Université catholique de Louvain
Ecole polytechnique de Louvain
Institute of Mechanics, Materials and Civil Engineering

Nanomechanical lab on-chip for testing thin film materials and application to Al and Al(Si)

Michaël Coulombier

Composition du jury:

Prof. Thomas Pardoen (promoteur)	Université catholique de Louvain, Belgique
Prof. Jean-Pierre Raskin (copromoteur)	Université catholique de Louvain, Belgique
Prof. Joris Proost	Université catholique de Louvain, Belgique
Prof. Stéphane Godet	Université Libre de Bruxelles, Belgique
Prof. Ingrid De Wolf	Katholieke Universiteit Leuven, Belgique
Prof. Taher Saif	University of Illinois at Urbana-Champaign, USA
Prof. Grégoire Winckelmans (Président)	Université catholique de Louvain, Belgique

Louvain-la-Neuve, March 6, 2012

Remerciements

Les "remerciements" constituent traditionnellement le chapitre zéro du manuscrit d'une thèse de doctorat. Pour certains, c'est le seul chapitre qui ne sera pas lu. Pour d'autres au contraire, c'est le seul qui attirera l'attention. C'est aussi le seul chapitre rédigé dans la langue maternelle de l'auteur. C'est le seul qui est écrit à la première personne. Ce chapitre est à la thèse de doctorat ce que le générique est à un film. C'est le petit frère de la bibliographie puisqu'on y retrouve l'ensemble des sources d'inspiration de l'auteur. Ce chapitre enfin, c'est une délivrance, car lorsqu'on aura fini de le rédiger, c'est tout le manuscrit qui sera terminé.

Mon premier merci revient à mes deux promoteurs, Thomas Pardoen et Jean-Pierre Raskin, deux maîtres de l'optimisme capables de transformer les "j'en ai marre, j'en peux plus" en "c'est reparti, je suis le meilleur du monde". Je les remercie de m'avoir permis de faire partie des pionniers des micromachines. Je les remercie pour ce qu'ils sont au quotidien : des passionnés passionnants qui m'ont permis d'évoluer continuellement dans mon métier de chercheur.

I would also like to thank all the members of my jury: Joris Proost, Taher Saif, Ingrid De Wolf, Stéphane Godet and Grégoire Winckelmans who took the time to read the manuscript and created fruitful discussions about the lab on-chip concept before, during and, I hope, after the private defence.

Je tiens également à remercier toutes les "blouses bleues" des chambres propres, tous ces techniciens, ingénieurs, chercheurs et étudiants avec qui j'ai eu l'occasion d'interagir lors du combat continuel de l'homme contre la machine. Je ne citerai pas de noms en particulier car les blouses

bleues sont une immense armée et les contributions de chaque soldat m'ont permis de mener à terme bien des batailles.

Je remercie bien sûr l'ensemble des mes collaborateurs imapiens. Ils ont été nombreux et m'ont offert un environnement de travail idéal. Merci à tous d'avoir multiplié les événements extra-scientifiques. Je pense notamment aux tournois sportifs en tout genre, aux pauses multivitamines, à la préparation des animations "team building", aux triples Karmeliet et aux "kroepoek parties".

Et puis il y aussi toutes ces personnes de mon entourage qui, à des degrés divers, m'ont manifesté leur soutien durant tous ces mois où revenait souvent l'expression "j'peux pas, j'travaille sur ma thèse". Thèse, micromachine, fluage... autant de termes auxquels ils ne comprenaient pas grand-chose mais dont ils savaient que c'était important pour moi. Merci à vous tous.

Et enfin j'adresse un énorme merci à celle qui a su sacrifier soirées et weekends à l'accomplissement de cette thèse. Anaïs, tu m'as soutenu du début à la fin en rivalisant d'ingéniosité pour me faire garder le sourire lors de la longue période de "fin de thèse". Merci ! C'est promis, maintenant c'est vraiment la fin !

Contents

Part I

Context

Chapter 1

Scientific and technological motivations

The expression "thin films" is used when referring to layers of materials with thickness ranging from a single atomic monolayer to several micrometres. However, the small thickness of thin films is not their only specific feature as the deposition methods are very particular. Indeed, thin film fabrication requires specific techniques usually divided into Chemical Vapour Deposition (CVD) and Physical Vapour Deposition (PVD). These processes are responsible for the specific microstructure of thin films which then influences their properties. The sometimes unique properties of thin films encouraged their use in a wide variety of applications:

- The microelectronic industry is probably the main field that has promoted the development of the thin film technology. Electronic devices make use of the electrical properties of thin films as well of their small size with the continuous quest for miniaturisation.
- In MicroElectroMechanical Systems (MEMS), the mechanical properties of thin films are important considering that some elements of the device move and deform in response to an electric signal (actuators). Similarly, an external force can induce the motion of

an element of the device which in turn is converted into an electric signal (sensors).

- Thin films can be used also as surface coatings for surface functionalisation of bulk metallic, ceramic, glass, and polymeric materials. In this case, the mechanical or optical properties of the film material are used to improve (e.g. wear resistance) or to add a particular property (e.g. reflectivity) to the substrate.

In all these applications, the reliability of the devices and coatings is a major concern. Material with small-scale dimensions involve indeed mechanical properties different from their bulk counterpart. This is due to the dominance of surface and interface effects in thin films as well as due to their particular microstructure (e.g. with often only one grain over the thickness). These particular features can affect the mechanisms controlling the deformation and fracture behaviour of the films which can have deleterious effects on the proper operations of the devices. It is thus essential to develop testing methods to characterise the mechanical properties of thin films. Moreover, combining the extraction of the mechanical properties to standard observation with SEM and TEM is needed to understand the origin of the size dependent deformation and failure mechanisms in thin films. Understanding the link between the microstructure and the mechanical properties can then open new routes to improve the properties.

Whereas conventional MEMS structures aim at extracting the internal stress and Young's modulus of the coatings, we are interested here in extracting the entire behaviour of the thin film materials from small elastic strain to large plastic strain. Adaptation of classical techniques used to test bulk materials is not straightforward and, over the years, numerous concepts of micro- and nanomechanical testing techniques have been proposed. In this thesis, a novel concept based on MEMS fabrication methods is developed which aims at solving some of the deficiencies of the existing techniques. The original idea of the concept is to use the internal stress generated in a thin layer to actuate another layer from which the mechanical properties can be extracted. This original idea was first proposed by J.-P. Raskin and T. Pardoen and I demonstrated

the feasibility of the technique during my master thesis in 2006[1]. This thesis is the first one on the subject and has, for primary objective, to demonstrate the ability of the technique to extract full stress-strain response of thin film materials. Although the concept does not allow to directly test the adhesion of thin films on substrate, one major strength is its versatility as the simple fabrication process enables to extract in principle the mechanical properties of any industrial deposit. This work describes the novel concept and is applied to the study of the mechanical behaviour of Al and AlSi films revealing some interesting physical and mechanical effects.

The thesis is divided into three main parts. Part I starts with the context of the work with Chapter 2 describing the state of the art in mechanical testing of thin films while Chapter 3 focusses on the mechanical properties and deformation mechanisms already observed in Al films. In Part II, the new tool developed in the frame of this thesis is described in details. The concept is presented in Chapter 4 together with the rules governing the design procedure. Chapter 5 describes the fabrication process while Chapter 6 explains how the parameters needed for data reduction are extracted. The last chapter of part II (Chapter 7) gives some additional extensions to the new tool. Part III finally gives all the extracted results from the new mechanical tool focussing on two thin film material systems: AlSi (Chapter 8) and pure Al (Chapter 9).

[1]The technique is now patented under the name "Thermal stress actuated micro- and nanomachines for testing mechanical properties of micro and nano-sized material samples".

Chapter 2

State of the art in mechanical testing of thin films

Adaptation of mechanical testing methods used for macro-sized specimens to the micro- or nanoscale is not straightforward. The physical dimensions of specimens of interest range from a few hundreds micrometres down to several nanometres. As a consequence, specimens are easily damaged through handling and gripping. Moreover, extreme displacement and load resolution is required for extraction of mechanical properties of small specimens.

This chapter aims at reviewing some of the methods developed for the extraction of the mechanical properties of materials with at least one small dimension. These methods are divided into two broad categories: testing of thin films on substrate (Section 2.1) and testing of freestanding thin films (Section 2.2).

This is not an exhaustive list and details about each of these techniques can be found in the cited references as well as in the following paper reviews: [22], [96] and [105].

2.1 Thin film on a substrate

2.1.1 Nanoindentation

Nanoindentation, also called depth sensing indentation, is the most widespread method used for mechanical characterisation. The idea is to measure the material resistance to a sharp tip as a function of the penetration depth. This results in a load-displacement curve with loading and unloading segments that describe the material response (Fig. 2.1a).

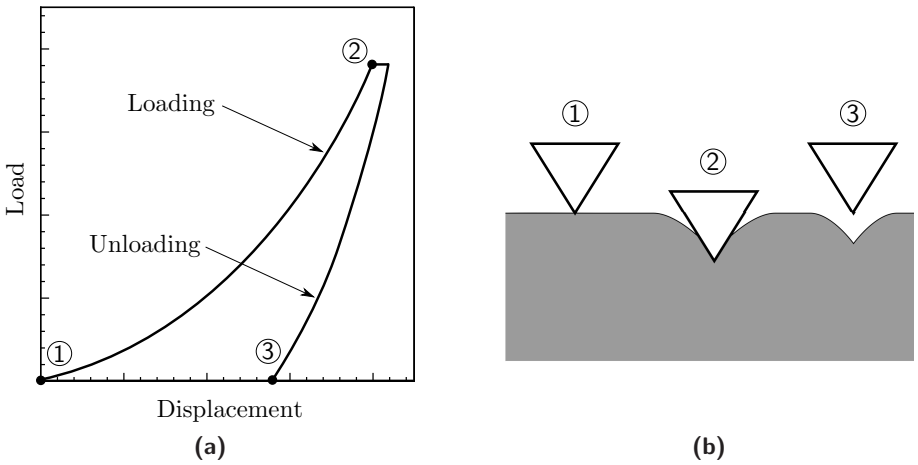

Figure 2.1: *(a) Schematic of a typical load-displacement curve obtained by nanoindentation, (b) side view schematic of the different steps in the nanoindentation process.*

The indenter tip is generally made of single crystal diamond and can be produced with different shapes depending on the type of experiment. The tip can be conical, spherical, cube corner, four-sided Vickers type or three-sided Berkovich type. The latter is the most frequently used in nanoscale testing as it is the easiest way to manufacture perfect sharp tips.

The different steps involved in depth sensing indentation can be described as follows. The tip is moved till making contact with the material (1 in Fig. 2.1). The load is then applied to maintain a constant tip

displacement rate. The material deforms first elastically and then plastically. The strain field in the vicinity of the tip is quite complex. After reaching the maximum indentation depth, the load is maintained for several seconds (2 in Fig. 2.1). The unloading takes place and the load is decreased to zero with the same rate as during the loading step (3 in Fig. 2.1). The unloading segment of the load-displacement curve is then governed only by the elastic properties of the material.

The main two parameters which can be extracted from nanoindentation are the hardness of the material H and its Young's modulus E.

The hardness is determined via the following equation:

$$H = \frac{P}{A}, \tag{2.1}$$

H hardness;

P applied load;

A indenter/material contact area[1].

The Young's modulus is extracted from the unloading part of the load-displacement curve. Doerner and Nix [25] proposed a first approach based on the assumption that unloading occurs linearly. Oliver and Pharr [99] improved that method assuming the unloading data were better fitted by a power law.

One inherent feature of the methods used to determine the hardness or the Young's modulus is that these quantities are not directly measured but rely on assumptions such as on the surface of the contact area. When it comes to thin film testing, it must be verified whether these assumptions are still valid. Indeed, in thin films, substrate effects play an important role in the shape of the load-displacement curve and the Young's modulus is more affected than the hardness. Practically, the maximum indentation depth should be limited to a small fraction of the specimen thickness in order to avoid substrate effects. This fraction

[1]This parameter depends on the indentation depth and is not measured. It is calibrated from indentations at different depths on a material with known mechanical properties.

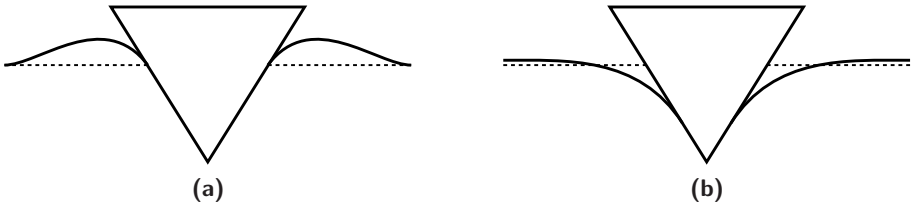

Figure 2.2: *Schematic of pile-up (a) and sink-in (b) effects.*

depends on the stiffness mismatch between the film and the substrate and can vary from less than 1% to more than 20%. Several models aim at increasing the accuracy of the extracted Young's modulus [61] but films typically thinner than one hundred nanometres should not be tested by nanoindentation. Too small indented volumes are not representative of the tested material and too large volumes will be affected by the presence of the substrate.

Another major complication with nanoindentation is the occurrence of pile-up (Fig. 2.2a) and sink-in (Fig. 2.2b) of the material around the indenter tip. Pile-up occurs in soft materials where plasticity is responsible for transport of material near the indenter tip. This increases the contact area between the film and the indenter. On the contrary, for hard materials, the difficulty to deform the material causes the strain field to propagate to a larger volume away from the indenter tip. This creates the sink-in effect and results in a decrease in the contact area between sample and indenter. Pile-up and sink-in effects both modify the contact area between the film and the substrate which has a direct impact on the accuracy of the extracted hardness and the Young's modulus.

The load-displacement curve obtained by performing a nanoindentation test on a thin film is a quite complex output. It is affected by many events such as cracking, delamination, pile-up and sink-in, substrate effect, etc. Nevertheless, nanoindentation stays a powerful tool as it needs no special requirement regarding specimen shape or preparation. Hardness and Young's modulus are the most routinely measured properties with this technique and have been extracted from numerous thin film

materials. The trend now is to couple nanoindentation with modelling to extract other material properties [12] [100].

2.1.2 Wafer curvature thermal cycling

The field of microelectronics and many other industries are very concerned by the deposition of thin layers on thick substrates. Deposition often occurs at temperatures higher than room temperature. Due to the difference in thermal expansion coefficients of the two materials, cooling to room temperature causes the substrate to curve to accommodate the strain. The change of curvature of the substrate can be linked to the internal stress arising in the film through the well-known Stoney equation (Eq. 2.2).

$$\sigma = \frac{1}{6}\frac{E_s}{1-\nu_s}\frac{t_s^2}{t_f}\left(\frac{1}{R_{post}} - \frac{1}{R_{pre}}\right), \tag{2.2}$$

σ	stress in the film;
$\frac{E_s}{1-\nu_s}$	biaxial modulus of the substrate material;
t_s	thickness of the substrate;
t_f	thickness of the film;
$\frac{1}{R_{pre}}$	initial curvature of the substrate;
$\frac{1}{R_{post}}$	final curvature of the substrate.

The Stoney equation is actually a simplification of the more general case of the thermo-elastic deformation of a bilayer which still has an analytical solution [39]. The simplification comes from the fact that the thickness of a layer (thin film) is negligible compared to the other layer (substrate). The interest of Eq. 2.2 comes from the fact that the stress is independent of the film properties. There is thus no need to know the Young's modulus of the thin film material to extract the internal stress. It is also important to note that Eq. 2.2 is valid for both elastic and plastic deformation within the film.

The thermal mismatch between the substrate and the thin film material is not the only origin explaining the internal stress, but it is the basic principle ruling the wafer curvature thermal cycling technique. The idea is to make use of differences in thermal expansion coefficients to impose varying biaxial strains in the film through heating and cooling.

Flinn et al. [41] were the first to use thermal cycling on thin films deposited on silicon wafers to extract mechanical properties. Many authors [128] [116] [4] [104] [80] used that method since then. The principle is always the same: record the internal stress in the film as a function of the temperature. The difference from one author to the other is the technique used to measure the stress. Two broad categories can be distinguished: those based on a direct measurement of elastic strains by X-rays and those based on measurement of the associated curvature. X-rays methods give information on all the components of stress but work only in the case of crystalline thin films. Substrate curvature methods give an average value of the stress but are easier to implement and work for any kind of films.

Fig. 2.3 shows a typical thermal cycling experiment in which the thermal expansion coefficient of the film is larger than the one of the substrate. Heating has thus the effect of reducing tensile internal stress which then turns into compressive stress. The deviation from linear elastic behaviour gives information about the yielding point. Then, the decrease in the compressive stress with increasing temperature gives information about the temperature dependence of flow stress. The cooling part of the experiment when tensile stress develops within the film gives also the tensile flow stress as a function of temperature.

Wafer curvature thermal cycling is thus a good technique to investigate yielding and plastic flow of thin films. This testing method has been used extensively to determine the yield stress variation of different Al alloy films [128] [116] [4] [80]. Still on Al alloy films, isothermal stress relaxation experiments by wafer curvature measurement were performed to determine the creep parameters of the film material [104] [92]. However, because the actuation is thermally imposed, no isothermal stress-strain experiment can be performed with the present technique. Moreover, any microstructural change that occurs during the experiment will contri-

bute to the shape of the stress-temperature plot. Indeed, grain growth, precipitation or recrystallisation can occur due to temperature. In this case, the first thermal cycling experiment can give a plot different from further heating and cooling cycles.

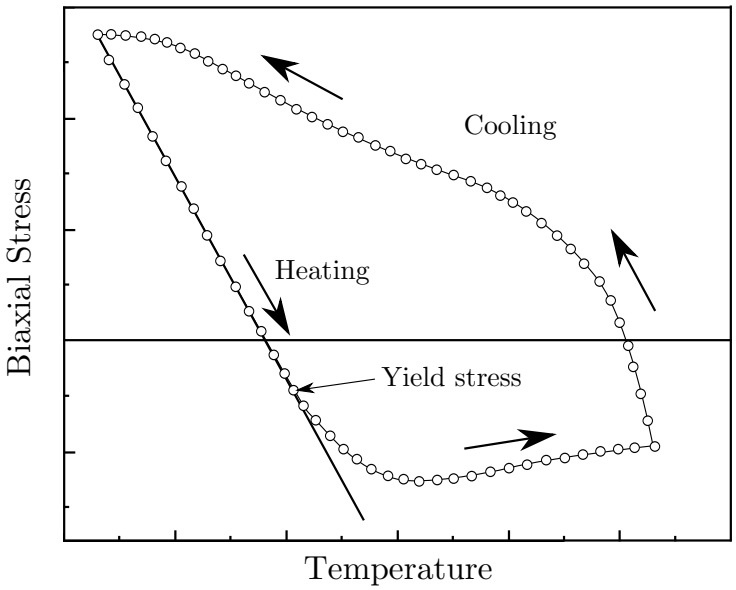

Figure 2.3: *Typical stress-temperature plot for a film on substrate submitted to heating followed by cooling back to room temperature.*

Changes in microstructure in such experiments as well as the will of having more insights in the deformation mechanisms has pushed some authors to modify the wafer curvature thermal cycling experiment in an in situ TEM experiment [86] [88]. This was performed by cutting from as-deposited samples followed by polishing.

2.1.3 Compression test of a film on a substrate

Due to the increasing number of nanoindenters and the existence of Focussed Ion Beam (FIB) as an etching tool, there has been a growing interest for performing compression of micropillars. This test is similar to macroscopic compression test except from the fact that the specimen

is not freestanding. The lower end of the micropillar is indeed connected to the substrate in order to avoid micromanipulation. As a result, the substrate acts as the lower compression platen during the test. The actuation is performed with a nanoindenter with a flat punch as sketched in Fig. 2.4. Micropillar compression has been extensively used on Ni, Au, Al, Cu, Nb, W and Mo single crystals (see [123] and [51] for recent reviews). Most studies focussed on the strong dependence of the yield strength with the diameter of the pillar. However, care must be taken when interpreting data from FIB milled specimens as gallium ions used in specimen preparation can indeed induce defects in the material modifying its intrinsic properties [78]. Note that recently, Bei et al. [6] produced pillars by the dissolution of a matrix grown by directional solidification which enables to avoid the complications of FIB-related defects and damage.

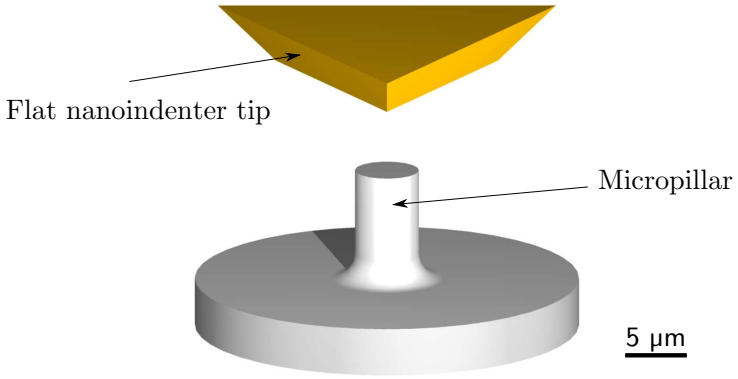

Figure 2.4: *Compression test on FIB prepared micropillar.*

2.1.4 Tensile test of a film on a substrate

Generally, the easiest way to extract mechanical properties of a material is to perform a uniaxial tensile test. Measurement of the force

versus displacement imposed to the specimen enables the extraction of the stress-strain behaviour. The challenge with thin films is the difficulty to handle and transfer thin specimens. An alternative consists in deforming films still attached to their substrates. This has the advantage of avoiding handling issues. However, determination of the stress applied to the film is quite difficult since the external applied force is distributed between the substrate and the film. In order to minimise the contribution of the substrate to the mechanical response of the film-substrate composite, soft materials with low Young's modulus can be used instead.

In [75], the thin film material is deposited as a long strip on top of a 4 µm-thick polyimide layer itself deposited on a silicon wafer. The polyimide is then peeled off the silicon and specimens are prepared by cutting strips in the polyimide which now acts as a substrate for the top thin film. The composite polyimide-thin film is then mounted on a micro-tensile testing machine for further actuation. Two kinds of samples are tested separately: thin film/polyimide strips and polyimide strips. The force-displacement behaviour of the thin film material is obtained by subtracting the force contribution in the polyimide tensile test from the composite tensile test (Fig. 2.5). This is correct as long as the two materials in the composite strip deform homogeneously (no occurrence of fracture or delamination). Note that a difference in the Poisson coefficients of the two materials can also induce lateral stresses in the tested thin film.

Another approach which avoids testing the polymer substrate independently from a substrate/thin film composite is to perform in situ stress measurement. X-ray diffraction is then used to measure directly the spacings between similar planes in the specimen material lattice. The offset with respect to the unstrained lattice parameter gives access to the stress via Hooke's law. This method was first proposed by Schadler and Noyan [113] and has been used by several authors since then [80] [64] [108] [52]. This technique implies to perform tensile testing in a stepwise manner. The sample is strained using a dedicated tensile set-up (electro-mechanical tensile machine [64], micrometre screw [108]) and a complete stress measurement is done with the X-ray synchrotron

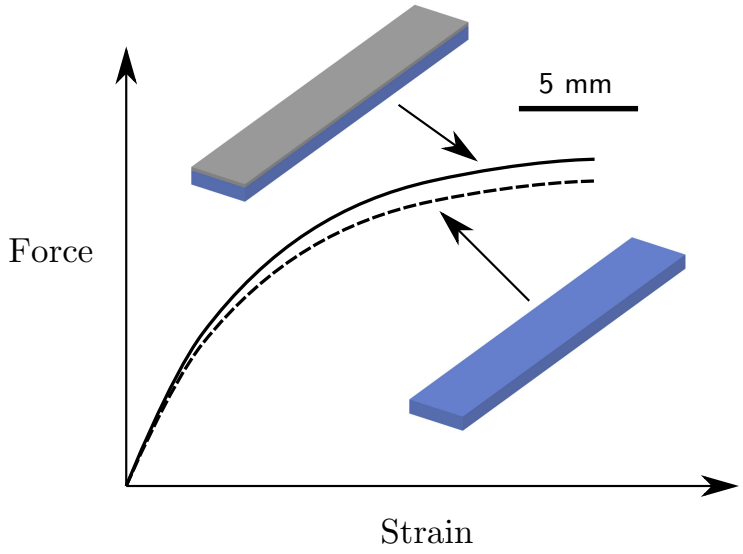

Figure 2.5: *Illustration of the methodology used for tensile testing on polyimide substrate with typical length scale of the specimens [75].*

after each step.

Oh et al. [97] performed an in situ TEM experiment with thin films on polyimide substrate. For this experiment, dogbone shape specimens were designed (metal on top of a 8 µm-thick polyimide layer). The specimens were glued on a rectangular Cu support itself fixed to a straining stage. The centre of the support had a rectangular hole for TEM observation. Further ion milling of the polyimide substrate was necessary to have electron transparent specimens. Although such experiments give a lot of information on the behaviour of the thin film material, stress and strain are not measured during the in situ experiment. Instead, separate tests are performed on the same kind of samples by in situ XRD straining techniques using a synchrotron radiation source as in [113].

Besides the TEM investigations of Oh et al. [97], tensile testing of films on compliant substrate has been performed to get the full tensile stress-strain behaviour of the film material. Kang et al. [75] focussed on Al films whereas Arzt and Spolenak [80] [52] focussed on Cu.

2.2 Freestanding thin films

MEMS devices differ from the structures of previous section by the presence of freestanding parts. Fabrication of MEMS includes the same deposition and patterning steps used in microelectronics to build complex sandwishes of 2D structures. The additional step is the etching of a sacrificial layer to free the upper layers from the substrate. This enables to dispose of movable structures. One inherent problem with freestanding structures is their tendency to deform once released from the substrate. This comes from the release of the internal stresses that arise in the successive layer depositions. As a consequence, very soon in the history of MEMS, work has been done to extract the internal stresses in thin layers (Section 2.2.1). It is only afterwards that structures were designed to extract the intrinsic mechanical properties of thin layers such as the Young's modulus (Section 2.2.2 and Section 2.2.3) and even later that the focus was put on extracting the full mechanical behaviour until fracture (Section 2.2.4).

2.2.1 Extraction of internal stress

Usually, the most common way to extract the internal stress of a thin layer on a substrate is to measure the change of substrate curvature consecutive to deposition. This relies on the Stoney formula which is explained in Section 6.5. The main advantage of Stoney formula is to provide a direct measurement of the internal stress of a thin film on a substrate but does not necessitate to know the Young's modulus of the film. Unfortunately, wafer curvature measurement does not allow local stress measurements and cannot account for stress gradient. Many freestanding structures have thus been proposed to measure, for a known Young's modulus, the local average residual stress. Some of them are reviewed in [124]. Such structures are generally made of one material with a specific geometry so that, when etching the underneath sacrificial layer, the internal stress in the structure material is released creating a deflection of the structure. This deflection can be measured in order to extract the internal strain in the structure layer.

In the case of compressive internal stress, an array of clamped-clamped beams with varying length can be used as a strain sensor [54]. Once released, a single clamped-clamped beam under compressive stress will buckle if its length is higher than a critical length (see Fig. 2.6a). This critical length is determined by the Euler criterion as determined in [54]. A proper design of the array of beams enables to capture any level of compressive stress and the accuracy is fixed by the length increment between two beams.

A similar concept of array of structures can be used to determine the level of tensile internal stress. This time the structures are rings fixed to the substrate at two points while a central beam spans perpendicularly to the anchor points [53]. Once released, the tensile internal stress puts the central beam in compression (see Fig. 2.6b). Similarly to the clamped-clamped beams, buckling occurs for a critical length.

Rotating sensors are another type of strain sensor where two beams relax in opposite directions inducing a torque to a third beam which is deflected. Different geometries are encountered in the literature (see [63] and [124] for a review) and generally there is an analytical relationship linking the deflection to the internal strain although finite element simulations can provide more accurate results. These type of sensors are convenient for both tensile and compressive stress measurement (see Fig. 2.6c, d and e). They have been successfully used on a wide variety of materials including polysilicon [63], Al [27] and Cu [126].

2.2.2 Bending experiments

Bending of cantilever micro-beams was first performed by Weihs et al. [134] and has been reproduced since then in references [56] [32] [62]. The original technique involves the deflection of a freestanding cantilever beam by means of a nanoindenter (see Fig. 2.7) although electric actuation is also possible [130]. Standard microfabrication techniques are used to create the cantilevers. Dimensions are on the order of a few micrometers to submicrometer thickness, tens of micrometers wide and hundreds of micrometers in length. Using simple elastic beam theory, the stiffness of the cantilever can be extracted (Eq. 2.3).

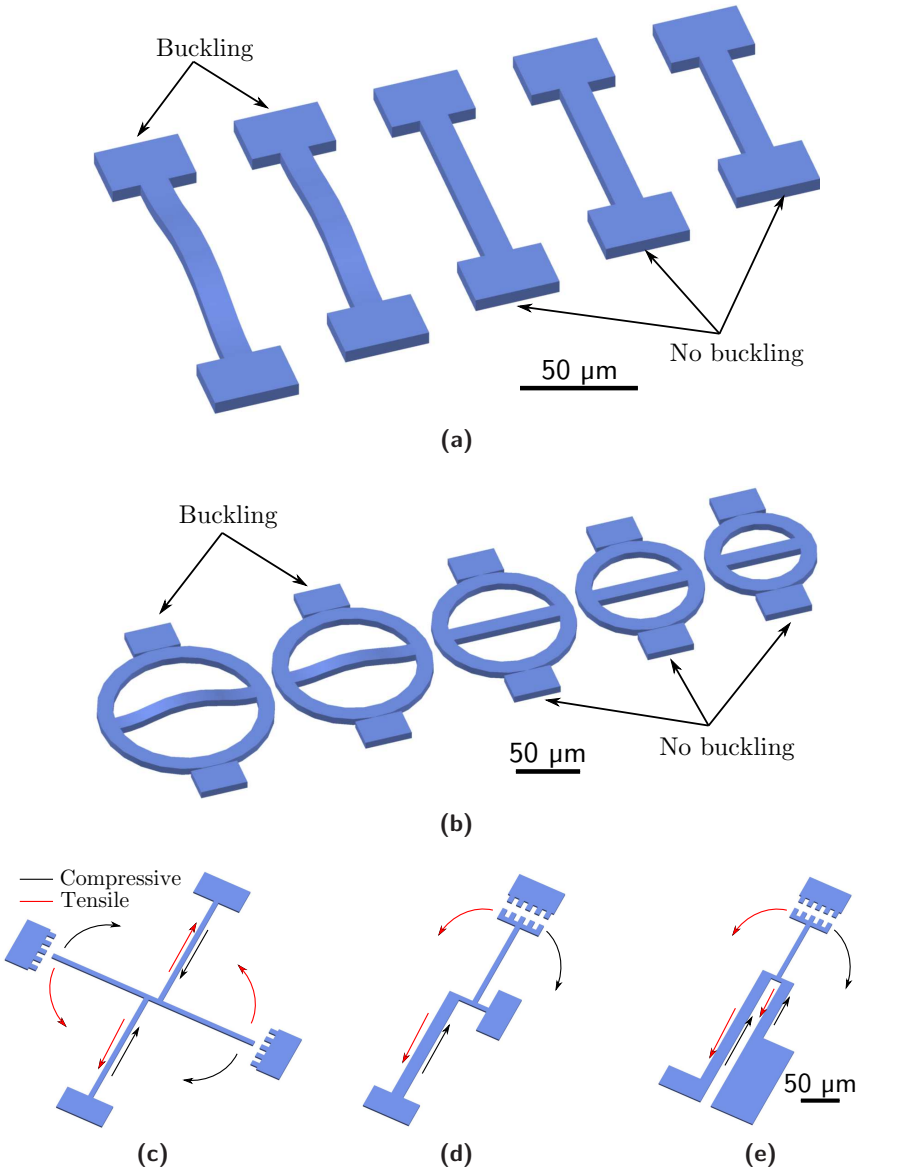

Figure 2.6: *MEMS structures aiming at extracting the internal stress in thin layers: (a) array of clamped-clamped beams for compressive internal stress, (b) array of rings for tensile internal stress, (c)-(e) various designs of rotating sensors for any type of internal stress (with typical length scale).*

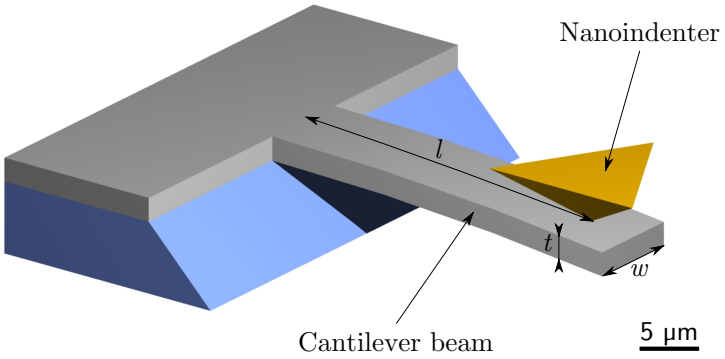

Figure 2.7: *Bending test performed on a freestanding cantilever beam (with typical length scale).*

$$k = \frac{Ew}{4(1-\nu^2)}\left(\frac{t}{l}\right)^3 \tag{2.3}$$

- k stiffness of the beam;
- E elastic modulus of the film material;
- w width of the beam;
- ν Poisson ratio of the film material;
- t thickness of the beam;
- l distance between anchor of the beam and contact point with the nanoindenter.

The stiffness is obtained from the bending experiment as the slope of the load-deflection curve. The Young's modulus can thus be extracted using Eq. 2.3. Special care must be taken when measuring the thickness and length of the beam as they appear to the third power. Moreover, undercutting of the anchor can introduce some uncertainties in the measurement of the cantilever length.

The yield strength can also be extracted as long as the permanent deformation regime is reached in the cantilever beam [96]. One of the major disadvantage of the technique lies in the inhomogeneous strain distribution in the cantilever beam. This is a consequence of the non-constant bending moment along the length of the beam. Florando and Nix [42] proposed a solution to that problem by performing the same kind of test on triangular beams. The resulting uniform strain field combined to simple computational modelling allows extraction of the stress-strain behaviour for the elastic regime as well as the early stages of the plastic regime. Van Barel [124] uses a different configuration where bending is performed on a chariot wheel structure instead of a freestanding beam which allows a more accurate determination of the Young's modulus.

Bending has been used on a wide variety of materials ranging from standard metals like Al and Cu [56] [42] to more exotic materials like ultra nanocrystalline diamond [32] and biocompatible materials [62].

2.2.3 Bulge test

The bulge test consists in deflecting a thin membrane by means of a pressurised fluid. In the original version of the bulge test developed by Beams [5], the freestanding film covers a cylindrical or rectangular shape cavity. The film is fixed at the edges of the chamber and the maximum deflection occurs at the centre of the membrane. The bulge height can be measured by interferometry. The output coming from a bulge test is a pressure-deflection plot with loading and unloading cycles. Based on an energy minimisation analysis complemented by finite element analysis [107], a relationship between pressure and deflection can be found where the residual stress and the Young's modulus of the membrane are the unknown parameters. The fitting of the experimental data with this relationship provides the values of both parameters. The stress and strain in the membrane are not directly measured and a data reduction procedure accounting for edge effects is needed.

The technique has evolved over the years essentially by changing the shape of the cavity. By using a high aspect ratio rectangular cavity, the edge effects are concentrated in the rectangle short ends and uniform

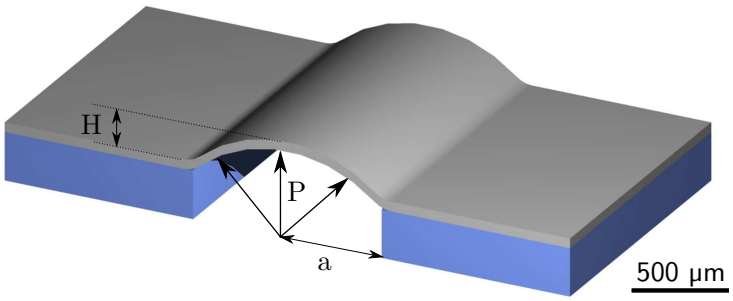

Figure 2.8: *Cross-section of the middle of a high aspect ratio rectangular membrane in a bulge test (with typical length scale).*

plane strain deformation develops within the middle of the membrane (Fig. 2.8). In this particular case no finite element analysis is needed for the extraction of stress and strain in the membrane. Instead, the following approximations can be made [105]:

$$\varepsilon = \frac{2}{3a^2} H^2 \tag{2.4}$$

$$\sigma = \sigma_{res} + \frac{E}{1-\nu^2}\varepsilon = \frac{a^2}{2t}\frac{P}{H} \tag{2.5}$$

ε	strain in the middle of the membrane;
σ	stress in the middle of the membrane;
P	pressure applied in the cavity;
H	bulge height;
t	membrane thickness;
a	half-width of the membrane;
σ_{res}	residual stress in the membrane;
E	Young's modulus of the membrane material;
ν	Poisson ratio of the membrane material.

The bulge test is a suitable technique for extraction of the elastic as well as plastic properties of materials. It has been used on a wide variety

of materials including metallic [52] and polymeric [67] layers to extract properties such as the residual stress, the Young's modulus and the yield strength. Extension of the bulge test to higher pressures can even be used to burst rectangular membranes [107]. In this case, finite element analysis gives access to the fracture strength.

The bulge test is usually reported as an easy method to determine the in-plane mechanical properties. However, apart from Vlassak et al. [135] who report deformation up to 4%, most experiments report deformation below 1% [133] [136] [52] [94] and other techniques should be preferred to measure the mechanical behaviour of more ductile films.

Another limitation comes from the residual stresses in the membrane. Tensile residual stresses make the membrane flat when no pressure is applied. On the contrary, compressive residual stresses result in a buckling of the membrane. In this particular case, the resulting initial dome height has to be accurately measured in order to avoid large errors in the experimental results.

2.2.4 Uniaxial tensile testing

As already stated in Section 2.1.4, the uniaxial tensile (or compressive) test provides the easiest interpretable data in order to extract the mechanical behaviour of a material. But, adaptation from bulk testing to small-sized specimen testing is not straightforward. Indeed, new concerns arise such as specimen preparation, handling and mounting. This section aims at describing some of the major attempts to circumvent these difficulties.

Four major components can be distinguished in any tensile testing machine. These are the mechanical frame and the grips, the actuator, the load sensor, and the strain sensor. All these four components need to be adapted for small-sized specimen testing.

In the method developed by Read et al. [106] [14], microfabrication techniques such as deposition, lithography and etching procedures are used to produce micro-sized specimens. The substrate is a silicon wafer and the frame and specimen are made with the same thin film deposit. The

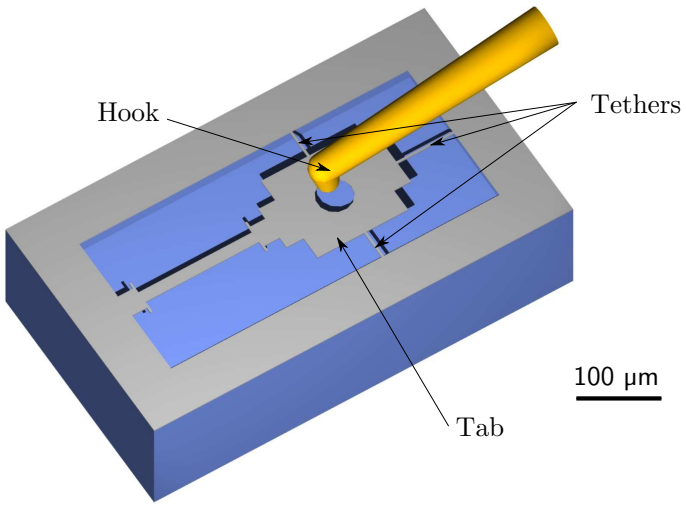

Figure 2.9: *Tensile test developed by Read et al. [106] (with typical length scale).*

specimen is a 180 µm-long and 10 µm-wide beam. One end of the specimen remains connected to the surrounding frame while the other end is a tab connected to the frame via three tethers (Fig. 2.9).

The silicon under the specimen beam, tab and tethers is removed over a sufficient depth so that a hook can be inserted in the tab. The hook is connected to an extension arm and a force sensing device which has a force range of 20 mN. The hook with extension arm and force sensing device is further mounted on a three-axis micromanipulator having piezoelectric motors that acts as the actuator. Before starting uniaxial loading, the tethers are cut with the hook. The hook is then inserted in the middle of the tab and tension is provided by moving the hook along the correct axis. The tensile test is performed under a microscope and displacements and strains are calculated using digital image correlation (DIC) techniques. This technique was successfully used to extract the stress-strain curve of micro-sized films in polysilicon, pure Al, Al alloys, polyimide and electrodeposited Cu [14].

Another noteworthy tensile testing technique is the one developed by

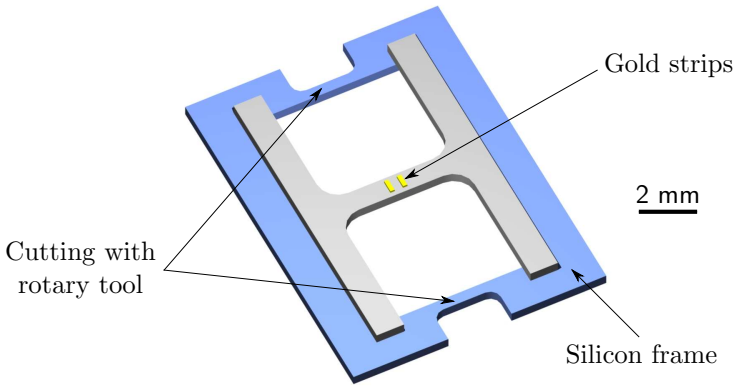

Figure 2.10: *Tensile test developed by Sharpe et al. [115] (with typical length scale).*

Sharpe et al. [115] [84] depicted in Fig. 2.10. This technique was originally designed to allow very accurate measurement of the Young's modulus. Microfabrication is used to pattern the specimen in a dogbone shape. The specimen is around 600 µm-wide, a few millimetres long and a few micrometres thick. The substrate is a silicon wafer and bulk micromachining allows to etch a window underneath the specimen. The silicon frame with the specimen is then mounted on the testing stage, gripped at both ends and glued. One of the grips is fixed while the other is attached to a load cell mounted on a piezoelectric actuator. Before tensile testing, the two narrow sides of the silicon frame are cut with a rotary tool to free the specimen from the frame. During testing, the load is measured via the load cell which has a resolution of 5 mN and a load range of 4.5 N. Strain is measured on the tensile specimen by laser-based interferometry as reflective gold strips are patterned on the surface of the specimen. These strips form interference fringes when illuminated with a laser. The fringes motion enables real time extraction of the strain with a resolution of 5 microstrain.

Gianola et al. [48] used the same technique as Sharpe et al. with a dif-

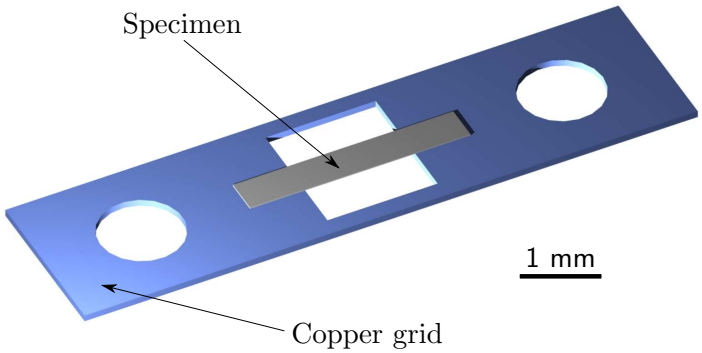

Figure 2.11: *Tensile test developed by Legros et al. [87] for in situ TEM investigation (with typical length scale).*

ferent method for strain measurement. The displacement was measured directly at the specimen grips with a capacitance gage or via an optical extensometre. Al films thinner than a few hundreds of nanometres were tested this way [47] and the probing of similar specimens confirmed the repeatability of the technique. DIC was used to track the evolution of deformation past tensile instabilities such as plastic localisation.

In Legros et al. [87], a set-up similar to Sharpe et al. is used for TEM investigation (Fig. 2.11). The specimens are shaped as rectangular strips 1 mm-wide and 3 mm-long. The silicon frame is glued onto a deformable copper grid. The copper grid is then stretched within a TEM. Deformation is thus transferred to the specimen and the deformation mechanisms can be observed in situ. The technique does not allow the measurement of stress and strain within the specimen as the focus is put on qualitative observations. This technique allowed to underline stress-assisted grain growth as a deformation mechanism in pure Al films.

Another tensile testing technique, developed by Tsuchiya et al. [122]

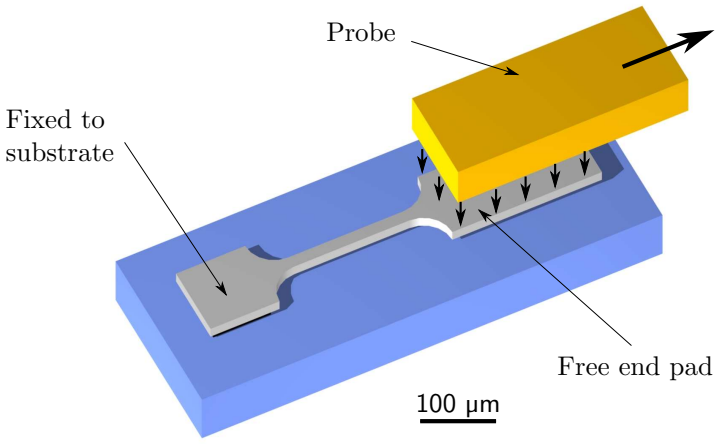

Figure 2.12: *Tensile test with electrostatic gripping developed by Tsuchiya et al. [122] (with typical length scale).*

[121] [120], uses an electrostatic force gripping system to load the film. The thin film specimen is a beam fixed at one end to the silicon substrate and with a large pad at the other end (Fig. 2.12). The specimen dimensions in the gauge region are on the order of 100 to 500 µm for the length, 20 to 50 µm for the width and 100 nm to several micrometers for the thickness. For tensile testing of the cantilever beam, a probe is brought into contact with the free end pad. An electrostatic attractive force is generated between the two surfaces by applying a voltage. Electrostatic forces being weak compared to mechanical forces, the dimensions of the specimen are chosen so that the force in the gauge region never exceeds the one in the gripping system. Tensile testing is achieved by piezoelectric actuation of the probe along the axis of the specimen. Force is measured using a load cell with a range of 1 N. Two gold gauge marks on the specimen allow direct strain measurement by means of optical microscopy. This technique allowed to capture the stress-strain curve from small deformation until fracture for monocrytalline Si, polysilicon as well as Ti and Ni films [120].

As electrostatic gripping is limited to conductive materials and imposes

constraints on the specimen design, Chasiotis and Knauss [11] developed a testing procedure a little different from Tsuchiya et al. Electrostatic forces are used to stick the specimen pad to the substrate while a probe with an adhesive layer is fixed to it. This enables to prevent any movement of the specimen during attachment allowing better alignment between probe and specimen. Curing of the adhesive layer with UV light is performed before the electrostatic force is reversed to release the specimen from the substrate. Tensile testing occurs then in a similar manner to Tsuchiya et al. except from the strain measurement which is performed through atomic force microscopy (AFM) and DIC.

The membrane deflection experiment (MDE) developed by Espinosa and co-workers [35] [36] [102] is an original technique to generate a uniaxial tensile loading (Fig. 2.13). The specimen is shaped in a double dogbone with both ends fixed and with a wider area in the centre where a line-load is applied. This geometry aims at minimising the stress concentration where the loading device contacts the freestanding specimen. Microfabrication techniques are used to pattern the specimen and to create an opening beneath the membrane. A nanoindenter is used to provide a line-load at the centre of the wider area to achieve specimen stretching. This results in direct tension in the gauge region of both dogbones. The load-displacement curve from the nanoindenter gives access to the force in the specimen while an interferometer focussed on the bottom side of the specimen allows to extract independently the deflection in the specimen gauge region. MDE has been used to test films thinner than 1 μm of both elastic-brittle and elastic–plastic materials [102].

Standard microfabrication techniques are not the only way to produce specimens. Similarly to the fabrication of micropillars for compression testing (see Section 2.1.3), Kiener et al. [77] patterned needle-like single crystal rods by FIB. Sample preparation is time consuming but it allows accurate control of the shape of the final specimen. After FIB cutting, the specimen is directly placed in a SEM chamber for tensile testing. Actuation is performed with a gripper adapted to the specimen shape (Fig. 2.14). The gripper is itself connected to a microindenter capable of forward and reverse loading. The load-displacement behaviour is subjected to noise at the beginning of the tensile test due to the initial poor

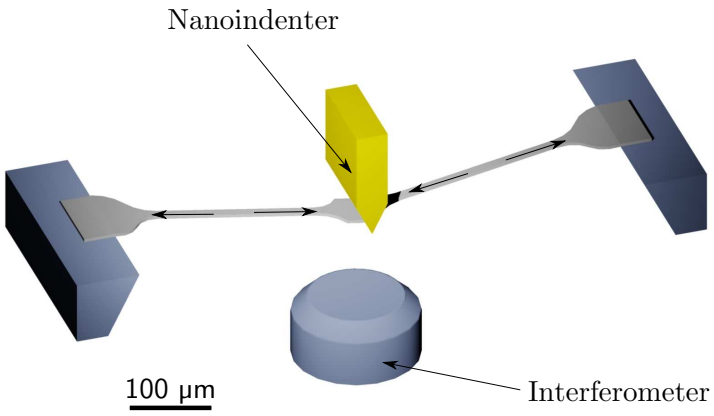

Figure 2.13: *Membrane deflection technique developed by Espinosa et al. [35] (with typical length scale).*

contact between the specimen and the gripper. A major advantage of this in situ technique lies in the highly precise alignment between actuator and specimen. This technique was used to test single-crystal Cu specimens.

One of the major difficulties in the techniques cited above is the connection between micromachined specimens and external loading devices. Microelectromechanical systems (MEMS) can be advantageously used to circumvent theses difficulties as actuators and strain sensors can be directly integrated on the wafer. A MEMS-based testing approach was developed by Saif et al. [59] [56] [57]. The set-up is a single crystal silicon frame (Fig. 2.15). One end of the structure is attached to a piezoelectric actuator and the other end is fixed. The specimen is deposited during the fabrication process with one end connected to a fixed-fixed beam with known spring constant that acts as a load sensor. The other end of the specimen beam is connected to the actuator via a supporting beam structure. The innovation lies in the fact that the supporting beam structure is designed to convert any non-uniaxial load into direct

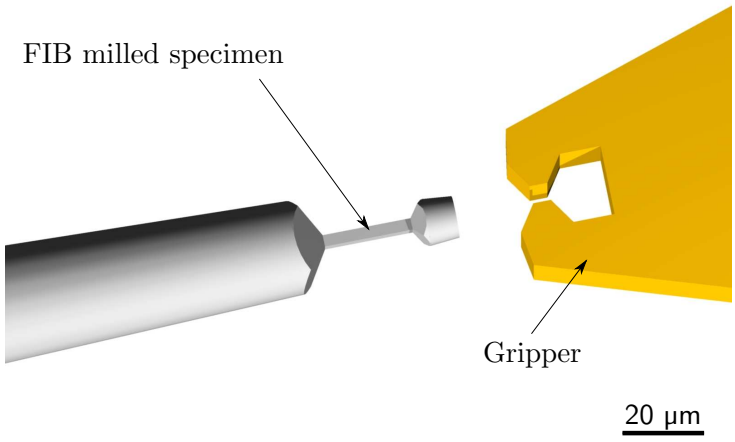

Figure 2.14: *FIB milled specimen tested by the technique developed by Dehm et al. [77] (with typical length scale).*

tensile load on the specimen. This solves the difficult issue of loading device-specimen alignment. The set-up can be integrated in a SEM or TEM and the displacement is read directly from cursors located next to the specimen. Al film with thickness down to 50 nm have been tested so far [111].

Another MEMS-based approach is the one developed by Espinosa et al. [105] [33]. The technique relies on two types of actuators: electrostatic (comb drive) and electrothermal actuators. The former is force controlled and is suitable for the testing of compliant specimens whereas the latter is displacement controlled which is suitable for stiff specimens. Electrothermal actuation is based on the thermal expansion of freestanding beams when subjected to Joule heating, as sketched in Fig. 2.16. Both types of actuators are made during the microfabrication process. The load is measured owing to differential capacitive sensors also built during the fabrication process. Microscopy is thus dedicated to the observation of local deformations on the specimen. The small size of the MEMS device allows in situ observation within a SEM chamber or TEM

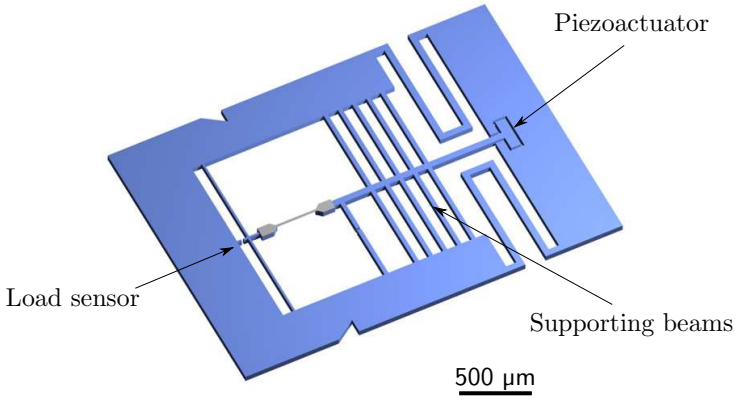

Figure 2.15: *MEMS-based tensile testing stage developed by Saif et al. [59] (with typical length scale).*

holder. Polysilicon specimens have been co-fabricated during the device microfabrication process although the technique allows mounting of nanostructured specimens such as nanowires and nanotubes by means of a nanomanipulator.

Finally, one recent technique developed at Sandia National Laboratories consists in a suite of test structures electrostatically actuated [21] [20]. Test structures are fabricated simultaneously on the test chip and have three different configurations: cantilever beams, fixed–fixed beams and notched fixed–fixed beams (Fig. 2.17). Each structure can be actuated electrostatically by applying a voltage between the structures and the underlying electrodes. Whereas the two first designs can give information about the Young's modulus and the internal stress of the tested material, the third one allows an increase of the stress in the notched region giving access to the inelastic properties of the layer material. Interferometry is used to measure the deflection as a function of the applied voltage. Modelling is performed to determine the strain field in the notched region corresponding to the measured deflection [21]. One of the advantage of the electrostatic actuation is that cyclic loading is possible

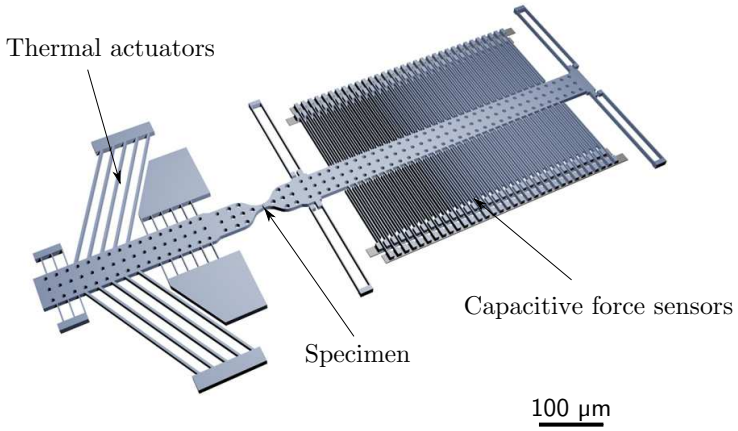

Figure 2.16: *MEMS-based tensile testing stage with electrothermal actuation developed by Espinosa et al. [33] (with typical length scale).*

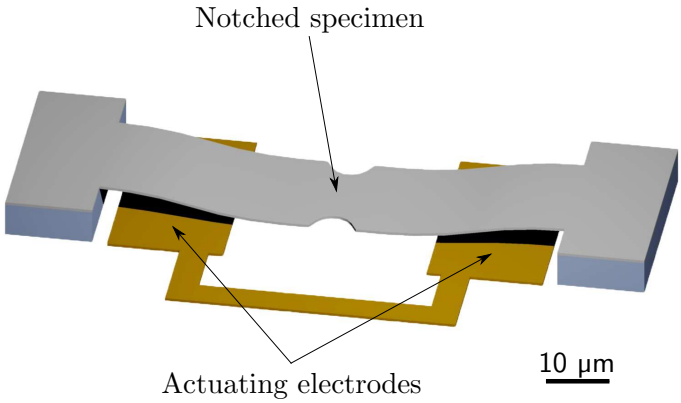

Figure 2.17: *Notched specimens with electrostatic actuation developed by de Boer et al. [21] as part of a suite of test structures (with typical length scale).*

which enables fatigue testing. Monotonic as well as fatigue loading have been performed with this technique on AlCu(0.5%) films [20].

2.3 Conclusion

This chapter presented the wide variety of techniques developed to measure the mechanical properties of thin films. The output of these devices ranges from single data like the internal stress and the Young's modulus to the full stress-strain behaviour. All the techniques differ by the actuation mean, the gripping system, the force and/or displacement sensors. There is no "Holy Graal" method and generally, there is a trade off between the complexity of the device and the number and accuracy of results. So there is room for other routes to investigate the mechanical properties of thin films. In this thesis, a new, simple and versatile on-chip tensile testing technique is proposed. It will be extensively described in Part II.

Chapter 3

Mechanical behaviour of Al thin films

A wide variety of materials is being used as thin films in microelectronics, MEMS technology as well as in thin coatings deposited on metallic, glass, ceramic and polymer substrates. They range from pure elements like Al and Cu to complex alloys. As this work is focussed on the extraction of the mechanical properties of Al and Al alloys, the first section of this chapter (Section 3.1) aims at reviewing the reported mechanical properties of Al thin films. The second section (Section 3.2) discusses the observed trends and gathers some of the experimental evidences about the deformation mechanisms in Al films.

3.1 Overview of mechanical properties of thin Al films

Looking through the literature, mechanical properties of Al films differ a lot from reference to reference. This can come from one or a combination of the following aspects:

- Deposition of a few micrometres down to a few nanometres of Al can be performed by different methods. Evaporation and sputte-

ring (physical vapour deposition) are among the most used technique for Al thin film deposition. Molecular beam epitaxy can be used as well and each method results in different microstructures. Moreover, the deposition conditions (deposition rate, substrate temperature, pressure, etc.) can be tuned to monitor the final microstructure.

- The purity of the Al target is of primary importance. If 99.99% pure Al target is often used, 99.999% is also met. The level of impurites can greatly influence the mechanical properties [71].

- Each author, depending on the testing technique, uses a particular substrate and, in some cases, the deposition of an adhesive layer can be necessary. The material on which Al is deposited can influence the growth of the film and thus its final microstructure and properties.

- Post-deposition conditions can alter the microstructure. Usually testing of Al thin films is not performed on the as-deposited film but on the film which underwent all subsequent process steps. Indeed, specimen microfabrication is sometimes part of a well established standard process which can involve further deposition steps on top of the Al films or annealing procedures. These steps can affect the surface of the Al film as well its microstructure which in turns modifies its mechanical properties.

- Other elements are often added to pure Al to avoid phenomena like spiking[1] or electromigration[2]. Si and Cu are respectively used for that purpose but other elements can be added in different proportions resulting in a wide variety of Al alloys with varying properties.

- Testing of the same film with different techniques can result in substantial differences. Differences in deformation mode (e.g. uniform vs gradient deformation [56]), strain rate, temperature can

[1] Non-uniform interdiffusion of Si into Al at the interface between Al and Si
[2] Transport of material caused by the movement of electrons or ions

indeed affect the extracted data. Moreover, different properties can arise just by comparing freestanding thin films and thin films on substrate or embedded between other layers.

Table 3.1 lists some of the mechanical properties of Al thin films given in the literature.

Materials and experimental conditions	Thickness [μm]	Grain size [nm]	E [GPa]	Yield strength [MPa]	Maximum strain [%]	Strain rate [s^{-1}]
Sputtered Al, bulge testing [107]	1.0	$\simeq$ 1000	73± 3	-	-	-
	1.4	$\simeq$ 1400	67± 2	-	-	-
Sputtered Al 99.9%, wafer curvature thermal cycling [29]	2.0	1000±200	-	∼200	-	-
	1.0	560±70	-	∼300	-	-
	0.6	540±70	-	∼450	-	-
	0.4	430±80	-	∼600	-	-
	0.2	320±90	-	>600	-	-
	0.1	140±10	-	>600	-	-
	0.05	200±10	-	>600	-	-
Evaporated Al 99.999%, micro tensile test on freestanding film [106]	1	∼300	∼30	94±10	22.5	3.0 10^{-4} to 6.0 10^{-4}
Sputtered AlCu(0.5%), suite of test structures (cantilever and notched specimens) [20]	0.43<h<0.65	∼1750	74.4±2.8	>172	∼4	-
Sputtered Al 99.99%, tensile testing on polyimide strips [75]	0.48	85	-	∼150	6	1.0 10^{-3}
	0.24	80	-	∼200	6	1.0 10^{-3}
	0.12	65	-	∼220	6	1.0 10^{-3}
	0.06	45	-	∼370	6	1.0 10^{-3}
Al, membrane deflection technique [36]	1	-	65-70	205	∼7	∼ 1 10^{-5}
	0.2	-	65-70	375	∼0.4	∼ 1 10^{-5}
Sputtered Al 99.99%, tensile testing with MEMS device [58] [60]	.485	212	-	∼450	∼3	-
	.2	80	-	∼525	∼2	-
	.15	65	-	∼600	∼2	-
	.1	50	69.6	∼750	∼1.5	-
	.05	22.5	62	∼550	∼2	-
	.03	11.1	60.2	325	∼0.6	-

Table 3.1: *Mechanical properties of Al thin films through the literature.*

The following paragraphs of this section aim at underlining the differences and similarities between bulk and thin film Al.

The Young's modulus of Al films is very similar to the one of bulk Al (69 GPa). It is not surprising as the Young's modulus is a property linked to the force of atomic bonds. No size effect is thus expected as the small dimensions encountered in thin films are still far larger than the atomic length scale. However, Haque and Saif [58] report for a lower Young's modulus for Al films with grain size smaller than 50 nm. This was attributed to the increase volume fraction of the grain boundary atoms with grain size reduction. The disorder in these grain boundary atoms are then responsible for the lower stiffness. But generally speaking, a lower Young's modulus of thin films with respect to bulk materials can be due to porosity. Thin film deposition techniques are indeed more prone to higher porosity than conventional bulk methods which is known to be detrimental to mechanical properties like stiffness but also yield strength [112] [137]. In addition, surface effects can play a role in the case of films thinner than 50 nm and can affect the measured Young's modulus.

The yield strength of pure polycrystalline Al is around 40-70 MPa. Table 3.1 reports higher values which seem to be dependent on the thickness and grain size. The dependence of the yield stress on the grain size is well established in bulk polycrystalline metals as stated by the Hall-Petch relationship (Eq. 3.1).

$$\sigma_y = \sigma_0 + kd^{-1/2}, \tag{3.1}$$

where σ_y is the yield stress, σ_0 is the lattice friction stress required to move individual dislocations, k is a constant and d is the grain size. This increase in yield strength with decreasing grain size comes from the fact that grain boundaries act as barriers against dislocation motion. However, the Hall-Petch equation is not sufficient to explain the increase of the yield strength and the limited numbers of grains along the thickness could contribute to the overall increase. Moreover, a reversed Hall-Petch effect has been observed for some experiments on nanocrystalline Al films [58]. The increased yield strength of Al films is encountered in

many other metallic materials and is at the origin of the famous "*smaller is stronger*" cited in a high number of publications dealing with thin films.

Bulk Al is known to be very ductile reaching uniform strain as high as 60%. Although all testing methods do not allow imposing such large strains, plastic localisation and fracture of Al thin films occur after a few percent of elongation only. This low ductility is a general trend in thin film materials and originates partly from imperfections which are inherent to thin film deposition methods and partly from a limited work hardening capacity [82].

Concerning the time dependent response, Al must receive special attention due to its low melting temperature (660 °C or 933 K). Indeed, creep phenomena are associated to thermally activated mechanisms like power-law creep (dislocation climb creep) and Nabarro-Herring-Coble creep (diffusional creep) [24]. Diffusional creep becomes important when the temperature is higher than 40% of the melting temperature which is not far from room temperature in the case of Al. In the work of de Boer et al. [20], room temperature experiments on loaded AlCu(0.5%) sputtered films did not detect creep after three hours at room temperature. Haque and Saif [59] [58] noticed the same lack of time dependent response on Al 99.99% films at room temperature. However, as their experiments were conducted in situ in a SEM, they noticed that, when exposed directly to the electron beam, creep deformation was occurring. This was attributed to the beam heating which provides the extra energy needed to activate creep.

3.2 Overview of deformation mechanisms in thin Al films

In this section, the microstructural features encountered in deformed thin Al films are reviewed in order to identify the underlying deformation mechanisms.

Wafer curvature thermal cycling in TEM was used by Dehm and coworkers [23] on Al epitaxial and polycrystalline films to understand the

higher yield strength occurring in thin films. Epitaxial films have no grain boundaries which allows to investigate the impact of the thickness on the yield strength alone. Film-substrate interface (Al-αAl_2O_3 here) was observed to act as a source for dislocations. Relaxation of the stress occurred by glide of these dislocations through the thin film. While gliding, dislocations segments are left at the interface. The measured yield strength[3] matches the prediction of Nix-Freund model [96]. In the case of Al polycrystalline films, the microstructure is totally different from epitaxial films as the films have now grain boundaries. Usually, polycrystalline Al films have a columnar grain structure with a grain size on the order of the film thickness and with grain boundaries perpendicular to the film surface (see Fig. 3.1). The tensile flow stress of polycrystalline Al thin films is found to be significantly larger than the epitaxial film for equivalent thickness. This is a consequence of the additional constraints imposed by grain boundaries. No emission of dislocation from film-substrate interface was detected this time but grain boundaries were found to absorb and emit dislocations. Yield strength still increases linearly with the inverse of the thickness for film thickness between 2 µm and 400 nm. A constant yield strength is reached for thinner films. Although the reason for this plateau is not well understood, plasticity at room temperature induced by thermal straining is observed to be dislocations mediated. On the contrary, diffusional processes dominate at the highest temperature. It must be noted that the grain size is not measured in this study. It probably scales with the thickness but the strengthening coming from grain boundaries cannot be isolated.

The increase in yield strength can result either from a decreasing grain size (Hall-Petch) or from a decreasing thickness (Nix-Freund model). In order to decorrelate these two contributions, Venkatraman et al. [128] [129] performed wafer curvature thermal cycling by successively removing an intentionally grown oxide on Al films. This enables to keep the grain size constant while modifying the thickness. The separation of the two strengthening components is done by considering that the flow stress σ_y is the sum of two components:

[3]The yield strength is taken at 40 °C after one thermal cycle.

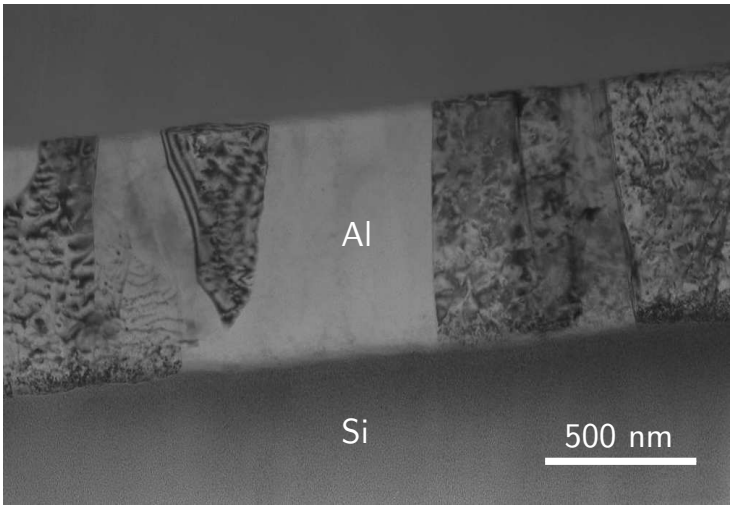

Figure 3.1: *Bright-field TEM image of an Al film on a Si substrate. Grains have a columnar shape with one grain over the thickness.*

$$\sigma_y = \sigma_{y,thick} + \sigma_{y,gb}, \tag{3.2}$$

where $\sigma_{y,thick}$ is the stress required to bow a dislocation pinned at the top and bottom surface of the film and $\sigma_{y,gb}$ is the grain boundary strengthening component. $\sigma_{y,thick}$ is expected to be proportional to $1/h$ (h being the current thickness of the film) while $\sigma_{y,gb}$ should remain constant for one deposited film as the grain size remains constant. The experiments confirmed the $1/h$ dependence of the thickness strengthening component[4] for thickness above 250 nm. Linearity of the plot of stress versus $1/h$ was not conserved for low values of film thickness as thermal straining was not sufficient to reach the high yield strength reached in these thinner films. Experiments on films with different initial thicknesses (different grain sizes) did not match the $1/d^{1/2}$ dependence of the yield strength predicted by the Hall-Petch relationship (Eq. 3.1). Instead, the data were more consistent with a $1/d$ dependence. In situ TEM experiments showed that deformation occurred by nucleation of

[4]The yield strength is taken at 60 °C after one thermal cycle.

dislocation loops on {111} planes [128].

Venkatraman et al. [128] also investigated the effect of a passivation layer on top of the Al film. A passivation layer can generally affect the properties of a metallic thin film by preventing dislocations from escaping out of the film. They noticed that thermal cycling experiment on Al film with a passivation layer did not reveal any change in the achieved stress levels. The native oxide is thus believed to act in the same way as the passivation layer.

In addition to pure Al testing, Venkatraman et al. [128] investigated the effect of the addition of 0.5% of Cu to the Al. Although the excess Cu formed $CuAl_2$ precipitates at grain boundaries, no significant hardening mechanism coming from precipitation was recorded. This was attributed to the fact that $CuAl_2$ precipitates occur in large plate-like form. And as the volume fraction of precipitates was low, a large fraction of grain boundary was free from precipitates. The effect is thus expected to be relatively limited. Using the same Al alloy, Proost et al. [104] performed isothermal stress relaxation between 50 °C and 175 °C. At these temperatures, relaxation occurred by dislocation glide. Proost et al. were able to determine the activation energy required for the dislocation to overcome the obstacles (ΔF) and the athermal flow stress (τ). The values found for these parameters were significantly higher than the ones reported for pure Al. This was attributed to an Orowan strengthening mechanism as TEM investigation revealed bowing of dislocations around $CuAl_2$ precipitates. The different behaviour of the Al-Cu alloy in Venkatraman et al. [128] and Proost et al. [104] comes from the stronger dispersion of precipitates in the latter case.

Another widespread Al alloy (AlCu(0.5%)Si(1%)) was tested by Kaouache et al. [76]. TEM investigation did not reveal any $CuAl_2$ precipitate but the silicon was found to form intragranular precipitates in the as-deposited form. These Si precipitates serve as anchoring points to dislocations in thermal cycling experiments. However, this anchoring effect is limited because ripening of Si precipitates occurs which lowers their number and increases their size. As a result, dislocation motion is hindered by only a few obstacles and dislocation densities are comparable to pure Al films. Again, the density of obstacles to dislocation motion

plays a major role on the strengthening as Flinn et al. [41] and Bader et al. [4] demonstrated that the addition of Cu to an AlSi alloy could increase the plastic flow stress. Data can indeed differ a lot in the literature only by considering the difference in thermal treatment before testing.

Other types of experiments than thermal cycling have to be taken into account to identify the deformation mechanisms in Al films. A first reason lies in the fact that other techniques enable constant temperature testing. Another reason is that thermal straining does not allow to reach high deformations. In order to be able to capture post yielding behaviour of Al at room temperature, Kang et al. [75] performed tensile tests on Al deposited on polyimide strips. The film thickness ranged between 60 nm and 480 nm. The stress begins to increase linearly and then parabolically with strain except in the case of the 60 nm-thick film (Fig. 3.2a). The strain hardening rate is very small. Although dislocation activity was rarely observed during deformation, the TEM observations on the deformed samples revealed networks of dislocations in some large grains as can be seen in Fig. 3.2b. In materials with high stacking fault energy like Al, climb and cross-slip is relatively easy. These mechanisms are responsible for the creation of the network of dislocations which form low-angle grain boundaries separating dislocation-free sub-grains. This has the effect to facilitate the nucleation of additional dislocations that are needed to further strain the material. This phenomenon is called dynamic recovery and lowers the strain hardening rate.

Similarly to Venkatraman et al. [129], Kang tried to separate the different contributions to the strengthening. The analysis was performed on the tensile strength instead of the yield strength. The strengthening from the thickness showed $1/h$ linear dependence as previously reported whereas the grain boundary strengthening was found to follow Hall-Petch type dependency ($1/d^{1/2}$). These observations are in agreement with TEM observations which show evidence of dislocations based mechanisms. However a decrease of the Hall-Petch slope in smaller grains could originate from non-dislocation type mechanisms such as diffusional creep, grain boundary sliding or grain growth.

The presence of a substrate or a passivation layer can induce significant

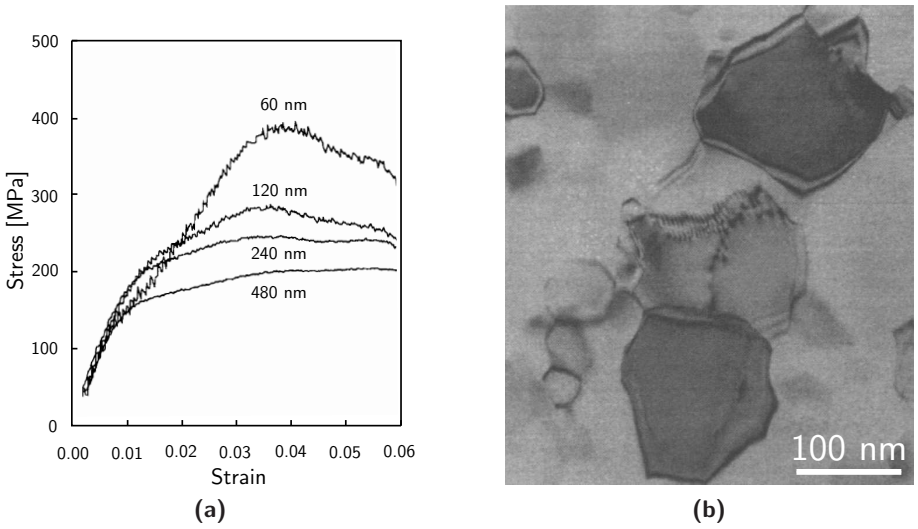

Figure 3.2: *Results extracted from tensile testing on Al thin films [75]: (a) stress-strain curves from different thicknesses and (b) bright field TEM micrograph of a* 120 nm*-thick Al film after 2% strain showing networks of dislocations forming low angle grain boundaries within the centre grain.*

constraints on the deformation behaviour of the tested films. Testing of freestanding films is thus performed to get rid of this constraints. de Boer et al. [20] tested AlCu(0.5%) films with their electrostatically actuated technique described in Section 2.2. The yield strength reached in these freestanding thin films was similar to the yield strength obtained from the simple model of Venkatraman et al. [129]. TEM analysis confirmed that plasticity was dominated by dislocation interaction within the grains. Dislocation density was found to be higher in the regions of the specimen experiencing higher deformation (notched region).

In all the experiments reported above, plasticity of Al films seems to be dislocation mediated. Obstacles to dislocation motion are grain boundaries, other dislocations and surfaces of the film (native oxide, passivation layer or substrate). The mechanisms are thus similar to the mechanisms encountered in bulk Al and the differences in mechanical properties come from the reduced grain sizes and the constraints imposed by the small thickness of films. However, when the grain size reaches the nanometre scale, the dislocation mechanisms governing work hardening in conventional materials are no longer geometrically possible. Other types of mechanisms should arise and could explain the deviation from classical Hall-Petch relationship in nano-grained films. Several molecular dynamics simulations [125] [38] suggest that although dislocation-mediated plasticity is always present in nanocrystalline materials, stress-assisted grain boundary deformation is more likely to occur.

To explore the behaviour of grain boundaries in nanocrystalline Al films, Jin et al. [73] [72] [93] performed in situ nanoindentation in a TEM at room temperature. The testing conditions were such that grain size was similar to or smaller than the contact area of the indenter (grain size between 100 nm and 500 nm). By indenting on the grain boundary between two grains, deformation occurred by elastic deformation followed by dislocation nucleation and dislocation multiplication. After this first stage of dislocation mediated plasticity, the grain boundary between the the two grains moved. The larger grains expanded as the smaller one shrank resulting in one final larger grain (Fig. 3.3). The same experiments on nano-grained films (20 nm) revealed similar phenomenon with grain growth starting almost immediately after the onset of the inden-

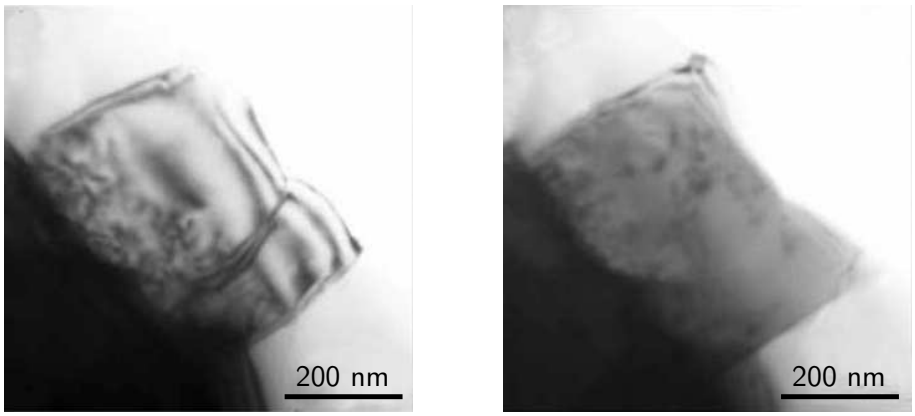

Figure 3.3: *TEM bright-field image (a) before indentation and (b) after indentation [73]. The larger grain grew by eliminating the smaller grain.*

tation process.

Although the in situ indentation experiment showed evidence of grain growth deformation mechanism, it cannot confirm whether this phenomenon happens in thin films. For this particular experiment, the sample is indeed thin in the thickness and in the direction of the electron beam. This has the important consequence that indentation stresses can be relieved by deformation perpendicular to the indenter, a mechanism that is not available in conventional films.

In situ TEM tensile testing of freestanding Al films was thus performed and pointed out for a similar mechanism. The experiments were performed by Gianola et al. [48] using a set-up similar to the one described in Fig. 2.10 and by Legros et al. [87] using the set-up of Fig. 2.11. In both experiments, discontinuous grain growth was observed at the tip of growing cracks (pre-existing crack in Legros et al.) and not in the other regions of the specimen. This indicates also the importance of the applied stress configuration in triggering grain growth. During loading, some grains with favorably oriented boundaries (grain size between 40

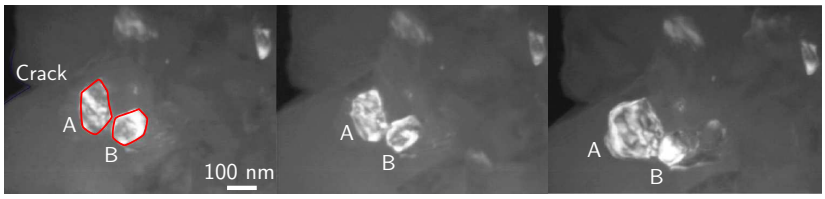

Figure 3.4: *TEM bright-field image showing grain growth by reorientation and coalescence [87].*

and 90 nm) grow first until reaching a critical size (200 to 400 nm) while the others maintain their initial dimensions. Upon further loading, an increased number of grains grow but the size of the larger grains remains constant. Growth was also found to occur by re-orientation and coalescence of grains with similar orientation (Fig. 3.4). Prior to deformation the microstructure was dislocation-free but as grain growth proceeded, dislocation activity increased in the larger grains (larger than 100 nm) leading to the formation of cells and subgrains. In Legros et al. [87], grain growth was observed to occur at very different strain rates (from 0.1 nm s^{-1} to 200 nm s^{-1}) suggesting different mechanisms. Additional experiments on freestanding Al films with geometric concentrators indicated that grain growth scaled with the shear stresses [109].

Grain growth has a direct effect on the macroscopic mechanical properties as ductility is enhanced and the strength is reduced compared to samples for which no grain growth is observed. Strain as high as 23% was reached for a 380 nm-thick pure Al films with initial grain size of 90 nm. This is one order of magnitude higher than the data reported on standard nanocrystalline materials. In the work of Haque and Saif [59] [56], tensile testing of freestanding Al films in TEM with dedicated MEMS-based set-up (Fig. 2.15) did not show any occurrence of grain growth. The films tested had grain sizes similar to the work of Gianola et al. and Legros et al. but showed limited ductility. Ductile fracture occurred by void growth and coalescence at a strain smaller than 2% [55]. The absence of grain growth in Al films tested by Haque and

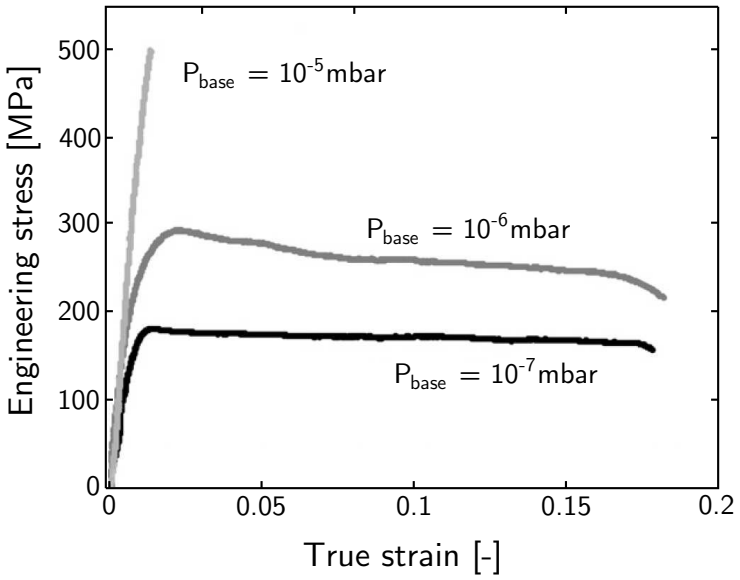

Figure 3.5: *Room temperature tensile stress–strain curves for three Al films deposited at varying chamber pressure showing two distinct classes of mechanical behaviour [47].*

Saif could originate from the purity of tested films. Gianola et al. [47] investigated the effect of purity by testing pure Al films deposited at varying chamber pressure, lower pressure resulting in less impurities and thus less pinning points for grain boundaries. They observed that only films deposited with base pressure under 10^{-6} mbar showed occurrence of grain growth and extended plasticity (Fig. 3.5).

The observations made in this section suggest that classical dislocation plasticity occurs in Al films when the grain size is larger than 100 nm. The strengthening with respect to bulk Al comes from the small grain size and the small thickness. The presence of a substrate, of the native oxide or of any passivation layer adds a constraint on the dislocation motion which strengthen the film. When the grain size falls below 100 nm stress assisted discontinuous grain growth occurs and dislocation mechanism proceed as soon as a critical size is reached and if pure enough. This grain growth mechanism enhances the ductility of Al films. The

addition of small amount of alloying elements to Al was found to create precipitates which can strengthen the Al by acting as obstacles to dislocation motion. However, the size and number of these precipitates is highly dependent on the thermo-mechanical history of the thin Al film. The deformation mechanisms in Al films are thus strongly dependent on the microstructure and can result in very different behaviours. This should be taken into account when comparing data from different authors.

Part II

Internal stress actuated micro-tensile testing stage

Chapter 4

Self actuated micro-tensile stage

In this chapter, the novel concept used in this work for extraction of the mechanical properties of thin films is presented. The chapter is divided in three sections[1]. The first one (4.1) describes briefly the basic ideas of the new technique. The second section (4.2) details the mechanics ruling the test structures. Finally, the third section (4.3) aims at providing the design requirements of the new concept in order to ensure accurate extraction of mechanical properties.

4.1 Concept

The new concept of micro- or nanomechanical test used throughout this work aims at measuring the mechanical properties of submicrometer films. The goal is to create a tensile testing technique which can easily be adapted to testing of any kind of thin film material. The technique must be able to extract the stress-strain behaviour from small elastic strain to large plastic strain. This concept differs from most of the techniques presented in (Section 2.2) through essentially two aspects:

[1]This chapter borrows a lot from the reference Gravier et al. [50] though extending several aspects.

1. The first idea is to use the internal stress present in one material, referred later as the "actuator", to impose the load to another film while avoiding any external loading and electrical signal.

2. The second idea is to take benefit of one of the greatest advantages of microfabrication technology which is the capacity for easily reproducing large numbers of elementary patterns, and thus multiplying elementary testing stages rather than building a complex multipurpose stage. Owing to this concept, thousands of elementary testing stages can be processed on a single silicon wafer with the potential to replicate suites of tests structures at multiple locations on the wafer, in the same vein as the approach by de Boer et al. [21] [20].

A single structure is called a "micromachine" and involves three thin layers deposited on top of a thick substrate as depicted in Fig. 4.1. The first layer is called "sacrificial layer" and is deposited over the entire surface area of the substrate with no patterning (Fig. 4.1b). The second layer is called "actuator layer" and provides the actuation force coming from the high tensile internal stress generated inside the layer during deposition. This layer is patterned following the design rules of Section 4.3 (Fig. 4.1c). Finally, the third layer called "specimen layer" is the film material to be tested. This layer is also patterned following the design rules of Section 4.3 (Fig. 4.1d). The sacrificial layer located underneath the actuator and specimen beams is etched away in a specific removal solution (Fig. 4.1e). This enables the release of internal stresses inside the actuator layer. The specimen beam being attached to the actuator beam, it is strained owing to the contraction of the actuator beam. The resulting freestanding structure reaches a stable position governed by force equilibrium. Knowing the displacement of the system actuator-specimen, direct application of force equilibrium (Section 4.2) gives access to the strain and stress in the specimen beam assuming that the actuator deforms elastically.

Different states of stress can be generated from small strain elastic behaviour up to fracture of the specimen beam by modifying the geometry

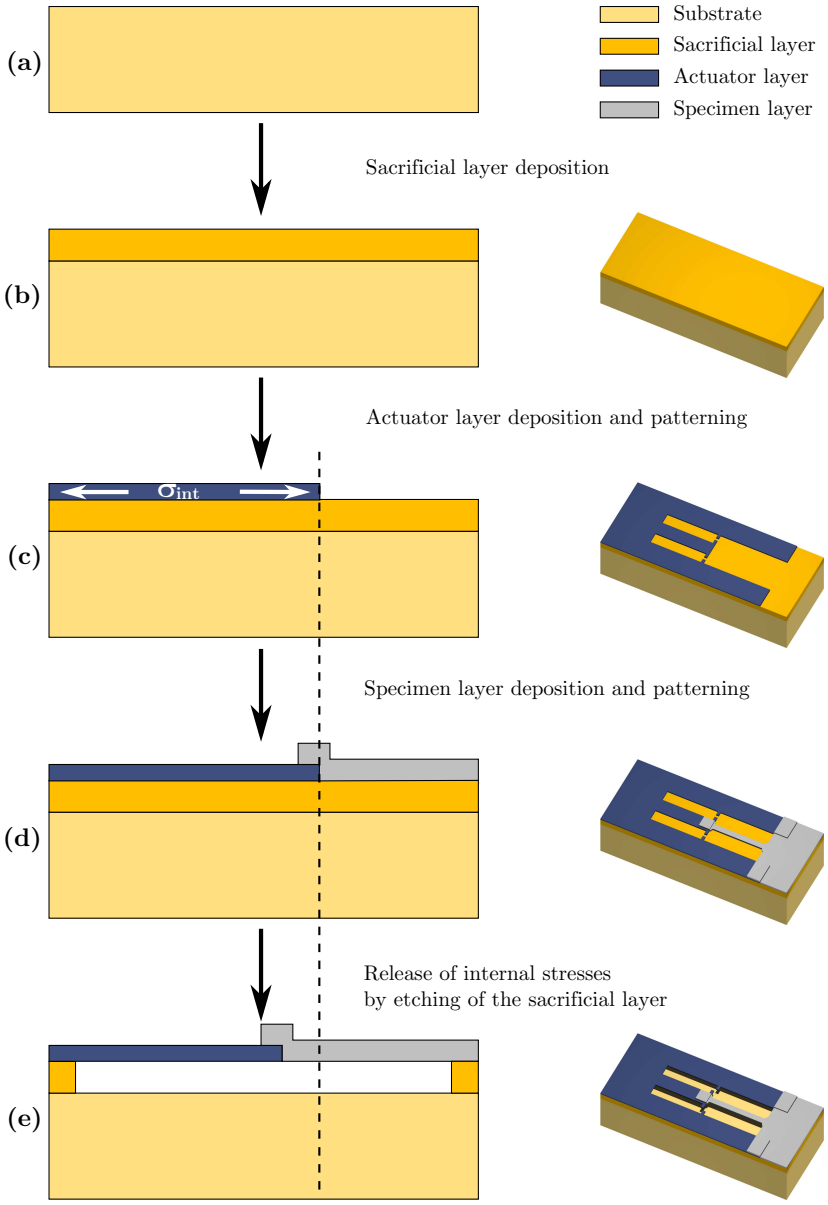

Figure 4.1: *Concept of a self actuated tensile testing stage. Starting from a bare substrate, the fabrication involves the deposition of 3 layers: the sacrificial layer (Fig. 4.1b), the actuator layer (Fig. 4.1c) and the specimen layer (Fig. 4.1d). The etching of the sacrificial layer under the test structure releases the stress in the actuator beam which then contracts and pulls on the specimen beam (Fig. 4.1e).*

of the beams. Microfabrication techniques are thus used to process a large number of those micromachines at the same time.

Up to now, four different generations of test structures have been designed. Even though each new generation took advantage of the learnings from the former one regarding the design rules and accuracy of the measurement, the focus was different for each generation.

- Generation 1 was used as a proof of concept and was motivated by the writing of a patent.
- Generation 2 aimed at testing different loading configurations such as shear, biaxial and compression, though in a qualitative way.
- Generation 3 focussed on uniaxial tensile loading. Design requirements were analysed in detail to ensure sufficiently accurate stress and strain determination [50].
- Generation 4 reproduced design of generation 3 with specific structures for brittle materials analysis as well as structures aiming at measuring the influence of stress on electrical properties.

In this work, almost all the results on pure Al and on Al alloys were obtained using generations 3 and 4.

4.2 Mechanical analysis of an ideal test structure

This section aims at analysing the mechanics of a single micromachine in order to determine the relationship that allows extraction of the strain and stress inside the specimen beam. Section 4.2.1 focusses on the behaviour of the actuator beam whereas Section 4.2.2 leads to the determination of the equations ruling the behaviour of the specimen beam.

4.2.1 The case of the actuator beam

Let us first consider the case of a single actuator beam before release (Fig. 4.2a). The actuator is undergoing large tensile internal stress which

can be represented by a force F_0 pulling on the actuator beam. After etching of the sacrificial layer, the freestanding beam can contract. If the actuator is free (not connected to anything), it contracts by an amount u_{free} (Fig. 4.2b). If the same actuator is not free but is connected to a specimen beam that prevents the actuator from fully relaxing, the actuator is subjected to a force F and it contracts by an amount u smaller than u_{free} (Fig. 4.2c). The displacements u and u_{free} are defined as positive when the actuator contracts during release[2].

As shown hereafter (Eq. 4.5), the displacements u and u_{free} can be directly related to the force F, the actuator geometry, and the material properties of the system. Hence, the actuator beam plays also the role of a load sensor. As stated later in Section 5.3, the selected material used throughout this work for the actuator beams is LPCVD silicon nitride. It is a stiff, brittle material which deforms in a linear elastic way and which can be deposited with large tensile internal stresses (around 1 GPa). The characteristic dimensions and properties of the actuator beam are the following:

ε_a^{mis}	mismatch strain in the actuator resulting from the deposition and subsequent fabrication steps;
σ_a, ε_a and ε_a^{mech}	true stress, total, and mechanical strains in the actuator beam after release, respectively;
E_a and ν_a	Young's modulus and Poisson ratio of the actuator material, respectively;
L_{a0} and L_{a0}^{free}	actuator lengths at the test temperature before chemical release of a constrained and a free actuator beam, respectively;
u and u_{free}	displacement between current (after release) and initial (before release) position in a constrained and a free actuator beam, respectively;
S_a and S_{a0}	current (after release) and initial (before release) cross-sectional areas of the actuator beam, respectively.

[2]In some micromachines, probably poorly designed, strong specimens with large internal stress could lead after release to a slight elongation of the actuator ($u < 0$).

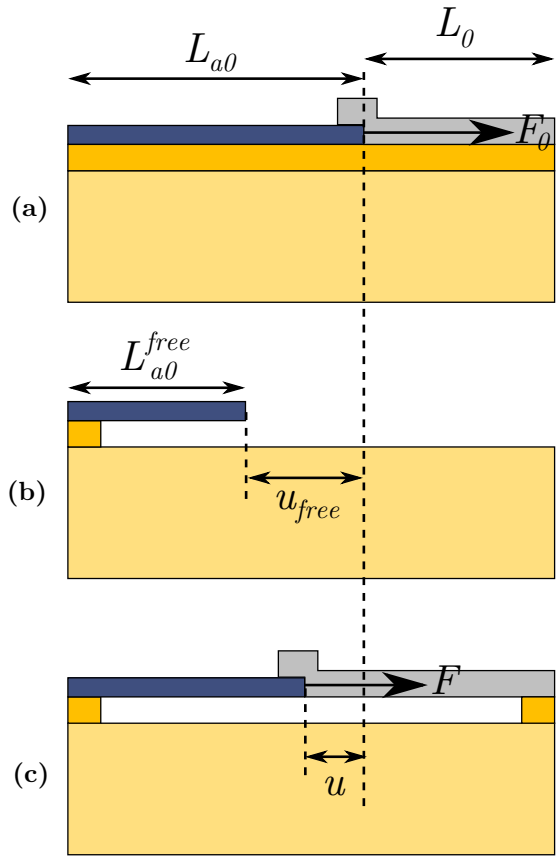

Figure 4.2: *Configurations that an actuator beam deposited on top of a sacrificial layer can take: (a) actuator beam is not yet released, (b) actuator beam is free to contract after the release, (c) actuator beam is constrained by a force F smaller than F_0, the initial force (e.g., by being attached to the specimen beam).*

The total strain inside the actuator is the sum of the mechanical strain and the mismatch strain, i.e.,

$$\varepsilon_a = \varepsilon_a^{mech} + \varepsilon_a^{mis}. \tag{4.1}$$

The total strain inside the actuator beam is given by

$$\varepsilon_a = \ln\left(\frac{L_{a0} - u}{L_{a0}}\right). \tag{4.2}$$

Throughout this work the maximum strain that can be reached in an actuator beam is around 0.3%. The small strain assumption can be made[3] and Eq. 4.2 becomes

$$\varepsilon_a = -\frac{u}{L_{a0}}. \tag{4.3}$$

The linear elastic behaviour of the actuator leads to

$$\sigma_a = E_a \varepsilon_a^{mech}. \tag{4.4}$$

In the case of a free actuator, the stress is equal to zero and $\varepsilon_a^{mech} = 0$, consequently, $\varepsilon_a^{mis} = \ln\left(\frac{L_{a0}^{free} - u_{free}}{L_{a0}^{free}}\right) \cong -\frac{u_{free}}{L_{a0}^{free}}$. The release of a free actuator provides thus the value of the mismatch strain. Other methods reviewed later in Section 6.3 can also be used to estimate ε_a^{mis}.

For the constrained actuator of Fig. 4.2c, the load F is obtained from Eq. 4.4 as

$$\begin{aligned} F &= S_a E_a \varepsilon_a^{mech} \\ &= S_a E_a \left(\frac{-u}{L_{a0}} - \frac{-u_{free}}{L_{a0}}\right) \\ &= \frac{S_a E_a}{L_{a0}} \left(u_{free} - u\right), \end{aligned} \tag{4.5}$$

[3]This assumption comes from the fact that $\ln(1 + x) \cong x$ for small x.

where the last equality shows that the force can be estimated only through the measurement of u and u_{free}.

The positions that the actuator can reach in a force-displacement diagram is a straight line (Fig. 4.3). The intersection with the horizontal axis corresponds to the free actuator (maximum displacement). The intersection with the vertical axis gives the force in the actuator before release of the sacrificial layer (maximum force). A longer actuator, having the same width, gives the same intersection with the vertical axis (internal stress, i.e. force divided by actuator cross-section, is the same for all actuators). The intersection with the horizontal axis is moved towards larger displacements.

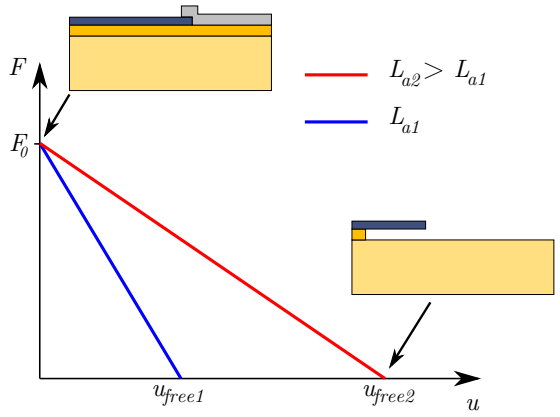

Figure 4.3: *Force-displacement relationship for an actuator of length L_{a1} (blue) and L_{a2} (red).*

As the strain in the actuator beam is always small, the variation of the cross-sectional area can be neglected and $S_a \backsim S_{a0}$.

4.2.2 The case of the specimen beam

In every micromachine, the load F is induced by the presence of a specimen beam attached to the actuator beam. The characteristic dimensions and properties of the specimen beam are the following:

ε^{mis}	mismatch strain of the specimen resulting from the deposition and subsequent fabrication steps;
σ, ε and ε^{mech}	stress, total, and mechanical strains in the specimen beam after release, respectively;
E and ν	Young's modulus and Poisson ratio of the specimen material, respectively;
L_0	specimen length at the test temperature before chemical release;
u	imposed displacement after release. It is the same displacement as in Fig. 4.2;
S and S_0	current (after release) and initial (before release) cross-sectional areas of the specimen beam, respectively.

The total strain inside the specimen beam is given by

$$\varepsilon = \ln\left(\frac{L_0 + u}{L_0}\right) = \varepsilon^{mech} + \varepsilon^{mis}. \tag{4.6}$$

It must be noted that in Eq. 4.6, the small strain assumption is not made as the specimen can undergo large strain in the case of testing of a ductile material.

The mechanical strain inside the specimen beam can thus be calculated through the measurement of u and ε^{mis}.

The stress in the specimen beam is given by the force F divided by the current cross-sectional area:

$$\sigma = \frac{F}{S} = E_a \frac{S_a}{S}\left(\frac{-u}{L_{a0}} - \varepsilon_a^{mis}\right). \tag{4.7}$$

These last two equations are the most important ones as they enable to determine the stress-strain response of the specimen material.

Similarly to the actuator beam, the behaviour of the specimen beam can also be drawn in the force-displacement diagram (Fig. 4.4). The case

of a ductile material is presented here. The force-displacement diagram starts at zero displacement. The force at zero displacement corresponds to the internal force in the specimen beam consecutive to deposition of the specimen material. A positive force corresponds to tensile internal stress in the specimen (Fig. 4.4) whereas a negative force corresponds to compressive stress. Then, the force linearly increases with displacement. This results from the elastic behaviour of the tested material. The slope then starts decreasing as the specimen plastically deforms (specific case of a ductile metallic film). The force reaches a maximum. At this point, plastic localisation occurs and the force drops till fracture of the specimen beam. For a specific micromachine, each beam (actuator and specimen) has its own force-displacement curve. Before release, the displacement u is zero, the force inside the specimen beam is minimum and the force inside the actuator beam is maximum. After release, the displacement increases till reaching the intersection point between the two characteristic curves. This point is the equilibrium condition expressed mathematically by Eq. 4.5.

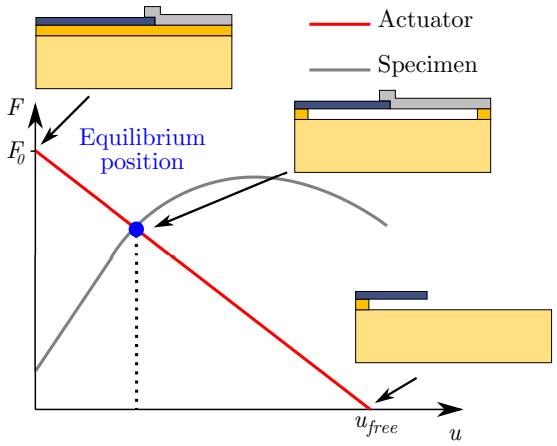

Figure 4.4: *Force-displacement relation for the actuator (red) and specimen (gray) beams.*

4.3 Design of an ideal test structure

Section 4.2 was meant to answer the question "How to extract stress and strain from a specific micromachine?". In this section, the question is asked in the other way: "What should the dimensions of a specific micromachine be in order to extract stress and strain accurately?". The goal of this section is thus to specify the set of constraints on the design required to produce valid measurements. By "valid measurements", it is meant that the error on the stress and the mechanical strain is smaller than the prescribed values.

4.3.1 General design considerations

The possible sources of errors lie in the determination of:

1. u, with the error noted Δu (defined as a positive value);
2. ε_a^{mis} and ε^{mis}, with the error noted $\Delta\varepsilon_a^{mis}$ and $\Delta\varepsilon^{mis}$, respectively (defined as positive);
3. $\frac{S_a}{S}$, which comes from inaccuracies in the measurement of the widths and thicknesses at the test temperature;
4. E_a.

The last two errors, which only affect the evaluation of the stress (see Eq. 4.7) can easily be taken into account in the analysis, even though they might be difficult to quantify. They do not directly enter into the design procedure.

In order to simplify the design procedure, Eq. 4.6 and Eq. 4.7 can be re-written with the engineering definition of strain suitable for small strains. This gives Eq. 4.8 and Eq. 4.9.

$$\varepsilon^{mech} = \frac{u}{L_0} - \varepsilon^{mis} \tag{4.8}$$

$$\sigma = E_a \frac{S_a}{S} \left(\frac{-u}{L_{a0}} - \varepsilon_a^{mis} \right). \tag{4.9}$$

Considering displacement and both mismatch strains as the only sources of errors, the design procedure proposed now consists of determining the range of dimensions for the actuator and test specimens, such as to respect the imposed maximum acceptable errors $\Delta\varepsilon$ and $\Delta\sigma$, for given Δu, $\Delta\varepsilon_a^{mis}$ and $\Delta\varepsilon^{mis}$. The following nondimensional geometrical quantities are defined: $\alpha = \frac{L_0}{\Delta u}$, $\beta = \frac{L_{a0}}{\Delta u}$, $R = \frac{S_a}{S}$.

Based on Eq. 4.8, the first condition on the strain writes

$$\frac{1}{\alpha} + \Delta\varepsilon^{mis} < \Delta\varepsilon \quad \text{or} \quad \alpha > \frac{1}{\Delta\varepsilon - \Delta\varepsilon^{mis}}. \tag{4.10}$$

Based on Eq. 4.9, the second condition on the stress writes

$$RE_a \left(\Delta\varepsilon_a^{mis} + \frac{1}{\beta} \right) < \Delta\sigma \quad \text{or} \quad R < \beta \frac{\Delta\sigma}{E_a} \frac{1}{\beta\Delta\varepsilon_a^{mis} + 1}. \tag{4.11}$$

Eq. 4.10 and Eq. 4.11 mean that knowing the error on the mismatch strains ($\Delta\varepsilon_a^{mis}$ and $\Delta\varepsilon^{mis}$) and the Young's modulus of the actuator material (E_a), one can directly infer the maximum error on the strain and stress measured with a specific test structure (fixed α, β and R). In other words, for a desired precision on stress and strain, the geometry of each micromachine must follow Eq. 4.10 and Eq. 4.11.

The design must also ensure that the dimensions of the test structures are varied in order to cover the spectrum of strains of interest, for example, between ε_{min} and ε_{max}. In order to derive these constraints on the dimensions, one needs to be more specific about the expected material behaviour which can be divided into two broad classes.

1. The first class involves elastic behaviour, which is, for most materials, linear and associated to small strains, often smaller than 1%. In brittle materials, the elastic response terminates with unstable fracture when reaching a critical stress. This behaviour puts the largest constraint on the design as it requires measuring small strains accurately.

2. The second class involves plastic (or viscoplastic or creep) behaviour, which is usually associated to moderate (1% to 5%) and sometimes large strains (10% and even more in bulk metals). As a first approximation, the level of stress does not change much during plastic deformation and can be set equal to the yield stress σ_0. In ductile materials, homogeneous plastic response lasts for several percents of straining, up to reaching the critical fracture strain or the necking condition [103].

The design procedures for both classes of materials will be detailed in the next sections.

4.3.2 Design for small strain elastic behaviour

It is first assumed that the test material has a Young's modulus E. The following nondimensionnal modulus is introduced $E^* = \frac{E}{E_a}$. Small strain elastic behaviour enables to write Hooke's law for the test material (Eq. 4.12)

$$\sigma = E\varepsilon_{mech}. \tag{4.12}$$

The expression of stress (Eq. 4.9) and strain (Eq. 4.8) in the case of small displacement are both introduced in Eq. 4.12 which leads to an expression for the displacement

$$u = \frac{E^*\varepsilon^{mis} - R\varepsilon_a^{mis}}{\frac{E^*}{L_0} + \frac{R}{L_{a0}}}. \tag{4.13}$$

Introducing the expression of the displacement u_i corresponding to a mechanical strain ε_i, i.e., $u_i = L_0(\varepsilon_i^{mech} + \varepsilon^{mis})$, into Eq. 4.13 leads to

$$R\mid_{\varepsilon_i} = E^*\beta\frac{-\varepsilon_i^{mech}}{\beta\varepsilon_a^{mis} + \alpha\varepsilon_i^{mech} + \alpha\varepsilon^{mis}}, \tag{4.14}$$

giving lower and upper bounds for the variation of R in order to cover the strain range $[\varepsilon_{min}, \varepsilon_{max}]$

$$\beta\frac{-\varepsilon_{min}}{\beta\varepsilon_a^{mis}+\alpha\varepsilon_{min}+\alpha\varepsilon^{mis}} \leqslant \frac{R}{E^*} \leqslant \beta\frac{-\varepsilon_{max}}{\beta\varepsilon_a^{mis}+\alpha\varepsilon_{max}+\alpha\varepsilon^{mis}}. \quad (4.15)$$

The nondimensional parameter $\frac{R}{E^*}$ represents the stiffness ratio between the actuator and specimen material. It controls whether a valid result can be extracted from a micromachine.

4.3.3 Design for plastic behaviour

The same approach can be followed for a material undergoing moderate to large plastic deformations. The nondimensional parameter $Y = \frac{\sigma_0}{E_a}$ is introduced. This time, the test material is considered to have no strain hardening ($\sigma = \sigma_0$). Using the logarithmic definition of stress (Eq. 4.7), the lower and upper bounds for R write

$$\frac{\beta}{\alpha-\alpha\exp(\varepsilon_{min}+\varepsilon^{mis})-\beta\varepsilon_a^{mis}} \leqslant \frac{R}{Y} \leqslant \frac{\beta}{\alpha-\alpha\exp(\varepsilon_{max}+\varepsilon^{mis})-\beta\varepsilon_a^{mis}}. \quad (4.16)$$

The nondimensional parameter $\frac{R}{Y}$ represents the stiffness ratio between actuator and specimen material during plastic deformation and controls whether a valid result can be extracted from a micromachine.

This design procedure was made such as to generate results with an imposed constant maximum error on the stress $\Delta\sigma$ and on the mechanical strain $\Delta\varepsilon$. Another more advanced design procedure consists in setting the maximum acceptable error on the evaluated mechanical strain ε^{mech} as a fixed fraction $x\,|_\varepsilon$ of it, i.e. $x\,|_\varepsilon\,\varepsilon^{mech}$, and the maximum acceptable error on the stress σ as a fixed fraction $x\,|_\sigma$ of it, i.e. $x\,|_\sigma\,\sigma^{mech}$, i.e., a constant relative error. This second design procedure is more attractive when dealing simultaneously with large strain plasticity and small strain elastic behaviour. This procedure is developed in Appendix A.

4.3.4 Illustration of practical design rules

As already stated in Section 4.1, one of the idea of the self actuated micromachine concept is to use MEMS microfabrication techniques to

pattern thin films, enabling to process thousands of elementary structures on a single wafer. This allows either using only a small part of them depending on the best suited design with respect to the test material or enabling high throughputs of data with statistical relevance. Practical implementation of the technique, requiring the release of long flat actuators and test specimens, as well as an objective toward miniaturising and multiplying the number of tests pushes for minimising the length of the actuator and test specimen. Hence, an additional constraint is to select the minimum α and the minimum β.

For the sake of illustration, a specific design is now addressed based on a set of parameters consistent with Al and Al alloys thin film studied, making use of a silicon nitride actuator with: $E_a = 235\,\text{GPa}$, $\varepsilon_a^{mis} = -0.003$, $\Delta\varepsilon_a^{mis} = 0.0001$ [7], as well as no mismatch strain in the test specimen, i.e., $\varepsilon^{mis} \backsimeq \Delta\varepsilon^{mis} \backsimeq 0$. The maximum error on the stress is imposed to be equal to 30 MPa, i.e., $\frac{\Delta\sigma}{E_a} = 0.00013$, considering that typical metallic or ceramic submicrometer films will show stresses reaching at least 250 MPa and being sometimes larger than 1 or 2 GPa. The maximum error on the strain is taken equal to 0.0005 and comes from the accuracy of the displacement measurement (see Section 6.2).

Hence, from Eq. 4.10, the length of the specimen beam must comply with $\alpha > \frac{1}{0.0005} = 2000 = \alpha_{min}$. Based on Eq. 4.11, the asymptotic behaviour for $\beta \to \infty$ imposes $R < 1.3$.

Fig. 4.5 shows the variation of the upper bound of R as a function of β set by the conditions of Eq. 4.11.

Design for small strain elastic behaviour

The design of a specific set of tensile testing stages allowing the measurements of the elastic behaviour up to the fracture stress is now worked out for materials with $\frac{E}{E_a}$ around 0.4. The bounds of the minimum and maximum strains of interest are set between $\varepsilon_{min} = 0.0005$ (0.05%) and $\varepsilon_{max} = 0.015$ (1.5%). As explained above, α is chosen equal to the minimum admissible value $\alpha_{min} = 2000$ ($L_0 = 100\,\mu\text{m}$).

Fig. 4.5 shows the variation of R as a function of β for different strains

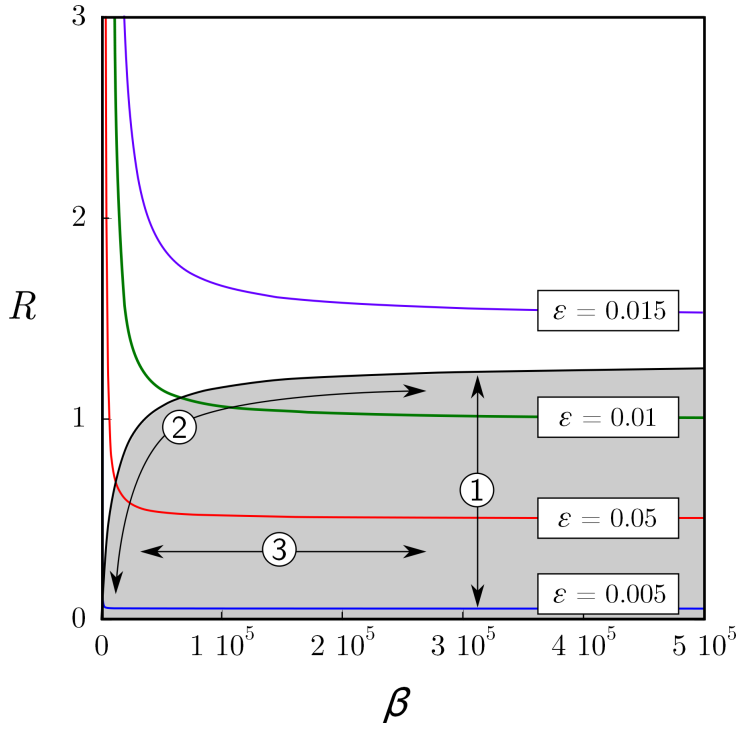

Figure 4.5: *Illustration of design methodology imposing a constant maximum acceptable error on strain (here 0.0005) and stress (here* $30\,\mathrm{MPa}$*). The constraint on strain imposes a minimum value for the specimen length which is taken to be equal to* $100\,\mu\mathrm{m}$ *for all relations shown on the graph. The constraint on the stress is responsible for the grey zone. This zone indicates the range of valid dimensions of the tensile testing stages elements in terms of the ratio* R *and* β*,* R *being the ratio of the cross-sectional areas of the specimen and actuator beams and* β *being the ratio of the actuator length* L_{a0} *divided by the error on the displacement measurement* Δu*. The other lines determine the* R *versus* β *relation for different strains. This design is made for a material having a linear elastic regime using the following set of parameters:* $\alpha = 2000$*,* $E_a = 235\,\mathrm{GPa}$*,* $E = 70\,\mathrm{GPa}$*,* $\varepsilon_a^{mis} = -0.003$*,* $\Delta\varepsilon_a^{mis} = 0.0001$*,* $\varepsilon^{mis} = \Delta\varepsilon^{mis} = 0$*. Numbers 1, 2, and 3 indicate three possible design strategies as explained in the text.*

as given by Eq. 4.14. Fig. 4.5 first indicates that the imposed constraint Eq. 4.11 on the maximum error on the stress does not allow reaching strains equal to 0.015 as initially envisioned. Hence, for the largest strains, one should either relax the acceptable error on the stress or improve the accuracy on the mismatch strain $\Delta\varepsilon_a^{mis}$. This conclusion motivates also the need for a design method based on a relative error and not a fixed error.

Different design strategies can be followed to fix the dimensions of the test structures (Fig. 4.5):

1. Strategy 1 proposes to choose a constant sufficiently long actuator length. This approach has two disadvantages. The first one is that it requires long actuators which cover lots of space on the substrate and are more prone to microfabrication problems such as stiction or geometrical defect. The second is that this approach requires changing the ratio R of the cross sections for each specimen. For reasons related to the chemical release of the structure discussed later (Section 4.4), it is better not to change too much the ratio of cross-sectional area within a set of testing stages. Moreover, some mechanical properties might depend on the width.

2. Strategy 2 not only optimises space but also requires changing the ratio of the cross-sectional area from specimen to specimen.

3. Strategy 3 keeps the ratio of the cross-sectional area constant while changing the actuator length, but it does not allow encompassing a very wide range of strains.

Now, R versus β is shown in Fig. 4.5 for a fixed value of the specimen length and a larger strain range can be covered by varying this length, i.e., changing α. The effect of changing α is shown in Fig. 4.6. For instance, changing α from 2000 to 10000 with $R = 0.8$ and $\beta = 40000$, leads to a change of the corresponding minimum mechanical strain that can be measured from 0.0071 to 0.0048, as computed from Eq. 4.14.

As a result, the design chosen for one set of test structures on generation 3 and 4 is based on a constant R value but with evolving β and α. For simplicity, a constant length $L_0 + L_{a0}$ is used.

Design for plastic behaviour

The same approach can be followed for the design of a set of tensile testing stages devoted to the measurement of the stress and strain evolution in a plastically deforming material characterised by a yield stress σ_0 and a range of strain typically between 0.01 and 0.1. Again, let us specify a value for σ_0, for example, 300 MPa, giving $Y = \frac{\sigma_0}{E_a} = 0.004$. Fig. 4.7 shows the variation of R as a function of β for different strains as given by one of the bound of Eq. 4.16. Strategy 3 based on a constant R allows covering a wide range of strains within the plastic regime. Evaluation of the plastic behaviour is much easier to implement with the present approach compared to the low-strain elastic behaviour.

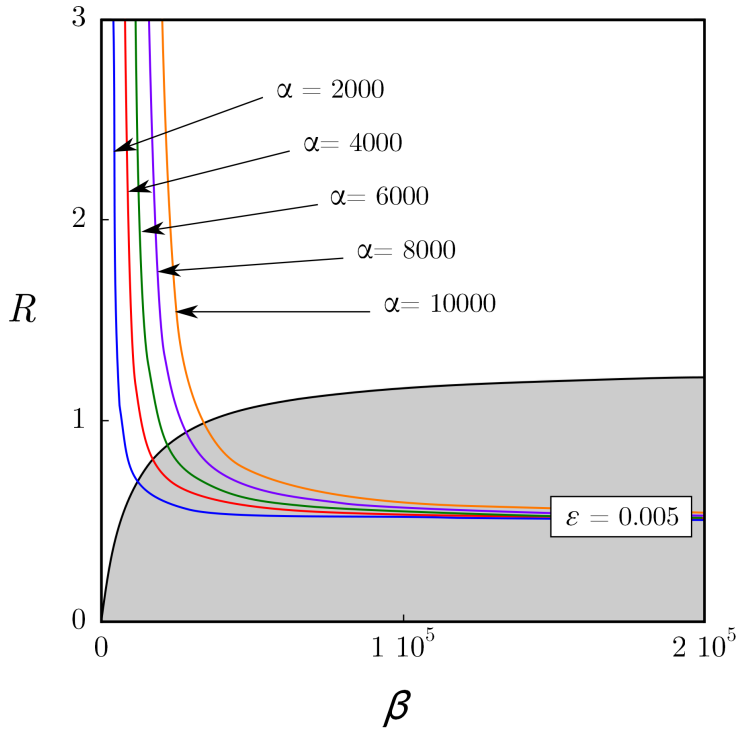

Figure 4.6: *Illustration of design methodology imposing a constant maximum acceptable error on strain (here 0.0005) and stress (here* 30 MPa*). The constraint on the stress is responsible for the grey zone. This zone indicates the range of valid dimensions of the tensile testing stages elements in terms of the ratio R and β, R being the ratio of the cross-sectional areas of the specimen and actuator beams and β being the ratio of the actuator length L_{a0} divided by the error on the displacement measurement Δu. The other lines determine the R versus β relation for a fixed different strain but with varying specimen length, i.e. varying α. This design is made for a material having a linear elastic regime using the following set of parameters:* $\varepsilon_i = 2000$, $E_a = 235\,\mathrm{GPa}$, $E = 70\,\mathrm{GPa}$, $\varepsilon_a^{mis} = -0.003$, $\Delta\varepsilon_a^{mis} = 0.0001$, $\varepsilon^{mis} = \Delta\varepsilon^{mis} = 0$.

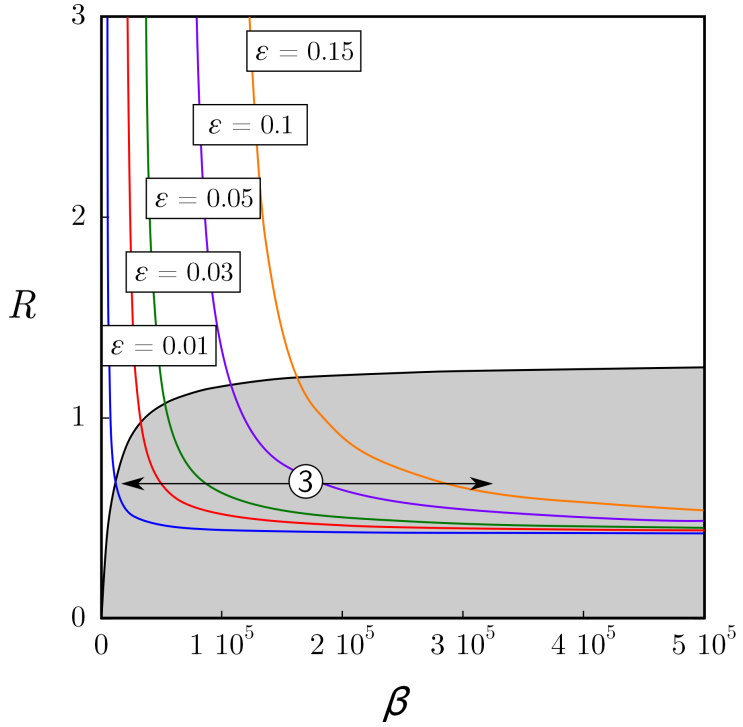

Figure 4.7: *Illustration of design methodology imposing a constant maximum acceptable error on strain (here 0.0005) and stress (here* $30\,\mathrm{MPa}$*). The constraint on strain imposes a minimum value for the specimen length which is taken to be equal to* $100\,\mu\mathrm{m}$ *for all relations shown on the graph. The constraint on the stress is responsible for the grey zone. This zone indicates the range of valid dimensions of the tensile testing stages elements in terms of the ratio* R *and* β*,* R *being the ratio of the cross-sectional areas of the specimen and actuator beams and* β *being the ratio of the actuator length* L_{a0} *divided by the error on the displacement measurement* Δu*. The other lines determine the* R *versus* β *relation for different strains. This design is made for a material having a plastic yielding regime (assuming a perfectly plastic behaviour) using the following set of parameters:* $\alpha = 2000$*,* $E_a = 235\,\mathrm{GPa}$*,* $\sigma_0 = 300\,\mathrm{MPa}$*,* $\varepsilon_a^{mis} = -0.003$*,* $\Delta\varepsilon_a^{mis} = 0.0001$*,* $\varepsilon^{mis} = \Delta\varepsilon^{mis} = 0$*. Number 3 indicates the best strategy to follow in order to cover a wide range of strain.*

4.4 Constraints from application to a real test structure

Up to this point, Section 4.3 was meant to provide the required dimensions of an ideal micromachines (α, β, and R) in order to extract stress and strain with a prescribed level of error. The real implementation of the theoretical requirements defined in Section 4.3 needs some adaptations. This section aims at reviewing all the mechanical and geometrical constraints that arise when designing the real geometry of the test structures. The configuration of the mask layout are presented first (Section 4.4.1). Then, all the additional constraints coming from the real implementation are detailed (Section 4.4.2 to Section 4.4.5). Although some constraints are inherent to the fabrication steps, a whole chapter (Chapter 5) is dedicated to the fabrication process. This section neither extends on the measurements that must be performed on the structures in order to determine the parameters involved in the equations of Section 4.2. Indeed, it will be the scope of Chapter 6.

4.4.1 Mask layout

Fig. 4.8a shows the overall layout of a wafer processed with the generation 3 set of masks. Fig. 4.8b enlightens a die which is reproduced several times on the wafer (5 times in generation 3). This die contains all the structures necessary for proper extraction of the mechanical properties of the specimen material. This comprises the standard structures for uniaxial tensile testing, the structures designed for extraction of some parameters needed in the equations of Section 4.2 (see Chapter 6) and some other structures like the notched specimens (see Chapter 7). Fig. 4.8c shows a set of the so called "standard" test structures. Within such a set, the width of the actuator and specimen beam are kept constant and the only varying parameter is the length of both beams in order to sweep the whole tensile behaviour from small elastic strain to fracture. Finally, Fig. 4.8d shows a magnified SEM picture of a single test structure where the overlap, the cursors and the dogbone are clearly visible. The origin of these differences with the ideal test structures from Section 4.3 are

justified in the following sections (Section 4.4.2 to Section 4.4.5).

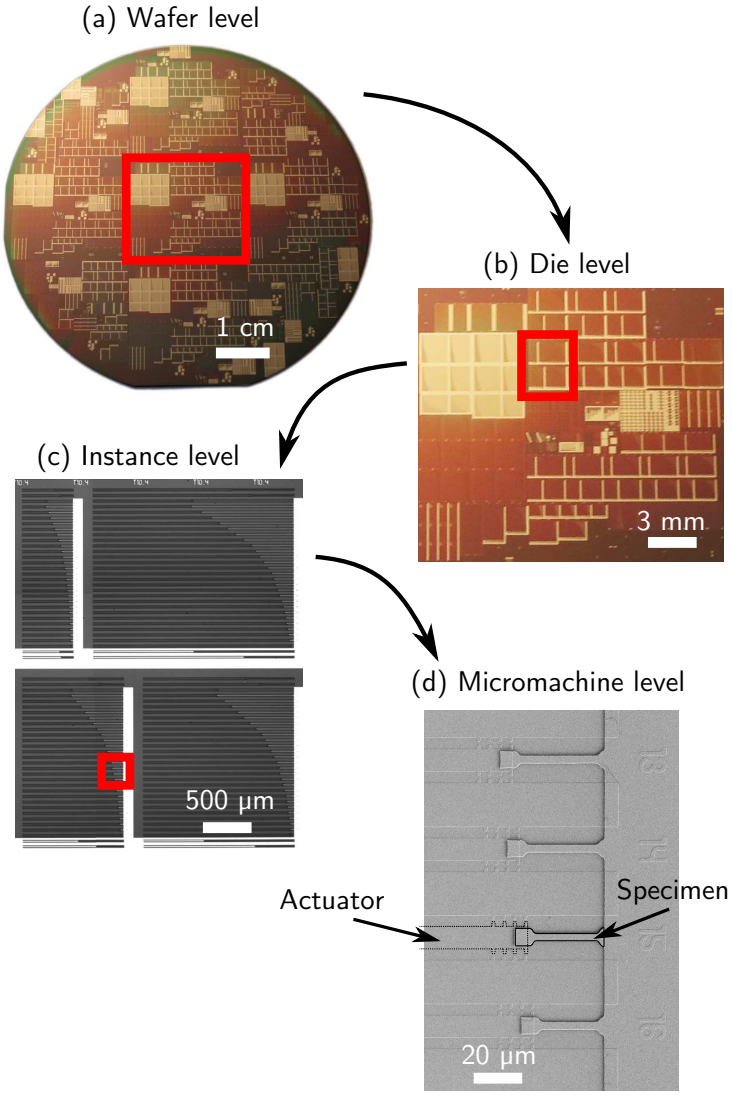

Figure 4.8: *Layout of the "generation 3" set of masks.*

4.4.2 Constraints on the width of beams

The release of internal stresses inside actuator and specimen beams is performed through the etching of the sacrificial layer located underneath the two beams. The etchant can only etch layers by direct contact. In the case of an isotropic etching of the sacrificial layer located under a structure, the etching will start from the sides of the structure, then continues until the center of the structure is released as depicted in Fig. 4.9. The wider is the beam, the longer is the etching time. This has several consequences:

- Actuator and specimen beams cannot be too wide as etching selectivity is never infinite (Section 5.5);
- Actuator beam must always be wider than the attached specimen beam so that the latter is released first (Fig. 4.9c). Indeed, possible non-uniformity of etching could cause the release of a small portion of the specimen beam. If the actuator is released at that time, all the strain imposed by the actuator beam will be concentrated inside that small portion, creating non-uniform loading conditions and premature fracture;
- Widths of actuator and specimen beams should be kept constant within one series of micromachine. This ensures that the structures of the same instance[4] require the same time to be released. This also lowers the number of measurements to be performed as two width measurements (actuator and specimen beam) are enough within the instance.

It must be noted that loading does not occur gradually. The actuator releases its internal stress only when all the sacrificial layer under the actuator beam is fully etched away. The loading rate is thus not controlled and is probably very fast. Moreover, as the test structures of one

[4]The word "instance" will be used throughout this work to speak about structures located at in the same area of the wafer and having the same dimensions (shape, width, total length).

instance have the same actuator width, they are all released at the same time and the strain rate applied is different from one test structure to the other. This is a limitation of this concept.

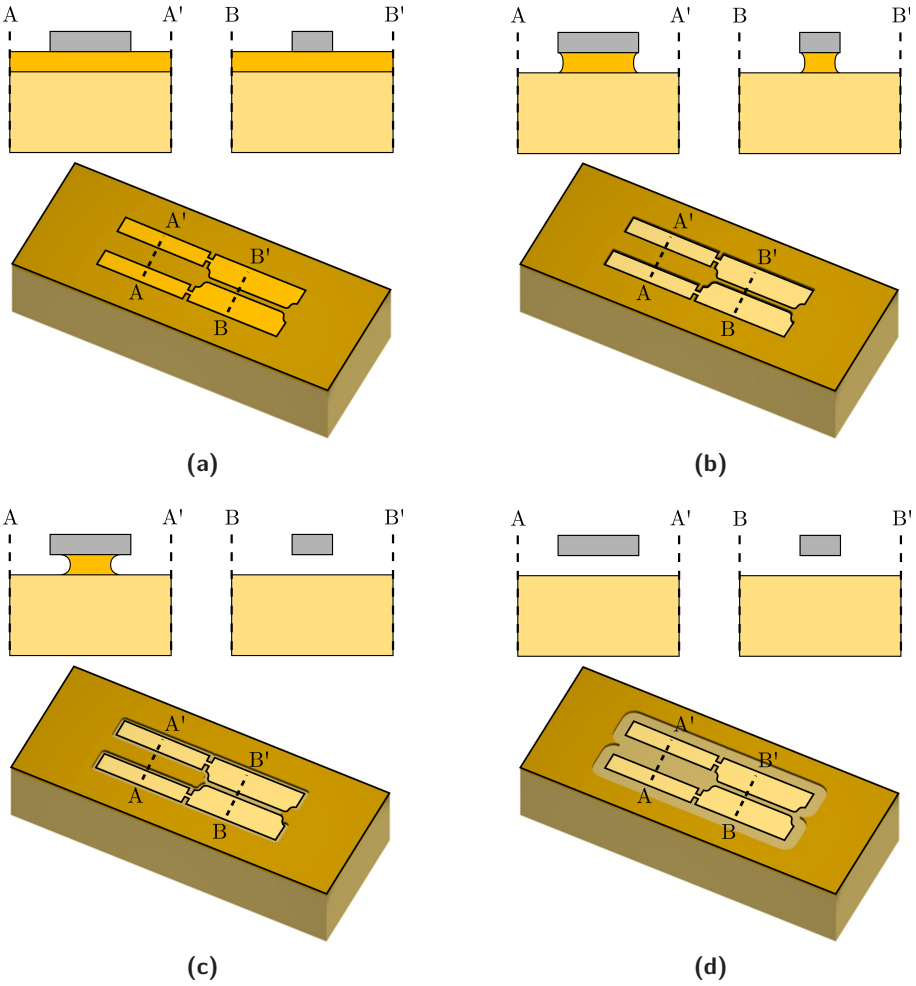

Figure 4.9: *Evolution of the etching of a sacrificial layer located under a micromachine. (a) test configuration before etching, (b) beginning of etching, nothing is released yet, (c) the specimen beam is released, (d) the actuator beam is released.*

4.4.3 Constraints on the overlap region

In the ideal case of Section 4.3, the actuator and specimen beams are considered as rectangular beams of length L_{a0} and L_0 respectively with no overlap. In the real case, there has to be an overlap of a beam on the other one to ensure a good connection between the beams. The zone where actuator beam and specimen beam meet can be divided in four parts (Fig. 4.10b) which all require special care in the design procedure.

- The "overlap" is the part of the specimen material located just on top of the actuator beam;
- The "uniaxially deformed zone" is the part of the specimen beam subjected to pure uniaxial tension;
- The "dogbone" is the part of the specimen beam located on both ends of the beam where the width is not uniform;
- The "connection" is the part of the specimen beam which connects the overlap to the dogbone. In other words, it is the part of the specimen material where the thickness is the lowest due to deposition process features.

Generation 1 set of masks consisted in structures with rectangular shapes for both beams as shown in Fig. 4.10a. The structures worked for at small deformation beams but breaking prematurely occurred just at the connection when the strain in the uniaxially deformed zone was still lower than the fracture strain of the specimen material. This was because the overlap of the specimen beam on the actuator beam is not at the same level than the specimen beam itself. The step created by the overlap is responsible for a stress concentration in this region. Fracture was thus always occurring at the connection first.

The idea was then to strengthen the connection so that fracture can occur in the part of specimen subjected to uniaxial loading conditions. The solution designed in generation 2 set of masks was to use a dogbone shape on both sides of the specimen beams. Dogbones enable to increase

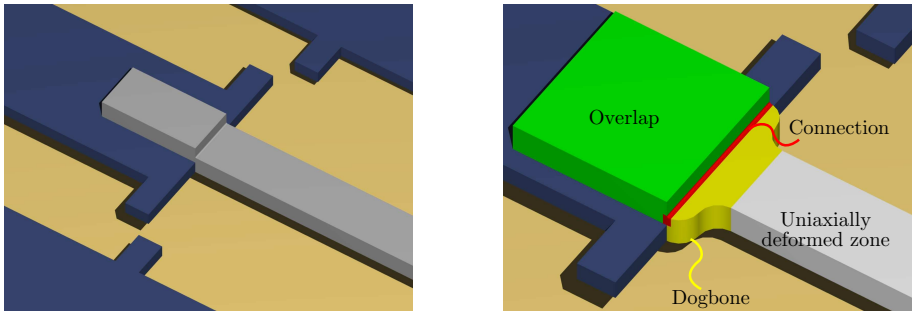

Figure 4.10: *Design of the connection between actuator and specimen beam: (a) no dogbone for generation 1, (b) dogbone for further generations.*

the section of the specimen material at the connection with respect to the uniaxially deformed zone. There is still a stress concentration due to the step but most of the stress is concentrated in the uniaxially deformed zone of length L_0 used in all equations of Section 4.3. However, the dogbone design suffers from two main drawbacks. The first one is that dogbones increase $R = \frac{S_a}{S}$, which according to Eq. 4.11, should be lower than a prescribed value. Eq. 4.11 is thus more difficult to satisfy. The second disadvantage is that dogbones are not taken into account in the above calculations.

The stress concentration in the connection should be kept in mind when choosing the thicknesses of the actuator and of the specimen layers. The specimen layer should always be thicker than the actuator layer. This is an additional constraint on the choice of the best ratio R suitable for a specific material[5].

Still concerning the overlap region, the length of the specimen part overlapping the actuator beam has to be determined. On the one hand, it cannot be too long in order to avoid curvature due to a bilayer of stres-

[5]One solution not investigated in this thesis is to deposit a filler layer before the specimen layer deposition. This filler layer would be part of the sacrificial layer and would decrease the step in the overlap region.

sed films. On the other hand, it cannot be too short to ensure sufficient adhesion during tensile testing. Finite element (FE) simulations have been performed to analyse the impact of the length of the overlap on the curvature of the bilayer [46]. A 10 µm long overlap was selected for generation 2, 3 and 4 set of masks as the FE simulations predicted negligible bending and out of plan displacement. The selected length corresponds to less than 1% of the total length of each micromachine. With this overlap, no adhesion fracture was noticed during tensile testing of Al and Al alloys. This was mainly due to the good adhesion between silicon nitride (actuator material) and Al. Note that in the case of poor adhesion between the two layers, a thin adhesion layer can be deposited prior to specimen layer deposition (usually 5 nm of titanium or chromium depending on the etching selectivity). The overlap is always designed to be 2 µm narrower than the actuator width in order to anticipate possible misalignment between actuator mask and specimen mask (see Fig. 4.10b).

4.4.4 Constraints on the symmetry

A general trend to follow in thin film mechanical testing is to keep every structure symmetrical. This ensures that the release of internal stresses by etching of the sacrificial layer occurs uniformly so as to perform pure uniaxial tensile test (no shear component). Cursors are thus designed on both sides of the actuator tip. Reference and moving cursors have also the same size and are in the same material to minimise the error made on the measurement of displacement u.

4.4.5 Constraints on the anchors

Actuator and specimen beams are connected to anchors. Anchors are big squares designed large enough to ensure that underetching will not release them from the substrate. Reference cursors should also be connected to fixed unreleased structures. Typically anchors are at least 100 µm wide. It must be noted that underetching of the anchors should be kept minimum as even a partially released structure can deform a little bit

and underetching is not taken into account in the equations of Section 4.3. However, FE simulations showed that taking the underetching into account induces very negligible correction to the calculated stress and strain in the specimen beam [46].

4.4.6 Concluding remarks and notations

The design requirements from Section 4.4 have been learned by the successive generations of masks. On the opposite, the design requirements described in Section 4.3.1 to Section 4.3.3 are determined from the accuracy of measurements (Δu, $\Delta\varepsilon_a^{mis}$, $\Delta\varepsilon^{mis}$), from the used materials properties (E, E_a, ε^{mis}, ε_a^{mis}, σ_0) and from the expected accuracy on stress and strain ($\Delta\sigma$ and $\Delta\varepsilon$, respectively). This procedure assumes that the mechanical behaviour of the test material is first elastic (E known) then perfectly plastic (σ_0 known). Of course, this assumption is not correct and the properties are expected to vary with the thickness making it difficult to guess the mechanical behaviour when designing the structures. As a consequence, the design requirements of Section 4.3.1, Section 4.3.2 and Section 4.3.3 should be used as guidelines. Moreover, the surface area for a set of masks is sufficiently large to design many structures with varying geometrical parameters in order to capture different types of mechanical behaviour even for different materials. As a result, all the structures located on a set of masks will not be suitable for accurate determination of a specific mechanical behaviour of the test material. But it is the role of the user to select the most accurate ones.

The large number of elementary structures (about 5000 to 10000 on a single 3-inch Si wafer) requires a specific convention for grouping the structures. Series of micro tensile stages with similar geometry (same actuator width and specimen width) are grouped within sets of 30 structures (or "instances"). Within one set, the total length of the couple actuator and specimen structure is kept constant while the actuator length is progressively increased. Each set is named as "Tx-y L" where:

- x is the width of the actuator beam and is either 10 µm either 15 µm;

- y is the width of the specimen beam and the different values are: 1, 2, 4, 6, 8 and 10 µm;
- L is the overall length of each test structure and is equal to 500, 1000, 1500 or 2000 µm.

Within one set, the tensile structures are numbered from 1 to 30. Increasing the number corresponds to increasing the deformation applied to the specimen after release.

Chapter 5

Fabrication process

The main steps required to fabricate a set of on-chip test structures are described in this chapter. The properties expected for each involved layer will be detailed. For each step, the conditions and materials used for the specific testing of pure Al and Al alloys films will be given. The standard process flow is shown in Fig. 5.1.

The processing of Fig. 5.1 has been entirely performed within the WINFAB[1] facilities. The processing steps of Fig. 5.1 remain the same if the coating/film is deposited (step e) outside WINFAB. Another interested team can thus deposit its material on pre-processed wafers (Fig. 5.1a to Fig. 5.1d). After deposition, the patterning of the coating (Fig. 5.1e) and etching of the sacrificial layer (Fig. 5.1f) are performed within WINFAB for extraction of the mechanical properties of the coating.

[1]WINFAB stands for "Wallonia Infrastructure Nano FABrication" and is a clean-room area used for microfabrication of electronic and MEMS devices.

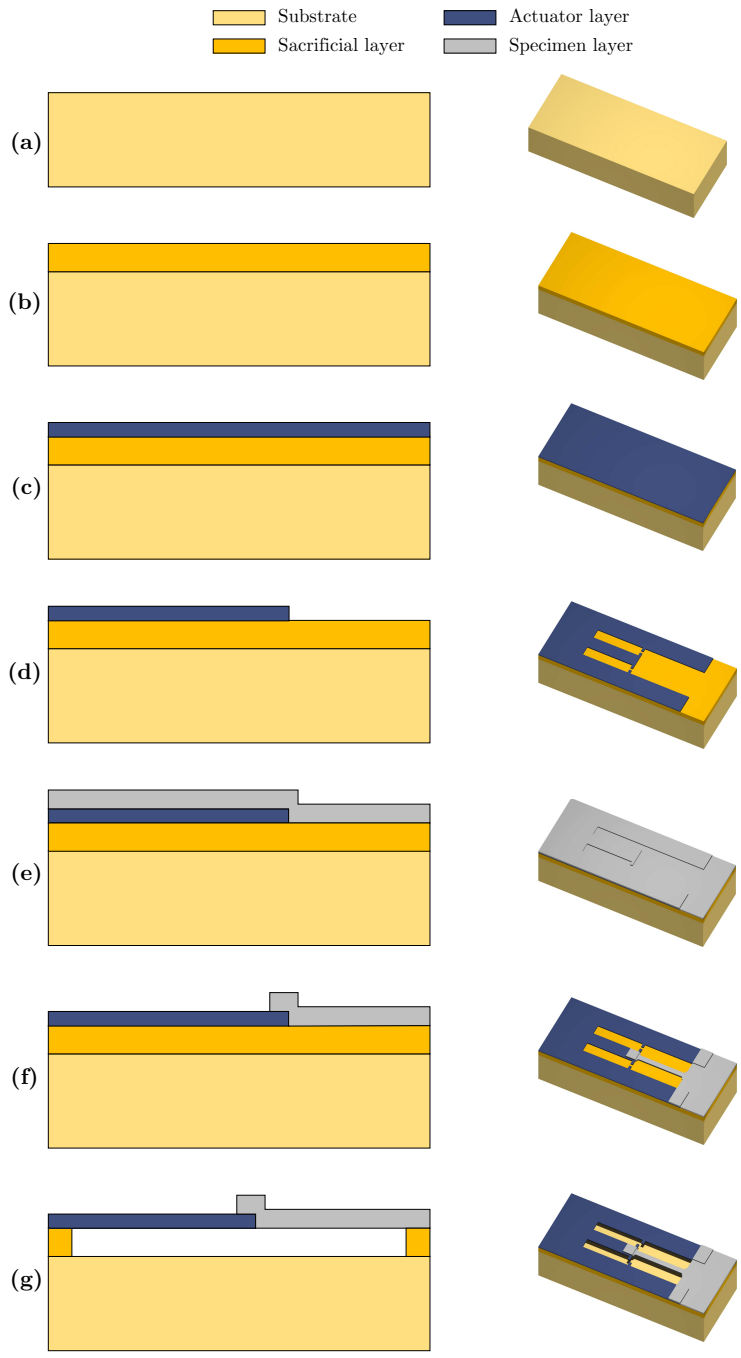

Figure 5.1: *Fabrication process involving (b) the sacrificial layer deposition, (c) the actuator layer deposition, (d) the patterning of the actuator layer, (e) the specimen layer deposition, (f) the patterning of the specimen layer and (g) the etching of the sacrificial layer.*

5.1 Wafer selection

Fabrication in WINFAB implies that the substrates used for processing are silicon wafers with a diameter of 3 inches and a thickness equal to 380 µm polished on the front face. The wafers are made of pure monocrystalline silicon. The orientation is given in Fig. 5.2.

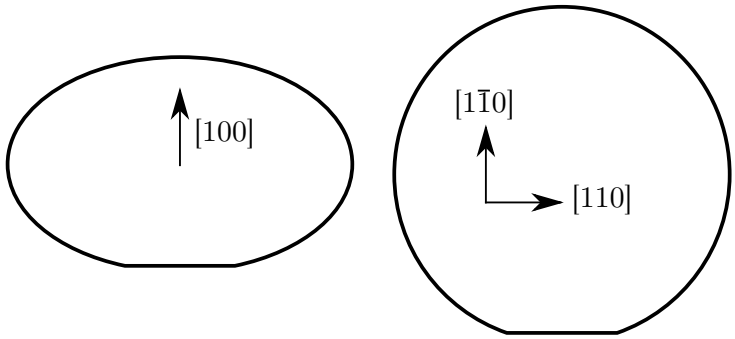

Figure 5.2: *Silicon substrate orientation.*

A priori, any wafer can be used for the subsequent steps. But as the internal stress in each film is an important parameter in order to determine the mismatch strain or the Young's modulus [7], the wafers showing a monotonic curvature (Fig. 5.3b) must be selected. Indeed, wafer curvature method [83] is used for stress measurement and monotonic curved substrate is a first requirement in order to produce accurate measurement. The curvature is determined by running a profilometre tip along one axis of the wafer (Fig. 5.3a).

The whole process can be performed on non-monotonic curved wafers (Fig. 5.3c) but at least one suitable wafer has to be used throughout the process for wafer curvature measurement at each step (one measurement before and after deposition of one layer and before and after any thermal treatment).

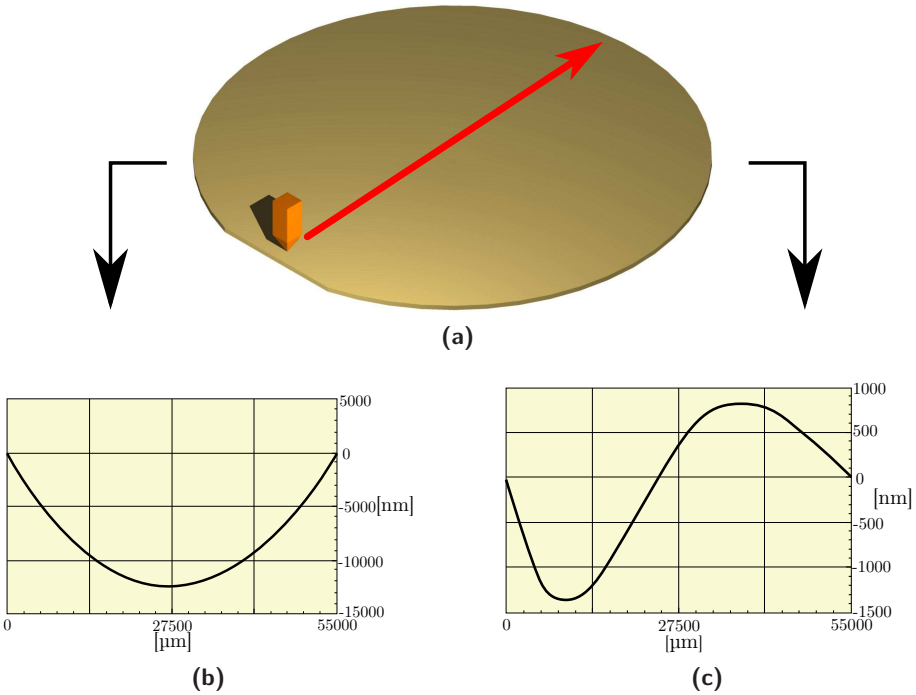

Figure 5.3: *Curvature measurement performed with a profilometre (b) monotonic profile, (c) non-monotonic profile.*

5.2 Sacrificial layer

The first layer to be deposited is the sacrificial layer. This layer is the one that will be etched away at the end of the process in order to release the upper layers. The major requirement concerning this layer is the etching selectivity. The etch rate ratio between the sacrificial layer and the other layers has to be as high as possible. This ensures that the release step occurs without damaging the structures or modifying the dimensions, mainly the actuator and specimen thicknesses.

No particular mechanical property is required for this layer. The selected material must sustain all the conditions of the subsequent processing steps (e.g. heating, etching). The roughness should be as small as possible because it will be transferred to the top layers. Sacrificial layers with too high internal stresses should be avoided. Indeed, residual sacrificial layer on released structures could lead to more complex loading configuration such as out of plane bending instead of pure uniaxial tensile testing.

In all the applications addressed further regarding Al specimens, the sacrificial layer is a 1 µm-thick PECVD (Plasma Enhanced Chemical Vapour Deposition) silicon oxide layer. The deposition is made at 300 °C with a gas flow of $SiH_4/N_2O/N_2$ in the proportion 100/700/350 sccm. PECVD SiO_2 is used because it is a well-known material in MEMS processing. As a consequence, the etching selectivity with respect to other materials involved in the fabrication process is already determined. Hydrofluoric acid (HF) is generally used to etch silicon oxide. PECVD SiO_2 is used instead of thermal SiO_2[2] because it is a less dense oxide. The enhanced selectivity is preferred over the decrease in uniformity. Note that the internal stress in the sacrificial layer is quite large ($\sim$ 300 MPa in compression). A densification step (20 minutes at 800 °C) is thus always performed to decrease the internal stress but it also improves the quality of the oxide hence slowing down the etching rate. However, densification of the oxide is inevitable as subsequent steps (actuator deposition) involve heating to 800 °C. It must be noted that the N_2

[2] SiO_2 grown from a silicon substrate put at high temperature with O_2 gas

flow was found to dramatically impact the etch rate of the densified oxide. A high N_2 flow results in a better uniformity of the deposit while decreasing the etch rate in HF. The recipe used for SiO_2 deposition is thus the best compromise between uniformity and etching selectivity.

It must be pointed out that, in the frame of other researches at UCL, a generic polymer sacrificial layer is under investigation [127].

5.3 Actuator

The second layer to be deposited is the layer that will provide the actuation force: the actuator layer. In order to perform tensile tests, the actuator layer must undergo tensile internal stress. As the actuator dimensions and mechanical properties will be essential in order to extract accurate stress values in specimens, this layer should be as uniform as possible over the entire wafer. Among others, etching selectivity should be as high as possible with respect to the sacrificial layer.

LPCVD (Low Pressure Chemical Vapour Deposition) silicon nitride (Si_3N_4) is used as the actuator layer. It is deposited at 790 °C in a vertical Koyo VF-1000LP furnace. No matter the thickness deposited, the biaxial internal stress is about 1 GPa in tension. The thickness uniformity is very good as it varies by approximately 1 nm over a 3-inches wafer. The internal stress inside the Si_3N_4 layer comes essentially from the difference of thermal expansion coefficient between the silicon nitride ($\alpha_{Si_3N_4} = 6,06\ 10^{-6\circ}C^{-1}$) and the silicon substrate ($\alpha_{Si} = 2,3\ 10^{-6\circ}C^{-1}$). LPCVD Si_3N_4 is an amorphous material transparent to visible light. Its thickness can thus be measured using ellipsometry. It is an elastic isotropic brittle material which means its mechanical behaviour is entirely described by its Young's modulus and its fracture strength.

Si_3N_4 is deposited on both faces of the silicon substrate. No change of curvature should be observed after deposition. Internal stress inside the upper layer can only be determined after etching of the silicon nitride deposited on the back side. This is performed by dry etching with SF_6

plasma. Then, a wafer curvature measurement can be performed to extract internal stress in the Si_3N_4 upper layer.

The patterning of the actuator layer is made by photolithography. A positive photoresist (AZ6612) is deposited on the active face of the wafer (Fig. 5.4b). After prebaking of 90 seconds at 110 °C, the photoresist is exposed to a pattern of UV light using the "actuator mask" (Fig. 5.4c, Section 4.3 for design of the pattern). The exposed positive photoresist is then dissolved in a TMAH (TetraMethylAmmonium Hydroxide)-based solution called "developer"(Fig. 5.4d). A post-exposure bake allows the densification of the remaining photoresist. At this step, the pattern has been transferred from the mask to the photoresist. The next step consists in a pattern transfer from the photoresist to the Si_3N_4 layer. Dry etching is used for that purpose. The SF_6 plasma etches the unprotected part of the Si_3N_4 layer (Fig. 5.4e). The sacrificial layer acts as an etch-stop layer. The remaining photoresist is then removed using acetone or any other solvent that can get rid of the photoresist (Fig. 5.4f). Using UV light for the photolithography process offers a resolution of 0.6 µm meaning that the smallest shape that can be transferred is 0.6 µm large.

LPCVD silicon nitride is the best candidate as an actuator material up to now. Its main advantages are high uniformity of deposition, simple mechanical behaviour, high etching selectivity with silicon oxide in HF. The main drawback comes from the high temperature deposition. Due to this high temperature, the SiO_2 sacrificial layer densifies during the deposition of Si_3N_4. Selectivity is thus decreased. Other options under investigation at UCL, though in the framework of the present study, involve PECVD Si_3N_4 [138] or Cr.

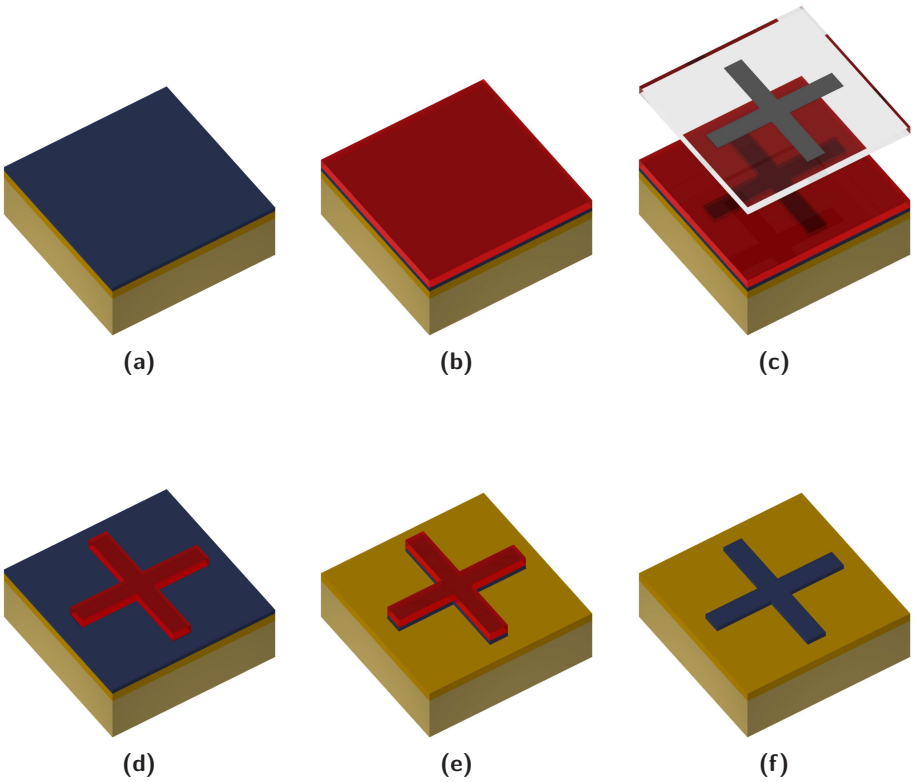

Figure 5.4: *Photolithography steps in the case of positive photoresist: (a) initial configuration with thin film deposited on the substrate, (b) photoresist deposition, (c) mask contact and exposure, (d) dissolution of the exposed photoresist, (e) plasma etching of thin film material, (f) photoresist removal.*

5.4 Specimen

After the patterning of the actuator material, the test material is the last layer to be deposited. No specific property is required for this material as the purpose of the new technique is to test any kind of material. In the present work, the focus is on Al thin films. The last layer to be deposited will always be a pure Al film or an Al alloy film deposited by PVD (Physical Vapour Deposition). The most common PVD methods are evaporation and sputtering.

In evaporative deposition, see Fig. 5.5, thermal energy is supplied to a source from which atoms are evaporated. These atoms then condense on a substrate surface to form a thin film coating. This occurs at low pressure in order to increase the mean free path of the atoms. The evaporated atoms can thus travel through the chamber and condense on the substrate. This method is used to deposit pure metallic materials. Metallic alloys can also be deposited using either a single heated source (alloy source) or two different sources (two pure material sources) at different temperatures. Nevertheless, as the composition in the vapour phase cannot be easily controlled, evaporative methods are generally not used to produce alloy films with specific and uniform composition.

In sputter deposition, see Fig. 5.6, ions, e.g. argon, are accelerated by an imposed electric field toward a target of the metal to be deposited (cathode). As the ions collide with the cathode, secondary electrons are emitted. An electrical discharge is then initiated and sustained. The impact of gaseous ions with the target material causes extraction of the surface atoms which form the vapour in the chamber. These atoms enter and pass through the discharge region to eventually condense on the substrate (anode), leading to the growth of the film. In magnetron sputtering which is usually used in microelectronics, magnets are placed behind the cathode to trap the free electrons in a magnetic field directly above the target surface. This increases their probability of ionising a neutral gas molecule by several orders of magnitude which in turns increases the rate at which target material is eroded and subsequently deposited onto the subtrate.

There are many differences between sputtering and evaporative deposi-

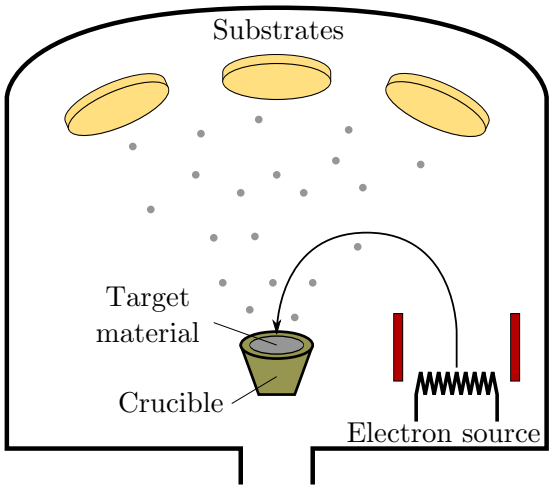

Figure 5.5: *PVD-electron beam evaporation.*

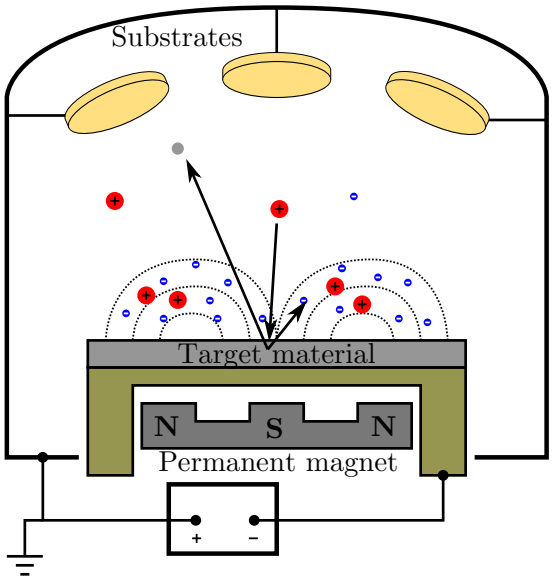

Figure 5.6: *PVD-sputtering.*

tions [98]. In sputtering processes, atoms extracted from the target have a higher kinetic energy than the ones that evaporate from the source in evaporative processes. As a result, sputtered films are more prone to defect nucleation and damage at the deposition surface due to the high energy of atoms. Moreover, as evaporation occurs at very low pressure (1.33×10^{-4} to 1.33×10^{-8} Pa) compared to the high pressure discharge zone (13.33 Pa), sputtered films generally contain a higher concentration of impurities. Conversely, sputter deposition offers better control of the stœchiometry, better step coverage, and better thickness uniformity of the film.

In this work, all the films were deposited by PVD methods. Pure Al films were deposited by evaporation in a modified e-gun Balzers-Vacotec whereas AlSi(1%) films were deposited by sputtering in a S-gun Varian. From the microstructure point of view, only one FCC (Face-Centered Cubic) phase is expected in the pure Al films whereas two phases are expected in the AlSi(1%) film (see phase diagram in Fig. 5.7). The solubility of silicon in Al is indeed almost zero at room temperature and the microstructure is thus expected to be made of Si precipitates in an Al matrix.

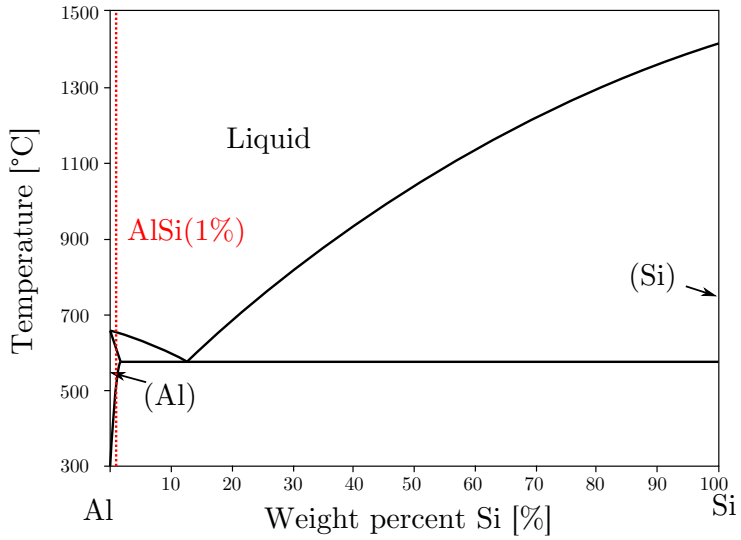

Figure 5.7: *Phase diagram of Al and Si.*

After deposition, the films were patterned by photolithography as for the actuator layer using "specimen mask" (see Section 4.3 for design of the pattern). The first difference with the actuator patterning is that the sample patterning requires a very good alignment between the actuator mask and the sample mask. The second difference is the plasma used for etching of the metallic layer. For both pure Al and Al alloys samples, the etching was performed with a plasma of Cl_2 and CCl_4 in an Electrotech RD600. The photoresist was then dissolved in a HNO_3-based solution.

Note that adapting the technique to another material requires a new recipe for the etching used to pattern the specimen layer. This can be quite complex as the etching selectivity between the specimen material and other layers (photoresist, actuator and sacrificial layer) must be preserved. In order to circumvent such a selectivity study, another method called "lift-off" can be used for the patterning, see Fig. 5.8. The idea is to deposit a negative photoresist (AZ5214) on the wafer before the deposition, see Fig. 5.8b. After pre-baking of 110 seconds at 110 °C, the photoresist is exposed to a pattern of UV light through the specimen mask, see Fig. 5.8c. A post-baking of 40 seconds at 118 °C is then performed followed by another exposure to UV light under an all-transparent mask. The negative photoresist which was masked during the first exposure is then dissolved in the "developer"(Fig. 5.8d). Specimen material deposition is then performed on the whole wafer (Fig. 5.8e) in "lift-off mode" (non-conformal deposition in order to avoid metal deposition on the sides of the photoresist). The lift-off process consists in dissolving the photoresist in acetone or any other solvent. The specimen material located on the photoresist disappears with the acetone solution while specimen material deposited directly on the wafer remains intact, see Fig. 5.8f. This patterning technique simplifies the process but suffers from lower resolution than positive photoresist.

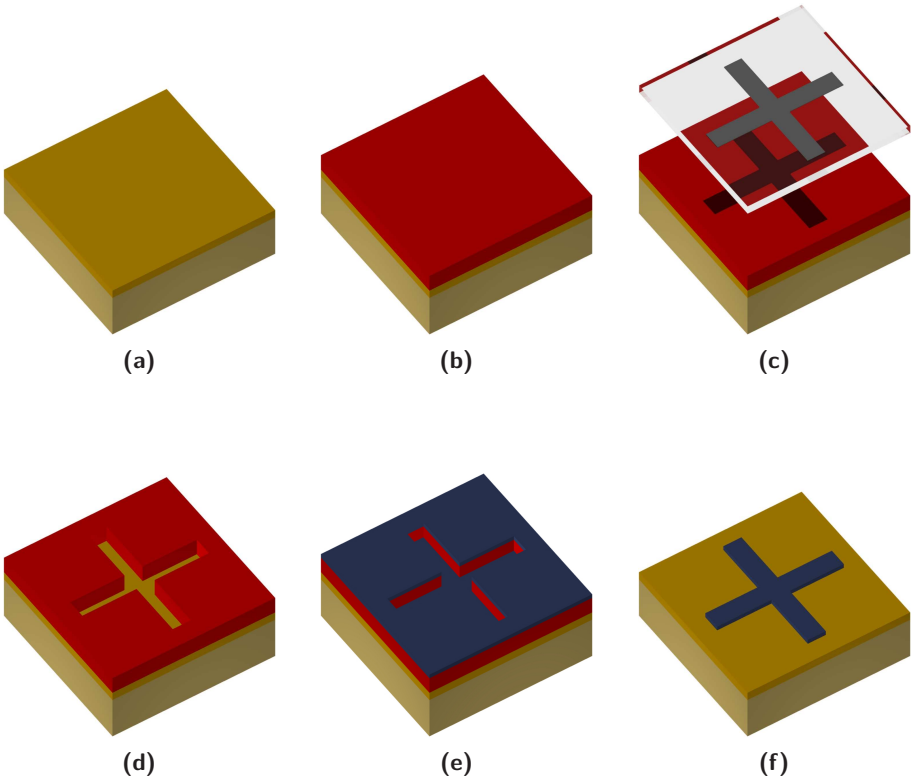

Figure 5.8: *Lift-off process (negative photoresist): (a) initial configuration, (b) photoresist deposition, (c) mask contact and exposure, (d) dissolution of the exposed photoresist, (e) thin film deposition, (f) photoresist removal.*

5.5 Release and etching selectivity

All the previous steps aimed at creating the micromachines. Internal stresses build up in the layers during the deposition steps. In order to load and deform the test material, the sacrificial layer must be etched away. This enables the actuator to contract. As the specimen part is connected to the actuator, the contraction of the actuator leads to an elongation of the specimen. The etching of the sacrificial layer will be referred as the "release step" throughout this work.

The main concern about the release step is a matter of selectivity. The etchant has to etch the sacrificial layer without damaging the other layers, i.e. the actuator and specimen layers. In microfabrication, a sacrificial layer is often associated with a specific etchant solution. For the specific case of silicon oxide, HF (hydrofluroric acid) based solution is commonly used. Dilution of HF in water, iso-propanol or NH_4F is sometimes used in order to monitor the etch rate of SiO_2 and to prevent etching of other materials. Gennissen and French [45] showed that the larger the concentration in HF, the smaller the etching of Al. The highest commercially available HF concentration (73%) was then used in order to etch the sacrificial layer. This solution gives the highest etch rate selectivity between PECVD SiO_2 and Al. Monitoring of the etch rate of SiO_2 layer was performed by choosing the appropriate SiO_2 recipe instead of modifying the etchant. Although the use of vapour HF (pure HF) could even improve the selectivity, it was not tested as it requires an equipment not available within the Winfab facilities.

Etching of the sacrificial layer with HF (73%) belongs to the so called "wet etching" techniques. Another kind of etching which was not used for the Al micromachines involves plasma treatment instead of chemicals. These so-called "dry etching" techniques could be used when trying to adapt the technique to another test material for which a couple sacrificial layer/etchant cannot be found. The idea is to use the top silicon layer on SOI wafer (Silicon On Insulator) as a sacrificial layer (Fig. 5.9). After patterning of the specimen layer (photolithography and etching), an additional step is needed. The micromachines are covered with a protective photoresist (additional mask - Fig. 5.9a and Fig. 5.9b). The

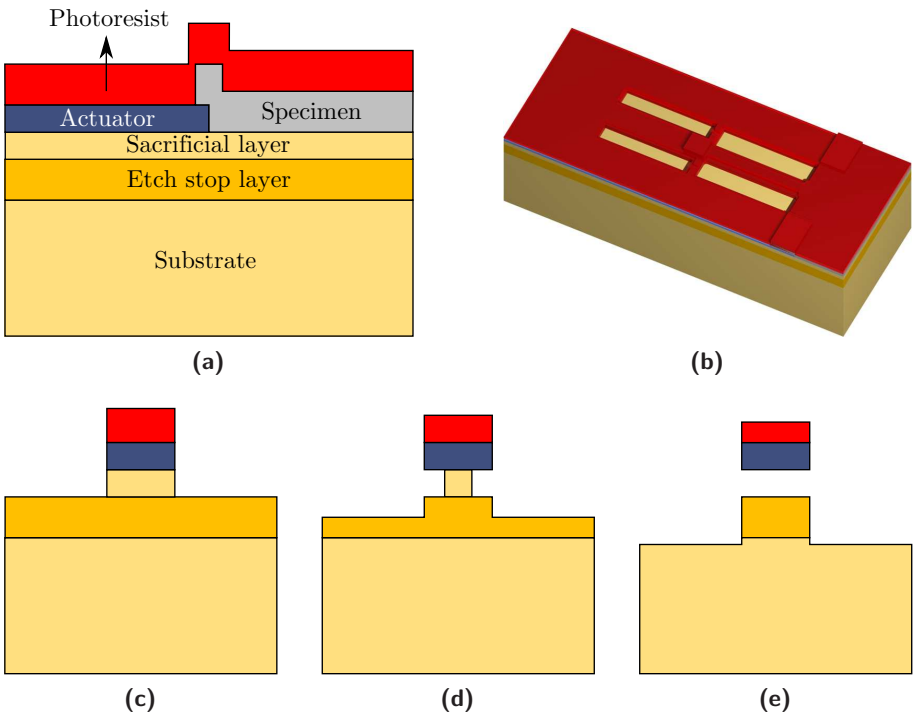

Figure 5.9: *Dry release: (a) and (b) protective photoresist deposition, (c) vertical etch of* Si*, (d) lateral etch of* Si*, (e) etch stop layer fully etched.*

release step is then performed by generating a SF_6 plasma in a chamber. The plasma etches the silicon anisotropically until it reaches the buried oxide which acts as an etch stop layer, see Fig. 5.9c. While the oxide is being etched away by the SF_6 plasma, a faster lateral etching of the silicon is taking place, see Fig. 5.9d. When the oxide has been etched away, the lateral etching of silicon stops and the anisotropical etching of the silicon substrate continues, see Fig. 5.9d. If the buried oxide is thick enough, structures can be released in that way [2]. This technique has been successfully applied in [110] for testing Ti thin films.

5.6 Critical point drying

Whenever wet etching is used to release structures, rinsing is performed in order to stop the etching. Rinsing also ensures that further processing does not damage or contaminate other structures with residual etching solution. Any solvent can be used for rinsing; water, iso-propanol, methanol are of common use. Now, as all measurements on micromachines have to be performed in a SEM environment, involving very low pressure, no liquid can remain on the wafer. Hence, the structures must be carefully dried. Sample drying in air can damage the structures. Indeed, capillary forces would cause the stiction of the structures on the underneath substrate. The solution is to avoid the phase transformation from liquid to vapour by using a critical point dryer (CPD). Basically, a CPD consists in a chamber in which the temperature and the pressure can be controlled. CPD raises the pressure and the temperature of the liquid solution till reaching its critical point where there is no interface between liquid and vapour phases. Pressure in the chamber is then decreased to atmospheric pressure, see Fig. 5.10.

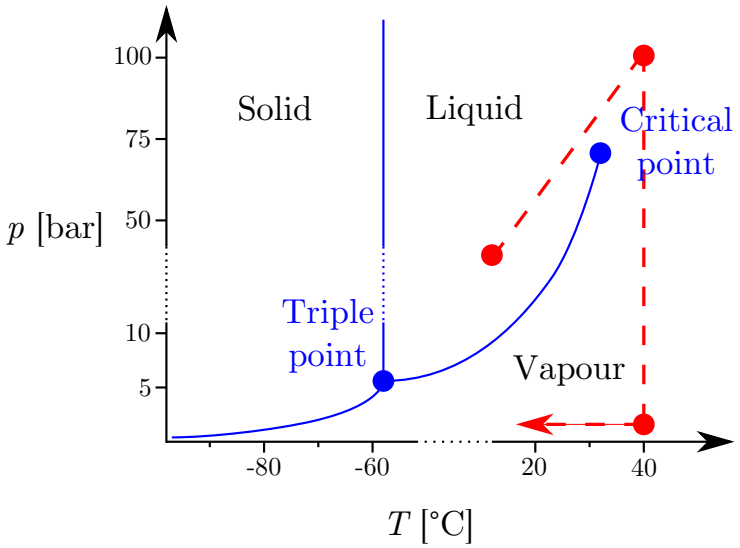

Figure 5.10: *Basic steps in critical point drying.*

Whenever dry etching is used, the only rinsing step is performed through several N_2 purges within the chamber. However, the protective photoresist remains there after SF_6 etching. As the photoresist is much thicker than the test film material, it could influence its mechanical response. Hence, it is preferable to etch the photoresist using a O_2 plasma. In order to avoid oxidation of the test material by the O_2 plasma, the polymer can also be dissolved in acetone. The use of a liquid like acetone will then imply a critical point drying step to avoid stiction.

For the case of Al, after etching in HF (73%), rinsing was performed in isopropanol for 1 minute in a first bath, 5 minutes in a second one and 5 minutes in a third one. Rinsing in water is not used as it would etch the Al. The CPD machine is a Tousimis 915B and uses CO_2 for drying. The critical point of CO_2 (31.3 °C and 7.38 MPa) is indeed easier to reach than the critical point of isopropanol. After the drying, the sample is ready for SEM observation. Note that a whole cycle in the CPD last for about one hour. Adding the rinsing time and transportation to SEM chamber time implies that the first observation can be made only one hour after the release of the sacrificial layer. This has to be taken into account when creep and other relaxation phenomena occur.

Chapter 6

Determination of the geometrical, physical and mechanical parameters for data reduction

This chapter addresses the parameters required to properly extract the mechanical properties of a test material using the on-chip test structures described in Chapter 4 and Chapter 5. These parameters are the ones entering Eq. 4.6 and Eq. 4.7. These two equations are rewritten here (Eq. 6.1 and Eq. 6.2) with the definitions of all the parameters.

$$\varepsilon^{mech} = \ln\left(\frac{L_0 + u}{L_0}\right) - \varepsilon^{mis}. \tag{6.1}$$

$$\sigma = E_a \frac{w_a h_a}{wh}\left(\frac{-u}{L_{a0}} - \varepsilon_a^{mis}\right). \tag{6.2}$$

σ and ε^{mech}	stress and mechanical strain in the specimen beam after release, respectively;
ε^{mis} and ε_a^{mis}	mismatch strain of the specimen and actuator material resulting from the deposition and subsequent fabrication steps;
E_a	Young's modulus of the actuator material;

L_0 and L_{a0}	specimen and actuator beam length at the test temperature before chemical release;
w and w_a	width of the specimen and actuator beam, respectively;
h and h_a	thickness of the specimen and actuator beam, respectively;
u	imposed displacement after release.

In the following, all the procedures used in order to measure these parameters are described in details. Section 6.1 focusses on the measurement of the geometrical parameters (L_0, L_{a0}, w, w_a, h and h_a). Section 6.2 is dedicated to the displacement measurement (u). Section 6.3 shows different types of structures aiming at extracting the mismatch strain in the specimen and in the actuator layer (ε^{mis} and ε_a^{mis}). Section 6.4 describes the method used to determine the actuator Young's modulus (E_a). An additional section (Section 6.5) is dedicated to the measurement of the internal stress in a thin layer on a substrate. Finally, the last section (Section 6.6) summarises the influence of each parameter measurement on the error on the stress and strain.

6.1 Geometrical parameters measurement

As for macromechanical testing, several geometrical parameters have to be determined in order to extract the stress and strain in the specimen. The initial length of the specimen (L_0) is needed in Eq. 6.1. The initial length of the actuator (L_{a0}), thicknesses (h and h_a) and widths (w and w_a) of the specimen and actuator are required in Eq. 6.2. In generation 3 and 4 of micromachines, lengths, widths and thicknesses differ by several orders of magnitude. The techniques to measure these parameters will thus be different.

The actuator lengths generally vary between a few hundreds micrometres and several millimetres and the sample lengths vary between a few micrometres and several hundreds micrometres. These lengths were chosen following the design rules explained in Section 4.3 and are reproduced

on the masks used for the photolithography steps in the fabrication process. The masks were created by e-beam lithography which ensures an accuracy close to one nanometre. When transferring the pattern from the mask to the photoresist, the accuracy is limited by the wavelength of the light used for exposition. Typically, the light source uses UV light (wavelength $\simeq 200\,\text{nm}$). Moreover, under-exposition or over-exposition can occur which alters the final length of structures. So each dimension on the masks is transferred so that these dimensions are increased or decreased by approximately 0 to $1\,\mu\text{m}$.

As a consequence, all lengths involved in the test structures are not measured and are taken as the lengths determined in the design. The error coming from photolithography is indeed very small compared to the length of actuators (usually error less than 0.1%). The error on the specimen length becomes larger in the case of very small specimens but these ones corresponding to highly deformed specimens are often broken and Eq. 4.6 and Eq. 4.7 cannot be used for broken specimens.

The widths of the actuators and of the specimens face the same inaccuracies coming from photolithography but, here, a $1\,\mu\text{m}$ variation constitutes a significant error: the specimen width varies between $1\,\mu\text{m}$ and $12\,\mu\text{m}$ and the actuator width is either $10\,\mu\text{m}$ or $15\,\mu\text{m}$. Moreover, as the etching selectivity is not infinite, both layers are etched during the release step which can also slightly modify the widths. Actuator and sample widths are thus measured by SEM at the highest possible magnification that enables to see the entire width of the beams. For each series of micromachines, the actuator and specimen widths are measured on the less deformed structure (lowest strain). The initial width is then considered to be the same throughout the series, hence taking into account slight changes in width due to non-uniformity of lithography or etching over the wafer. The measurements performed within the SEM can be trusted provided that an appropriate calibration of the measurement has been performed earlier. The accuracy of the measurement is determined by the magnification used to perform the width measurement. Typically, the error on the actuator and specimen width measurement is around 100 nm. Note that in the case of crystalline materials like Al, the width is a mean value as the sides of specimens are

not perfectly flat. This roughness is due to imperfections in photolithography as well as Al grain size which is just one order of magnitude smaller than the width of structures.

The thickness of the layers in the test structures are independent of the design of the masks used for the photolithography. The thickness depends on the deposition conditions (pressure, temperature, position in the chamber, time,etc.). Thickness can vary from wafer to wafer within the same batch and even from location to location over the same wafer.

The thickness of transparent layers such as silicon nitride are measured by ellipsometry. Ellipsometry measures the polarisation change upon reflection. This change is determined based on the layer properties, including the thickness. The actuator layer thickness can thus be measured with an accuracy around one nanometre[1]. Ellipsometry does not need patterning of the layer before the measurement. However, in order to account for possible thickness variation over the wafer and because the thickness can vary due to etching, ellipsometry measurements should be performed after the release step. The only requirement in the design is to have zones large enough to allow the measurement. The beams in the micromachines are indeed too small in the width to be measured by ellipsometry. Hence, large squares (1 mm x 1 mm) have thus been designed all over the wafer. It must also be noted that post-release measurement over large squares does not account for possible etching below structures. Now, assuming etching rate are constant with time, the final section of actuator beams can be calculated easily as described in Fig. 6.1.

For the case of non-transparent layers, profilometry is used instead of ellipsometry. A sharp tip is moved vertically in contact with a sample and then moved laterally across the sample for a specified distance and specified contact force. A profilometre can measure vertical displacement with nanometre resolution as a function of position[2]. As a consequence, profilometry does not directly measure the thickness of a layer but can only measure steps. The thickness has thus to be measured after patterning the layer. Again, due to the non-uniformity of the deposition and

[1]The ellipsometer used in this work was a Sentech 850.
[2]The profilometre used in this work was a Veeco Dekatk 150.

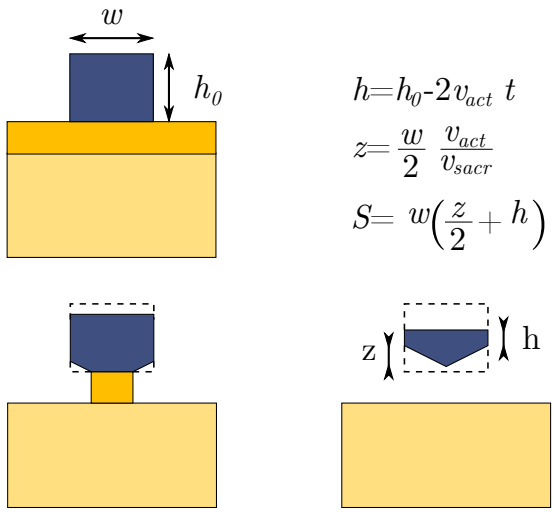

Figure 6.1: *Method used to determine underetching of actuators: h_0 is the initial thickness of the films, w is the width of the beam, h and z are shown in the figure, t is the time spent in the etchant, v_{act} and v_{sacr} are the etching rates of the actuator and sacrificial layer material, respectively, and S is the final section of the actuator beam.*

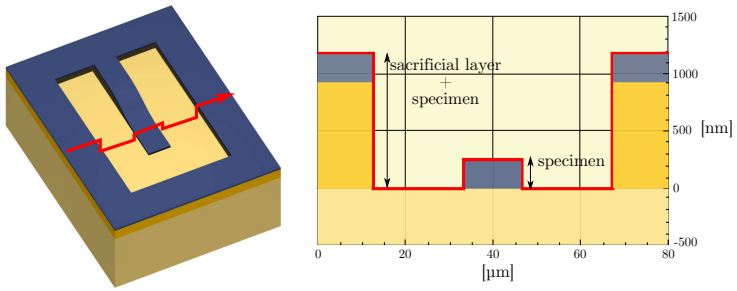

Figure 6.2: *Method used to determine the final thickness (h) of the specimen beam by profilometry.*

etching of the layer, profilometry should be used after the release step. Large unreleased squares (1 mm x 1 mm) are located all over the wafer in order to properly measure the specimen thickness. In this case, using the bulk silicon of the wafer as a reference, the measured step is the combination of the thickness of the sacrificial layer and of the thickness of the specimen layer. The specimen thickness is obtained by subtracting the sacrificial layer thickness which is measured by ellipsometry. The profilometre can also measure the thickness of any patterned layer by running the tip on cantilever beams, see Fig. 6.2. When the tip meets a cantilever, it forces contact and stiction between the beam and the bulk silicon which enables a thickness measurement. In this work, the specimen layer being made of pure Al or AlSi, profilometry is used to measure the specimen thickness and the accuracy is considered to be around 5 nm.

6.2 Displacement measurement

The displacement (u) resulting from the partial release of the internal stresses in the actuator beam has to be measured to determine the stress and strain in the specimen. The smallest displacement is around a few tens of nanometres (for short structures and small strain in the specimen) whereas the largest displacement occurs for the longest free actuators (broken specimen and no more stress inside the actuator beam) and

is around 6 µm. Optical microscopy does not provide enough accuracy to measure these displacements. Scanning electron microscopy (SEM) is used instead. The main disadvantage of SEM comes from charging effects. Indeed, the electrons from the beam can be evacuated only if the exposed area is a metal which is connected to the ground[3]. For insulating materials such as silicon nitride used for actuation, the charges accumulate and are responsible for local distortion of the electron beam, especially in the case of out of plane beams. FEG-SEM (Field Emission Gun) is thus used as it allows working at small voltage (1 kV).

Nanometre resolution can be reached by SEM provided that proper calibration has been performed. The resolution is strongly dependent on the magnification used to do the measurement and on the quality of the SEM. For each micromachine, the displacement measurement is performed next to the overlap between the actuator and specimen. Pairs of cursors have been designed on each side of the actuators. These cursors are 3 µm by 2 µm. The reference cursors are connected to the anchor[4]. The moving cursors are connected to the actuator beam and are aligned with the reference cursors prior to the release step. The contraction of the actuator beam leads to the displacement between the moving cursors and the reference cursors, see Fig. 6.3. The displacement being on the order of a few micrometres, the highest magnification which still shows the two types of cursors is around 20,000. The measurement is performed directly on the SEM picture and on both sides of the actuator. The displacement is taken as the mean value of four measurements (u_1 to u_4) as shown on Fig. 6.3. This enables to take into account possible misalignment between actuator and specimen masks. The accuracy on the measurement of the displacement is about 50 nm. This accuracy results more from the limited resolution of photolithography than from the resolution of the SEM. Indeed, cursors are not perfectly rectangular as designed on the masks which makes it difficult to choose the right pixel line for the measurement.

[3]In generation 4, all specimen parts (metals in this work) have been connected together. It is then easy to create a bridge between any part of the specimen layer and the ground (using silver paint).

[4]The anchors are the zones which are too large to be released from the substrate

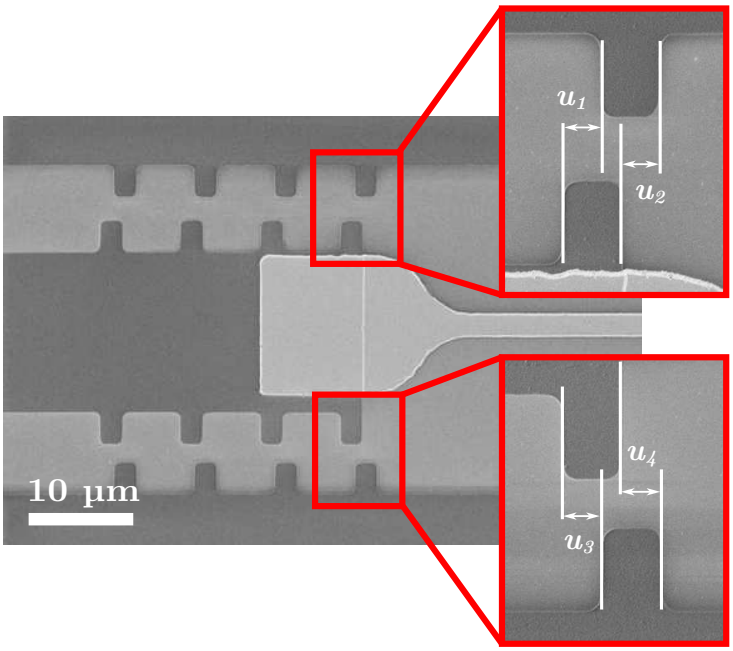

Figure 6.3: *SEM measurements to determine the displacement u.*

6.3 Mismatch strain measurement

As explained in Section 4.2, the mismatch strain is the strain present in a material after deposition on the substrate. Each material has its own mismatch strain which depends on the material properties as well as on the deposition conditions. Two mismatch strains are needed in Eq. 6.1 and Eq. 6.2.ε^{mis} affects the stress in the test specimen, see Eq. 6.2 and ε_a^{mis} affects the strain in the test specimen, see Eq. 4.6. Three types of structures were designed on the actuator and specimen masks in order to determine these two mismatch strains: rotating sensors, free cantilever beams and auto-actuated micromachines. It must be noted that He et al. [63] proposed a comparison of different techniques to extract mismatch strain in thin layers. Rotating sensors are one of them, but the two others are the most recent ones and first used in [7].

6.3.1 Rotating sensors

Following the design described in [66], rotating sensors were introduced at different locations over the set of masks of generation 3. The device consists of two fixed beams and one rotating indicator beam (see Fig. 6.4). Each fixed beam is connected to the substrate at one end and to the indicator beam at the other end. When the fixed beams are released from the substrate, they contract, see Fig. 6.4a, or extend, see Fig. 6.4b, in order to relieve the tensile or compressive internal stress. As the two fixed beams are slightly separated at the connection with the indicator beam, any deviation along the length of the fixed beams introduces a torque on the centre of the device causing the indicator beam to rotate. The direction indicates the type of stress (tensile or compressive) whereas the amplitude is proportional to the mismatch strain of the constitutive material of the device.

He et al. [63] provide the following equation in order to extract the mismatch strain from rotating sensors,

---

during the etching of the sacrificial layer.

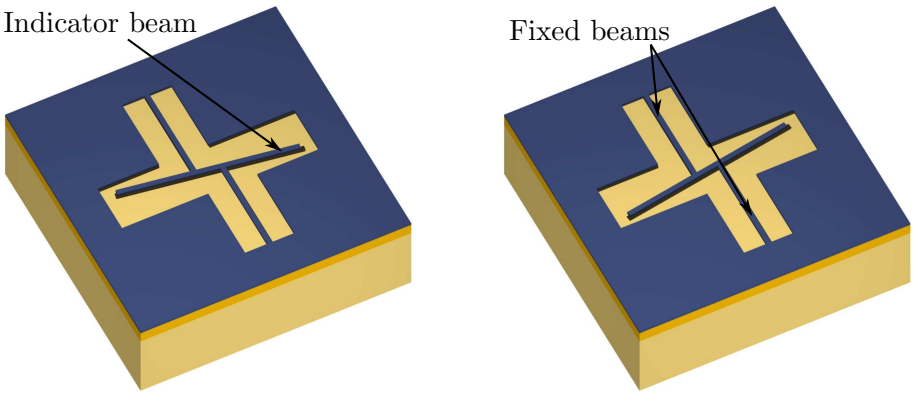

Figure 6.4: *Rotating sensor design (a) tensile internal stress and (b) compressive internal stress.*

$$\varepsilon_{mis} = \frac{D}{2L_{fixed}\left(L_{ind} + \frac{1}{2}D\right)}\delta, \tag{6.3}$$

ε_{mis}	mismatch strain of the material of the rotating sensor;
D	distance between the two fixed beams;
L_{fixed}	length of the two fixed beams;
L_{ind}	length of the indicator beam;
δ	displacement at the tip of the indicator beam.

More accurate values can be extracted from finite element simulations [66]. These structures were not used to determine the magnitude of the mismatch strain in each layer. Indeed, inaccuracies in the photolithographic process, especially where indicator beam and fixed beams are connected, can affect the rotation of the indicator beam [27] [66]. Moreover, these structures become inaccurate for too large deflection, i.e. large mismatch strain, or when plasticity occurs in the portion of the indicator beam between the two fixed beams [66]. As the optimisation of the design for a specific material as well as finite element simulations

of the structure were needed, rotating sensors were not used to quantify the mismatch strain of the actuator and of the test specimen material in the context of the present work. Nevertheless, these devices were still used to check the type of internal stress, i.e. tensile or compressive, and to confirm the absence of internal stress in some layers (no deflection for all structures) as in the case of pure Al in Section 9.2.

6.3.2 Free cantilever

When a thin film material is deposited, internal stress often develops. The internal stress is not relaxed by the patterning if the dimensions are much larger than the thickness and is relaxed in a very small region along the boundaries of the wafer with a width on the order of the film thickness. If the pattern is a beam connected to an anchor on one side, the beam experiences a strain such that it is longer (resp. shorter) than the undeformed beam in case of tensile (resp. compressive) stress. Releasing the internal stress in the thin film material by etching the sacrificial layer relaxes the beam to the unstressed position (Fig. 6.5). By the comparison of the length of the beam before (strained beam) and after (free beam) release provides the mismatch strain of the thin film material. Note that the mismatch strain is the elastic strain corresponding to the internal stress. It does not involve possible plastic strains developing when the internal stress is larger than the yield strain. This idea was already explained in Section 4.2. The mismatch strain for a cantilever beam of length L_0 is given by

$$\varepsilon_{mis} = \ln\left(\frac{L_0 - u_{free}}{L_0}\right), \tag{6.4}$$

ε_{mis} mismatch strain of constitutive material of cantilever beam;

L_0 initial length (before release) of cantilever beam;

u_{free} displacement of the free end of the cantilever beam after release [5].

[5] Let us remind that u_{free} is considered to be positive if the thin film material experiences tensile internal stress.

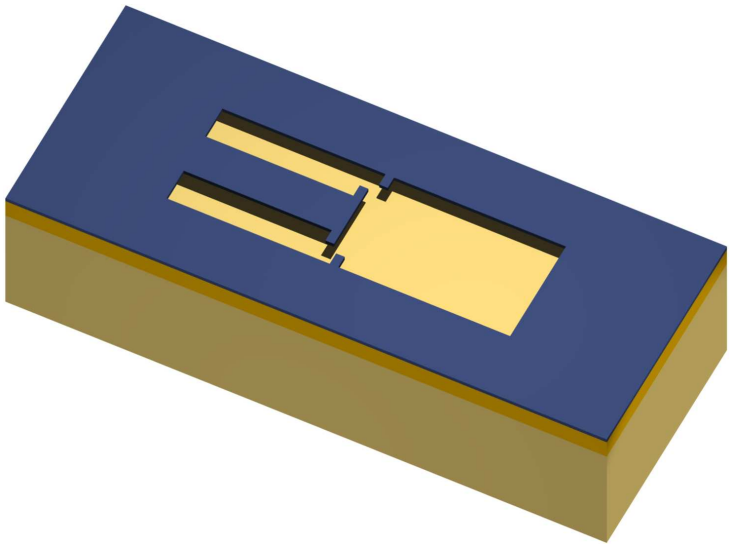

Figure 6.5: *Free cantilever beam which has experienced tensile internal stress before etching of the underlying sacrificial layer.*

Theoretically, the mismatch strain extracted from equation (6.4) should be the most accurate method provided that u_{free} can be measured accurately. Indeed, no assumption is made in the determination of Eq. 6.4. Only two parameters are needed. The length L_0 is accurately known, see Section 6.1, and the accuracy on displacement measurement can be very good, see Section 6.2. Moreover as the error decreases with larger values of both parameters, longer free cantilevers give better accuracy on the mismatch strain measurement.

Now, in the practice, long free cantilevers cannot surely be used for such measurements as minor internal stress gradients over the thickness give rise to out of plane bending (Fig. 6.6). As out of plane displacement cannot be measured (at least not accurately), only short cantilever showing no out of plane bending can be used. The accuracy on u_{free} is thus usually too low for accurate determination of the mismatch strain.

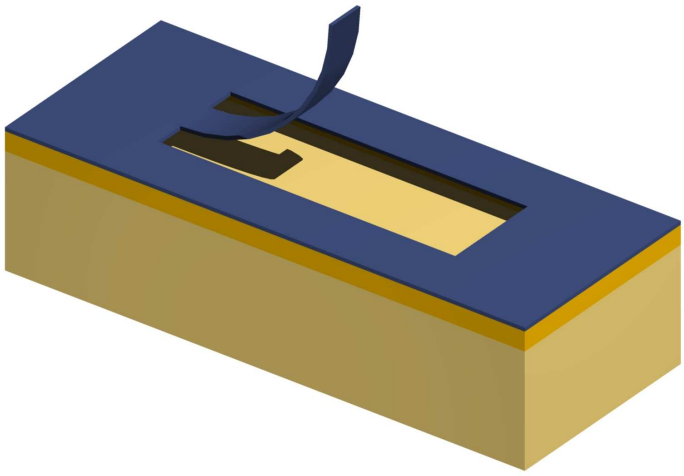

Figure 6.6: *Out of plane bending of free cantilevers.*

6.3.3 Single material auto-actuated test structures

In order to circumvent the problem caused by out of plane bending occurring in free cantilevers, structures clamped on both sides were designed. The concept is similar to the self actuated tensile stage concept, see Fig. 4.1, but using a one-mask process. The double clamped beam still involves two parts called actuator beam and specimen beam but the material is the same for both beams, see Fig. 6.7. The actuator beam is wider than the specimen beam. If the thin layer experiences a tensile internal stress, the wider beam will contract and pull on the specimen beam. Under the condition that all the parts of the structure stay in the elastic regime, the structure reaches a stable equilibrium governed by equation (6.5):

$$\begin{aligned} F &= S_a E \left(\frac{-u}{L_{a0}} - \varepsilon^{mis} \right) \\ &= SE \left(\ln \left(\frac{L_0 + u}{L_0} \right) - \varepsilon^{mis} \right), \end{aligned} \tag{6.5}$$

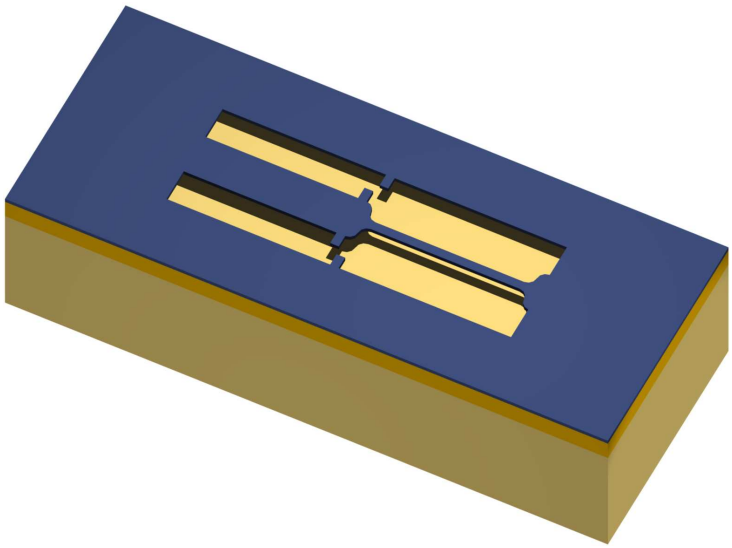

Figure 6.7: *Auto-actuated structure.*

F	force experienced by both beams when equilibrium is reached;
ε^{mis}	mismatch strain in the thin film material;
E	Young's modulus of the thin film material;
L_{a0} and L_0	length of actuator beam and specimen beam before chemical release, respectively;
u	displacement between current (before release) and initial (after release) position;
S_a and S	final section of the actuator beam and of the specimen beam, respectively.

Eq. 6.5 is similar to Eq. 4.5 but differently written. Here, the first equality is from the actuator beam point of view whereas the second equality is from the specimen beam point of view. Together, these two equalities provide a relationship independent of E, linking the mismatch strain ε^{mis} to the geometrical parameters as,

$$\varepsilon_{mis} = \frac{S \ln\left(\frac{L_0+u}{L_0}\right) - S_a \frac{-u}{L_{a0}}}{S - S_a}, \tag{6.6}$$

As all these geometrical parameters can be measured (see section 6.1), the auto-actuated micromachine can be used in two different ways:

- Multiple structures can be designed with varying dimensions in order to optimise the parameters that will give the most accurate value for mismatch strain and in order to generate statistical data.
- Assuming that both the mismatch strain and the Young's modulus of the material are known, these structures can be used to extract the mechanical properties of the thin film material by using equations (6.1) and (6.2).

It must be noted that extracting the stress in the specimen beam using auto-actuated structures is possible only if the Young's modulus of the material is known. Indeed, Eq. 6.2 needs the Young's modulus of the actuator material which is the same as the specimen material here. The Young's modulus should be determined by another technique such as nanoindentation (see Section 6.4). In Fig. 6.8a, the stress-strain curve of a 130 nm-thick Si_3N_4 film is extracted from a set of auto-actuated structures. This curve was obtained assuming that the Young's modulus of Si_3N_4 was 240 GPa and that the mismatch strain was equal to -0.0032 (extracted from a free cantilever). The error bars in Fig. 6.8a account for the error coming from the displacement measurement only. The error on the strain becomes important for the smallest specimens which experience the largest strain. Indeed, for these specimens the length of the dogbone part becomes non negligible compared to the length of the specimen and finite element analysis should be performed to determine the strain in the uniaxially deformed zone. As a consequence, the non-linearity of the curve in Fig. 6.8a for the largest strain comes rather from a poor design than from a true material characteristic (non-linear elasticity or plasticity).

Even if the Young's modulus is not very well known, the stress-strain curves obtained with auto-actuated structures are still useful in order

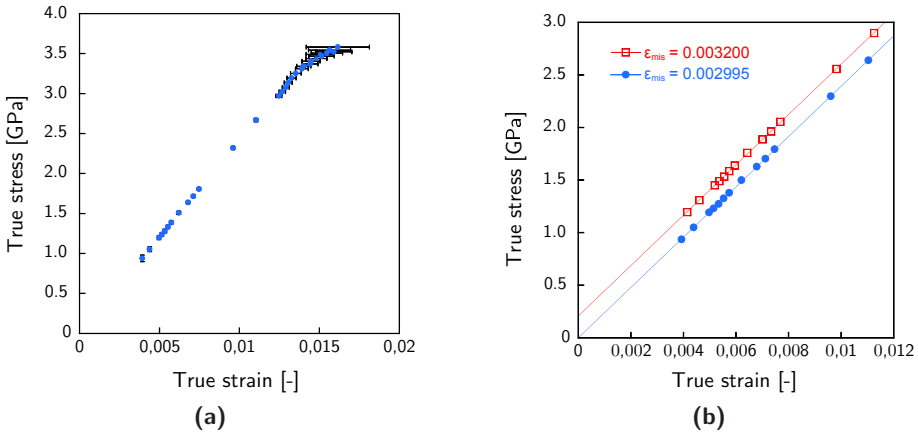

Figure 6.8: *Data obtained from a* 130 nm*-thick* Si_3N_4 *film: (a) true stress - true strain curve obtained with* $E = 240$ GPa *and* $\varepsilon^{mis} = -0.0032$ *(b) calibration of the mismatch strain by imposing the stress-strain curve to meet the origin of the axis.*

to determine the mismatch strain. The slope of the elastic part of the stress-strain curve cannot be calculated accurately as it depends on the value selected for the Young's modulus. However, what is known for sure is that the elastic line should meet the origin of the axis. The mismatch strain can thus be calibrated in order to meet this condition. This is performed in Fig. 6.8b where the upper line corresponds to a mismatch of -0.0032 as what was used in Fig. 6.8a. Calibration of the mismatch strain in order to meet the origin of both axis gives a mismatch strain equal to -0.002995.

The developments concerning auto-actuated structures were essentially conducted in order to determine the mismatch strain of the actuator material (silicon nitride here). Note that these structures cannot be used for compressive internal stress leading to the buckling of the beams.

6.4 Young's modulus measurement

Proper extraction of the stress in a specimen beam of an on-chip test structure requires the Young's modulus E_a of the actuator material as stated by Eq. 6.2. In [7], a method is proposed to extract the Young's modulus of a layer (E_f) from the measurement of both the elastic strain in the layer (ε_f^{el}) which is equal and opposite to the mismatch strain, and of the residual stress (σ_f) in the layer. These three parameters are linked through Eq. 6.7:

$$E_f = \frac{\sigma_f \, (1 - \nu_f)}{\varepsilon_f^{el}}, \tag{6.7}$$

where ν_f is the Poisson ratio of the film.

In [7], this method has been used on silicon nitride films similar to the films used in this work. The internal stress is extracted using the wafer curvature measurement method described in Section 6.5. The elastic strain is extracted by the same methods as the ones detailed in Section 6.3. The accuracy of the method is very much dependent on the accuracy of the metrology used for the displacement measurements involved in curvature measurement (for σ_f) and displacement measurement (for ε_f^{el}).

A more conventional method to extract the Young's modulus of a thin film layer is to perform depth sensing nanoindentation as described in Section 2.1.1. In [7], nanoindentation of the films is performed using an add-on force transducer from Hysitron Inc. with a Berkovich tip mounted on a conventional Atomic Force Miscroscope (AFM). Oliver and Pharr method [99] is used and gives a Young's modulus equal to 241 GPa.

Now, as already stated in Section 2.1.1, the extracted Young's modulus can be very dependent on the indentation depth:

- In the case of too small indentation depth, the small indented volume can result in too low accuracy. Moreover the roughness might have an impact on extracted data.

- In the case of too deep indentation, the nanoindenter tip may "feel" the presence of the substrate.

No quantitative rule can be stated as the "too small" limitation depends on the roughness of the film and the "too deep" limitation depends on the stiffness mismatch between the substrate and the film.

To have more insights in the best indentation depth that can be used to extract the Young's modulus of a particular film, use can be made of the Continuous Stiffness Measurement (CSM) [1]. This mode was developed by Agilent Technologies and has been available on a new nanoindenter set-up[6] operational in our lab since the beginning of the year 2011. The CSM mode consists in applying a load to the indenter tip to force the tip into the surface while simultaneously superimposing an oscillating force with a force amplitude generally several orders of magnitude smaller than the nominal load (extracted from [1]).

The CSM mode has been successfully used for indentation of a 440 nm-thick Si_3N_4 film. The output is a graph showing the evolution of the Young's modulus as a function of the indentation depth in the film as shown in Fig. 6.9. The uncorrected modulus is the Young's modulus extracted by Oliver and Pharr method while the corrected modulus is the "real" Young's modulus of the film obtained by a model which takes into account the presence of the substrate [61].

On the apparent modulus in Fig. 6.9, it is clearly seen that very small indentation depth ($\sim 2\%$) cannot capture a defined value of the Young's modulus essentially due to surface effects. As the indenter penetration increases, the apparent modulus is increasingly influenced by the presence of the softer substrate (Young's modulus of silicon = 180 GPa). There is no range of the indentation depth for which apparent modulus is independent of the substrate or in other words, no plateau is reached. On the contrary, the corrected modulus enables to reach a plateau between 10% and 40% of the normalised indentation depth. This plateau value can thus be considered as the real Young's modulus of the thin film material.

[6]The nanoindenter is a G200 Agilent Techologies.

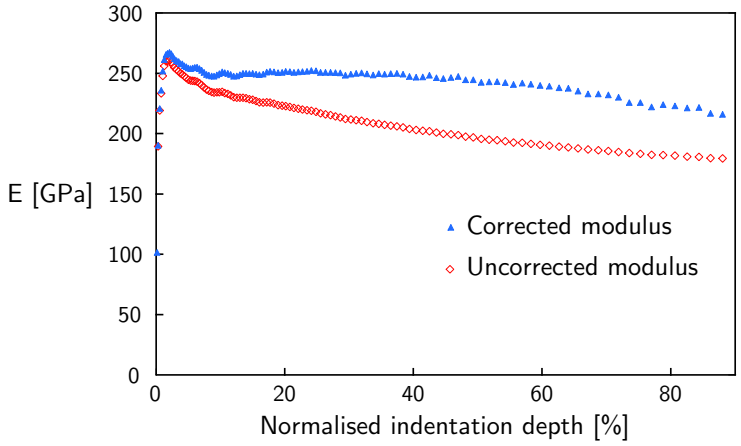

Figure 6.9: *Young's modulus as a function of the normalised indentation depth in a* 440 nm*-thick* Si_3N_4 *film.*

6.5 Internal stress measurement

When a material is deposited on a substrate, internal stresses often develop. These residual stresses can be divided into two broad categories:

- Intrinsic stresses are the stresses arising from growth on the substrate. These stresses are strongly dependent on the deposition conditions and are usually due to the fact that the deposition occurs under non-equilibrium conditions;
- Extrinsic stresses arise from the changes in the physical environment of the film material after the growth process. They include the thermal contribution which arises as a consequence of the difference in thermal expansion coefficient between the film and the substrate.

Many mechanisms for stress generation in thin film deposition on thick substrate have been proposed, e.g. [26] for a detailed review. Generally, stresses result from a combination of these mechanisms. No matter the mechanisms involved, a thin stressed layer on top of thick substrate will

induce a change of curvature of the substrate. The solution for a bilayer under equibiaxial condition is analytic as long as the layers remain elastic and the in plane dimensions are much larger than the thickness. When the stiffness of the film is much smaller than the stiffness of the substrate, the solution can be expressed in the following way known as Stoney's formula [118]:

$$\sigma = \frac{1}{6}\frac{E_s}{1-\nu_s}\frac{t_s^2}{t_f}\left(\frac{1}{R_{post}} - \frac{1}{R_{pre}}\right), \tag{6.8}$$

σ	stress in the film;
$\frac{E_s}{1-\nu_s}$	biaxial modulus of the substrate material;
t_s	thickness of the substrate;
t_f	thickness of the film;
$\frac{1}{R_{pre}}$	initial curvature of the substrate;
$\frac{1}{R_{post}}$	final curvature of the substrate.

The film properties film do not enter Eq. 6.8 which remains valid if the film does not deform in a linear elastic way.

Although the internal stress is not a parameter entering Eq. 6.1 and Eq. 6.2, wafer curvature measurement using Eq. 6.8 is performed in order to monitor the deposition steps. Stoney equation can be used in this work as the substrates are very stiff, i.e. 380 µm-thick with a high Young's modulus, compared to all the layers under investigation with thickness below 1 µm. The biaxial modulus of silicon is equal to 180 GPa [65]. The thickness of the substrate is considered to be uniform: specifications of the silicon wafers claim for a Total Thickness Variance (TTV) of 5 µm. One thickness measurement is performed for each wafer with a palmer. The accuracy of the device ($\simeq$ 10 µm) is lower than the TTV. The thickness of the film is measured either by ellipsometry or profilometry depending on the material deposited, see Section 6.1 for details. Again, the film thickness is assumed to be uniform over the wafer. Finally, the initial and final curvature are measured with a profilometre (Fig. 6.10). The tip is run in the middle of the wafer from

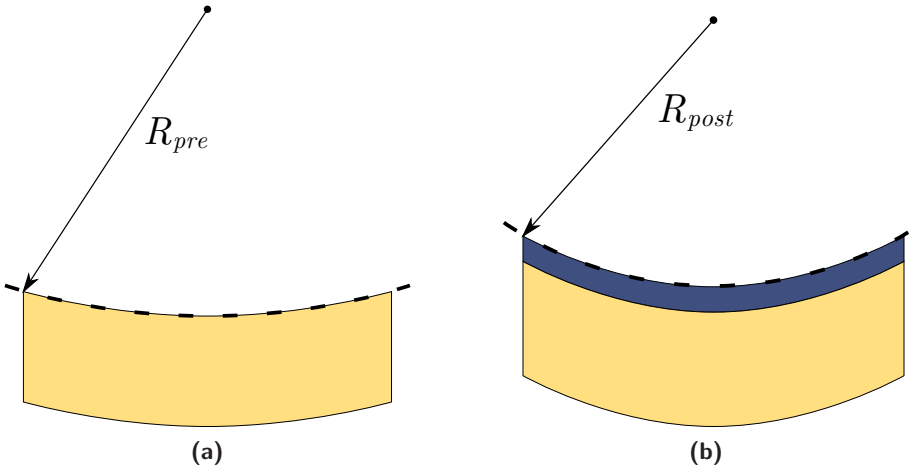

Figure 6.10: *Wafer curvature measurement (a) before and (b) after deposition.*

the flat part to the other end as already sketched in Fig. 5.3a. The radius of the measured profile is calculated using a least squares fit. Convex and concave profiles give positive and negative radius, respectively.

In the case of multiple depositions, Eq. 6.8 can still be used as long as the curvature just before the new deposit is taken as the initial curvature. The stresses in each layer can thus be calculated using the Stoney equation. However, care must be taken as the change in curvature can result from other contributions than the stresses generated in the last deposited layer. Indeed, stress relaxation in the other layers can contribute to the overall change in curvature. This is what happens when depositing LPCVD Si_3N_4 on PECVD SiO_2. As the actuator layer deposition is performed at high temperature (790°C), the stress in the SiO_2 layer can relax. Typically the stress decreases from 300 MPa in compression to less than 100 MPa in compression. In order to properly measure the change of curvature coming from the Si_3N_4 deposition, stresses in SiO_2 have to be relaxed first. The wafer with the SiO_2 layer is thus subjected to a 20 minutes heat treatment at 800 °C. The initial curvature in Eq. 6.8 is then measured after the densification step so that the internal

stress in the sacrificial layer no longer evolves in the subsequent process steps.

6.6 Error analysis

The uncertainties on all the parameters has some implications on the level of accuracy of the extracted strain and stress in the specimen beam. From the propagation of uncertainties described in the book of John R. Taylor [119], the relative error on strain and stress is calculated in Eq. 6.9 and Eq. 6.10, respectively.

$$\frac{\delta\varepsilon^{mech}}{\varepsilon^{mech}} = \sqrt{\left(\frac{\delta u}{L_0+u}\right)^2 + \left(\frac{-u\delta L_0}{L_0(L_0+u)}\right)^2 + (\delta\varepsilon^{mis})^2}, \tag{6.9}$$

$$\frac{\delta\sigma}{\sigma} = \left(\left(\frac{\delta E_a}{E_a}\right)^2 + \left(\frac{\delta w_a}{w_a}\right)^2 + \left(\frac{\delta w}{w}\right)^2 + \left(\frac{\delta h_a}{h_a}\right)^2 + \left(\frac{\delta h}{h}\right)^2 + \left(\frac{\sqrt{(\delta\varepsilon_a^{mis})^2 + \left(\frac{u}{L_{a0}\sqrt{\left(\frac{\delta u}{u}\right)^2+\left(\frac{\delta L_{a0}}{L_{a0}}\right)^2}}\right)^2}}{\varepsilon_a^{mis} - \frac{u}{L_{a0}}}\right)^2\right)^{1/2} \tag{6.10}$$

The values of the uncertainties on the different parameters are summarised in Table 6.1. The resulting errors on the strain and stress depend on the parameters of the micromachine considered. As a result the error varies from one test structure to the other. Generally speaking, the error on the strain is relatively small in the lab on-chip concept as the uncertainty on the displacement 50 nm is usually a lot smaller than the displacement measured (a few micrometres). The mismatch strain

Parameter	Measurement method	Uncertainty
Displacement (u)	SEM	$\delta u = 50\,\text{nm}$
Actuator Young's modulus (E_a)	Nanoindentation	$\delta E_a = 10$ GPa
Mismatch strain of specimen and actuator material (ε_a^{mis} and ε^{mis})	Free cantilevers or single material auto-actuated test structures	$\delta\varepsilon_a^{mis} = \delta\varepsilon^{mis} = 1.10^{-4}$
Length of specimen beam (L_0)	Not measured	$\delta L_0 = 1\,\mu\text{m}$
Length of actuator beam (L_{a0})	Not measured	$\delta L_{a0} = 1\,\mu\text{m}$
Width of specimen and actuator beam (w and w_a)	SEM	$\delta w = \delta w_a = 100\,\text{nm}$
Thickness of specimen beam (h)	Profilometry	$\delta h = 5\,\text{nm}$
Thickness of actuator beam (h_a)	Ellipsometry	$\delta h_a = 1\,\text{nm}$

Table 6.1: *Summary of the uncertainties on the parameters required for extraction of stress and strain in the specimen beam.*

being the same for each specimen beam, the uncertainty on the mismatch strain of the specimen material introduces a systematic error on the strain measurement. Concerning the stress determination, the dominant sources of errors are the actuator Young's modulus, the actuator mismatch strain and the displacement measurement. The two first being related to the actuator material properties, these are systematic errors as the actuator layer is supposed to have uniform properties over the wafer.

Chapter 7

Extensions of the method

This chapter presents additional features of the concept of self actuated micro-tensile stage. These features concern the geometry of the specimens (Section 7.1) as well as the process fabrication steps (Section 7.2), with the aim to generate more insight in the mechanical behaviour of thin film materials.

7.1 Notched samples

In chapters 4, 5 and 6, the focus was put on rectangular actuator beams pulling on dogbone shaped specimen beams. This simple geometry generates uniform tensile tests where the behaviour of the specimen material can be investigated from small elastic strain to large plastic strain. This is true as long as the strain state inside the gauge section of the dogbone specimen stays uniform. But under tensile loading conditions, plastic localisation by necking or shear banding can occur. In this case, the strain is no more uniform along the specimen. Strain increases in the localised region while the remaining of the specimen unloads elastically. The cursors at the actuator tip give only a global displacement measurement but cannot tell any information about the localised portion of the specimen beam. After initialisation of any localisation phenomena, the specimen can sometimes undergo significant straining before complete failure of

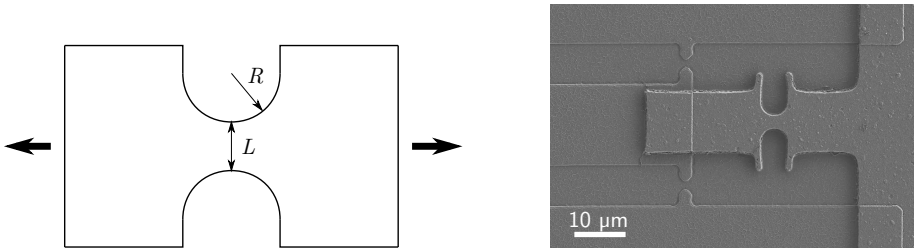

Figure 7.1: *Design of a notch specimen.*

the material. Standard dogbone design is thus not suitable to investigate the behaviour of a material after localisation.

In order to study the deformation behaviour until full fracture without the artefacts resulting from the necking process, series of notched specimens have been designed. The specimen shape is depicted in Fig. 7.1 and different values for ligament (L) and notch radius (R) are envisaged. Within one series the specimen shape is kept constant and the actuator length is varied.

The strain field in the notched specimen is no more uniform, which prevents the occurrence of necking. Cursors are still designed at the actuator tip and give information about the global force applied to the specimen similarly to standard specimens. But due to the non-homogeneity of the strain field within the notched specimen, measurement of displacement u is not sufficient to determine the strain. As no simple analytical method is available to extract the strain field in the specimen, 3-D finite element (FE) simulations are needed. For that purpose, Abaqus software is used. The two required inputs are a mesh of the specimen and a hardening law. The mesh needs to be highly refined in the near notch tip region where the largest strains develop. The hardening law can be extracted from uniform tensile testing via dogbone specimens.

Owing to the simple concept of actuating beams pulling on specimens, any geometry can be imagined in order to create specific loading conditions. Generation 2 set of masks aimed at testing many different designs.

They include shear structures Fig. 7.2a, compression structures, biaxial tensile structures Fig. 7.2b. Structures aiming at testing the material resistance to damage were included by creating holes Fig. 7.2c or pre-crack in specimens directly in the photolithography process. These structures have not yet been optimised and further generations were dedicated to tensile testing via standard dogbone geometry or notched specimens.

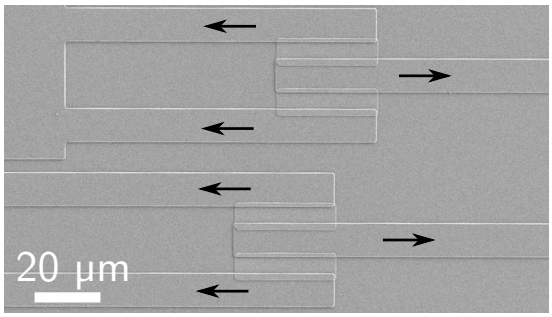

(a)

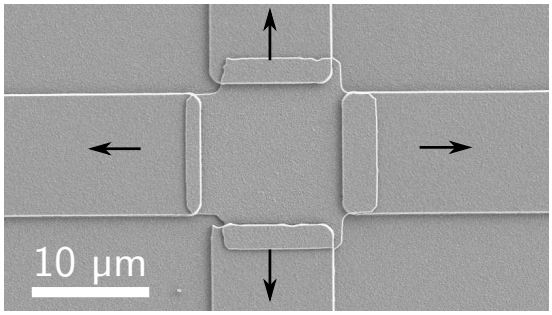

(b)

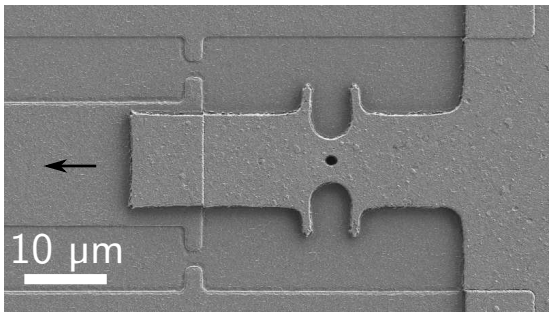

(c)

Figure 7.2: *Geometries created for various types of solicitations including (a) shear structures, (b) biaxial tensile structures as well as (c) structures with holes or pre-crack.*

7.2 Back etching for TEM observation

One of the advantages of dealing with thin films materials is that the use of Transmission Electron Microscopy (TEM) requires almost no further sample preparation for in-plane characterisation. Indeed, TEM specimens are required to be at most 100 to 200 nm-thick (HRTEM requires thinner specimen though). Higher atomic number elements being more prone to electron interaction, the thickness has to be decreased for heavier elements. In the case of Al samples, the maximum thickness is around 200 nm. TEM is a powerful tool as it allows the characterisation of the microstructure of each specimen i.e. grains, dislocations, voids, etc. The mechanisms responsible for deformation and fracture of thin films can thus be identified. Two methods were developed in order to perform TEM analysis. The first one was post mortem analysis through Focussed Ion Beam (FIB) cut specimens. The second one needed more process development but allowed in situ observation.

7.2.1 Post-mortem observation

After release of the micromachines, one specimen is selected for TEM observation. The specimen is cut on one side using FIB. It is then glued on a micro-manipulator with a carbon deposit. FIB cutting is again used at the other side of the specimen. Finally, the specimen glued to the micro-manipulator is transferred on a TEM copper grid.

This technique offers direct TEM observation of the specimen from the top. Every specimen can be observed this way without the need of particular processing in cleanroom. Thick films can be observed provided they are first thinned down to 200 nm with the FIB. The main drawbacks of this post-mortem analysis are the following:

- The use of micro-manipulator is delicate and care must be taken in order to avoid breaking of the specimen.
- Only one specimen can be prepared at a time.
- TEM observations are made on an unloaded specimen.

- As already stated in Section 2.2, the use of FIB can introduce defects into the thin film specimen.

7.2.2 In situ observation

In order to avoid all the aforementioned problems, a window can be etched on the backside of the wafer, allowing direct observation of the entire specimen by TEM. The fabrication process is the same as the one described in Section 5 until the patterning of the specimen layer (Section 5.4). The active face of the wafer is then covered with a protective resist. Grinding is then used to thin down the substrate to 200 µm. After grinding, a positive photoresist is deposited on the back face and patterned (SPR2020 (4.5 µm)). This requires a specific mask that is designed to create windows under the structures of interest and to pre-cut the TEM samples (Fig. 7.3).

The etching of the silicon is performed using a modified Bosch process. This process alternates repeatedly between two modes to achieve nearly vertical etching:

1. Nearly isotropic plasma etching (Fig. 7.4b).
2. Deposition of a chemically inert passivation layer (Fig. 7.4c).

The passivation layer protects the entire substrate and prevents further etching. During the etching phase, the directional ions that bombard the substrate attack the passivation layer at the bottom of the trench (but not along the sides). They collide with it and sputter it off, exposing the substrate to the chemical etchant. These etch/deposit steps are repeated many times in order to perform deep etching of the silicon wafer.

The initial grinding of the substrate is performed because Bosch process cannot create perfect vertical trenches for more than 200 µm and because the final sample cannot be too thick for the chamber of the TEM. This step can however be avoided by using thinner substrates from the beginning of the process. In this case, extra care must be taken through the

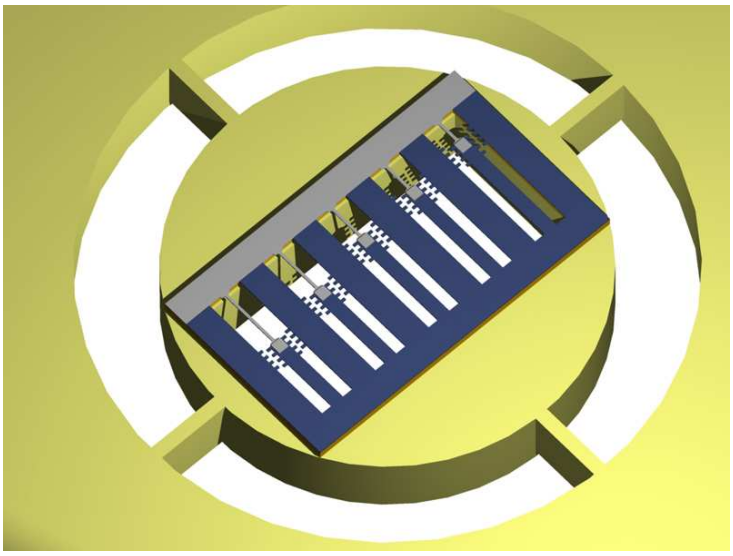

(a)

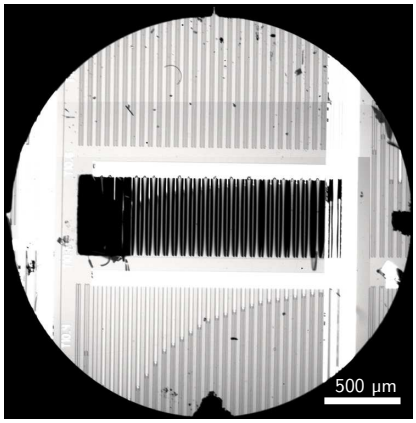

(b)

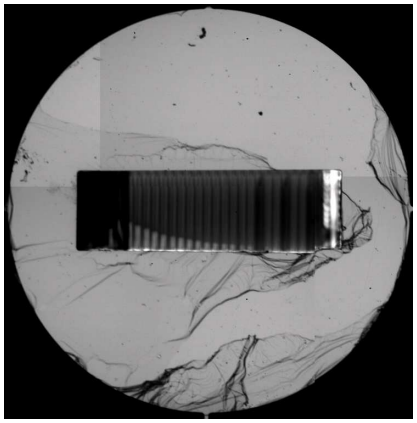

(c)

Figure 7.3: *Design of back etching mask: (a) 3D schematic view, (b) processed sample top view, (c) processed sample back view.*

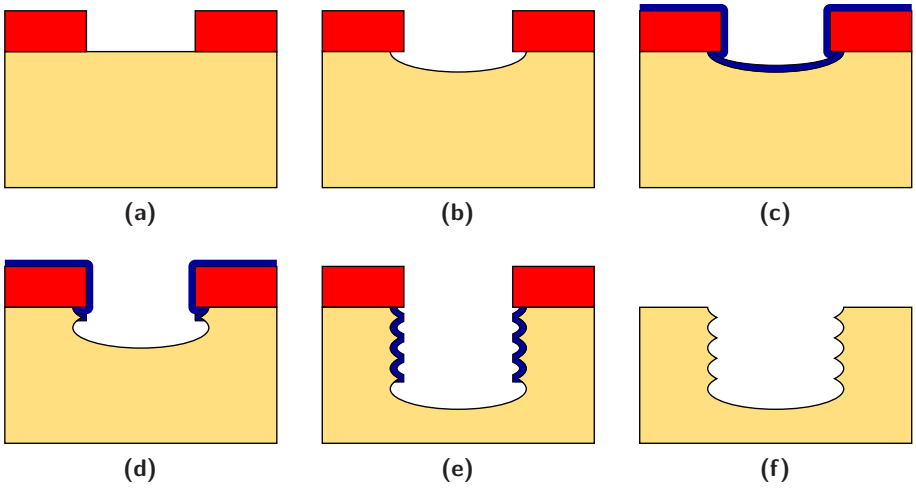

Figure 7.4: *Steps in a Bosch process: (a) initial configuration, (b) first etching step, (c) first passivation step, (d) second etching step, (e) after a few cycles, (f) final configuration.*

whole process due to the fragility of the substrates but this alternative proved to give the best results.

The etching of silicon is stopped when the sacrificial layer is reached (Fig. 7.4f). The standard process is continued with the release of the sacrificial layer (Section 5.5) and the critical point drying (Section 5.6). After drying, the pre-cut samples can be separated from the wafer by cutting the remaining tethers. Those samples can be directly put in a TEM for analysis.

This process offers many advantages over the previous method:

- Many specimens can be prepared at the same time depending on the design of the back etching mask.
- Specimens are not unloaded for TEM observation.
- As no FIB is being used for the sample preparation, no defects are introduced in the specimen material.

Apart from the more complex fabrication process (need for a specific mask), the main drawback with this technique is the manipulation of very brittle 200 µm-thick silicon wafers.

This technique cannot still be called in situ as the load is not modified in the TEM chamber. Some authors [87] were able to conduct true in situ tensile tests in TEM by the use of an external loading device. In order to perform in situ tests, the idea here was to add a small increment of strain in the TEM by decreasing slightly the temperature. Due to their thermal expansion coefficient, all the materials present in the TEM chamber (i.e. Si substrate, Si_3N_4 actuators and Al specimens) will contract. Thermal expansion coefficient of Si_3N_4 and Al being a priori larger than the one of silicon, actuators and specimens will contract more than the silicon. This should result in an increase in the stress and strain experienced by each specimen. Monitoring of the temperature should enable to control the load on a pre-loaded specimen. However, the cooling of the specimens shaped like the ones of Fig. 7.3 from room temperature down to $-150\,°C$ did not show evidence of additional loading. This was attributed to the fact that the thermal expansion coefficients (CTE) evolve with temperature. If this evolution is known for silicon [43], it is not the case for silicon nitride. The CTE of Si and Si_3N_4 are probably not that much different below room temperature which does not provide the expected thermal loading. Other actuating materials should be used to validate the technique but no further attempts were made in the context of this thesis. In situ TEM observations of the microstructure evolution could be performed in this way.

Part III

Application of the internal stress actuated micro-tensile stage concept to the study of Al and AlSi films

Part III presents and discusses the results generated with self actuated micro-tensile stages in order to study the mechanical response of pure Al and AlSi(1%) films. Chronologically, most of the work was first devoted to the study of pure Al films. The goal was to prove the ability of the technique to extract the mechanical properties of a thin film material. Most of the process and design improvements were made based on pure Al testing. The fast relaxation phenomena occurring in pure Al even at room temperature (see Section 9.2) did not permit to measure the hardening law but still interesting data about the ductility of the films were obtained. In order to benefit from the process specifically optimised for Al, it was decided to use a similar film material as a proof of concept. AlSi(1%) was thus selected as it was expected to involve slower relaxation. The results and analysis on AlSi are presented first (Chapter 8) as they illustrate better the test procedures developed in part II. The results and analysis of pure Al films are presented afterwards in Chapter 9.

Chapter 8

Mechanical response of Al-Si thin films

8.1 Materials and experimental procedures

AlSi(1%) films were deposited by sputtering using a reactor similar to the one depicted in Fig. 5.6 in Section 5.4. The AlSi target is always the same so that no other material should be found in the deposition chamber. The chamber pressure prior to argon admission is 1.10^{-7} mbar and reaches 3.10^{-3} mbar during deposition. Twelve substrates can be deposited at a time. The wafers rotate around two axis to ensure uniform deposition. Substrates are heated to 250 °C prior to deposition and the deposition rate is fixed to 6 $Å s^{-1}$. The only varying parameter from one deposition to another is the duration of the deposition process which allows monitoring the thickness of the film.

For each process involving AlSi(1%) test structures, one blanket wafer is added at the metallisation step. After AlSi deposition, this blanket wafer is used for internal stress measurement using the wafer curvature method (see Section 6.5). The processed wafers are patterned using positive lithography (Fig. 5.4) and plasma etching as already stated in Section 5.4.

Three films thicknesses were investigated in the present study: 205 nm,

415 nm and 1080 nm. Most of the analysis will be performed on the thinnest film. The two other film thicknesses involved particular processing conditions. In the case of the 415 nm-thick film, just after etching of the AlSi with a Cl_2 and CCl_4 plasma, the wafers were put for 10 seconds in a solution of HF, HNO_3 and acetic acid. This step was initially performed to etch the silicon content of the Al as the plasma recipe is "designed" for etching of pure Al. Unfortunately, the etching solution was found to damage the edges of the newly patterned specimens (Fig. 8.1a) as well as the actuator material. The geometry of the beams is thus affected and the accuracy of the measurements is decreased. In the case of the 1080 nm-thick film, SEM analysis revealed a sponge-like microstructure (Fig. 8.1b) very different from standard sputtering morphology. Moreover, the thickness of the actuator layer in this last case was too small to induce significant straining of the specimen material. In the following, the mechanical properties of the three deposited films are presented but care must be taken when interpreting the data on the 415 nm and 1080 nm-thick films.

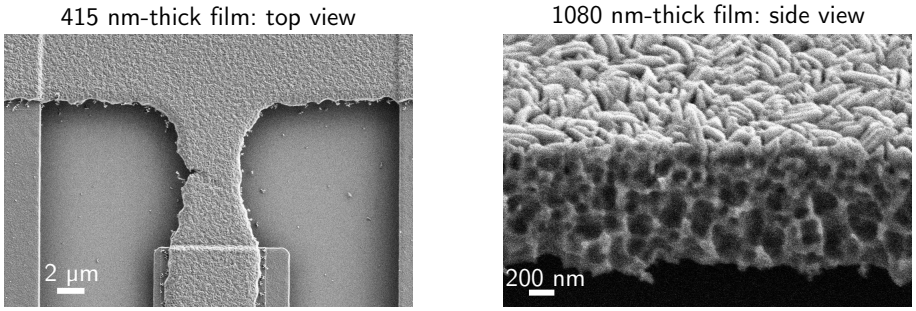

Figure 8.1: *SEM pictures showing (a) the non uniform edges of the* 415 nm*-thick AlSi film and (b) the unusual microstructure of the* 1080 nm*-thick AlSi film.*

8.2 Stress-strain curve analysis

The strain-strain curves presented in this section will be identified as belonging to a "Tx-y" set of structures. As already stated in Section 4.4.6, a "Tx-y" set of structures consists of 30 micromachines named from 1 to 30 with x being the width of the actuator beam in micrometres, y being the width of the specimen beam in micrometres. Micromachine 1 corresponds to the least deformed specimen beam whereas micromachine 30 is the most deformed one. In generation 3, the test structures of a series have the same total length (actuator + test specimen). The total length is 500 µm, 1000 µm, 1500 µm or 2000 µm. Structures with the same number should provide the same point in a stress-strain curve independent of the total length of the test structure. The only difference lies in the displacement measurement which should scale with the length scaling factor. Here, only the results on the longer structures (2000 µm) are provided giving the most accurate measurements. In some cases, smaller structures sustain higher strains (see Section 9.3.1). In this particular case, the information available in the smaller structures is added to the longer ones.

The stress-strain curve of Fig. 8.2 is obtained from a "T10-6" set of structures of a 205 nm-thick AlSi film. True stress and true strain in each specimen beam are extracted using Eq. 4.7 and Eq. 4.6 presented in Section 4.2. The 23 first tensile stages in the set are deformed while the 7 last are broken, with failure taking place inside the specimen beam. A test structure "24" from the 1500 µm-long set and a "25" from the 1000 µm-long set were found to sustain a higher deformation. They have thus been added to the stress-strain curve. All further stress-strain curves are obtained following the same procedure.

The Young's modulus of AlSi(1%) was measured by nanoindentation on a 1080 nm-thick AlSi film and found equal to 70 GPa. The elastic line corresponding to this Young's modulus has been added to Fig. 8.2. One can see that even the less deformed structure lies outside the linear regime, at a stress equal to ∼150 MPa. The biaxial stress was measured on a blanket wafer with the same deposit and wafer curvature measurement using the Stoney equation Eq. 6.8 provided a tensile internal stress value

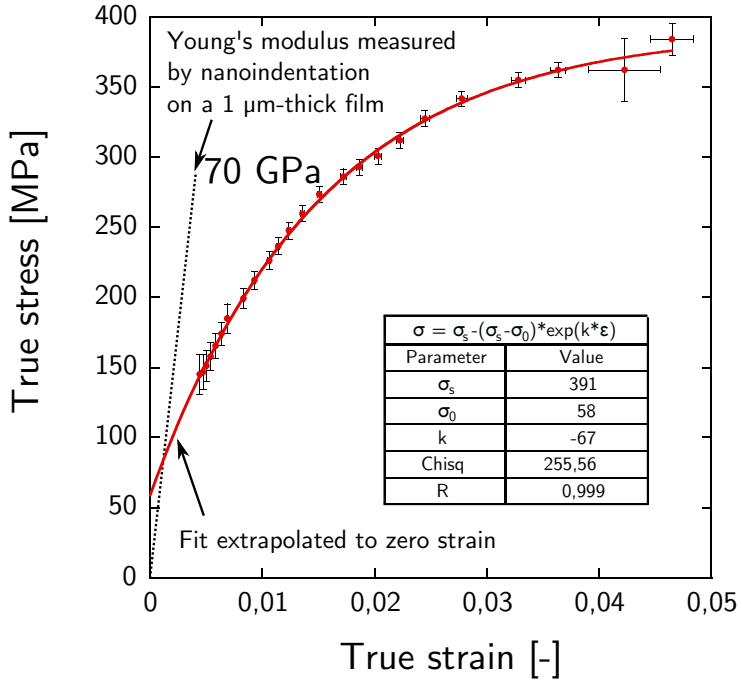

Figure 8.2: *True stress-true strain curve obtained from a "T10-6" set of structures of a* 205 nm*-thick AlSi film. The fitting is performed using a Voce law.*

around 270 MPa. This high value comes essentially from the fact that the deposition was performed at 250 °C and that the thermal expansion coefficient of AlSi (2.1 10^{-5}°C^{-1}) is higher than silicon (2.3 10^{-6}°C^{-1}). The absence of data in the linear regime indicates that internal stress is probably higher than the yield strength of the film. As a matter of fact, Fig. 8.3 depicts the different cases that can be encountered. It must be noted that the biaxial internal stress measured by wafer curvature has to be mutiplied by $1-\nu$, ν being the Poisson ratio of the film material, in order to get the internal stress experienced by a uniaxial beam.

When the internal stress is higher than the yield strength of the test material, data in the elastic regime can be extracted only if unloading of the internal stress occurs. This happens only if a negative displacement

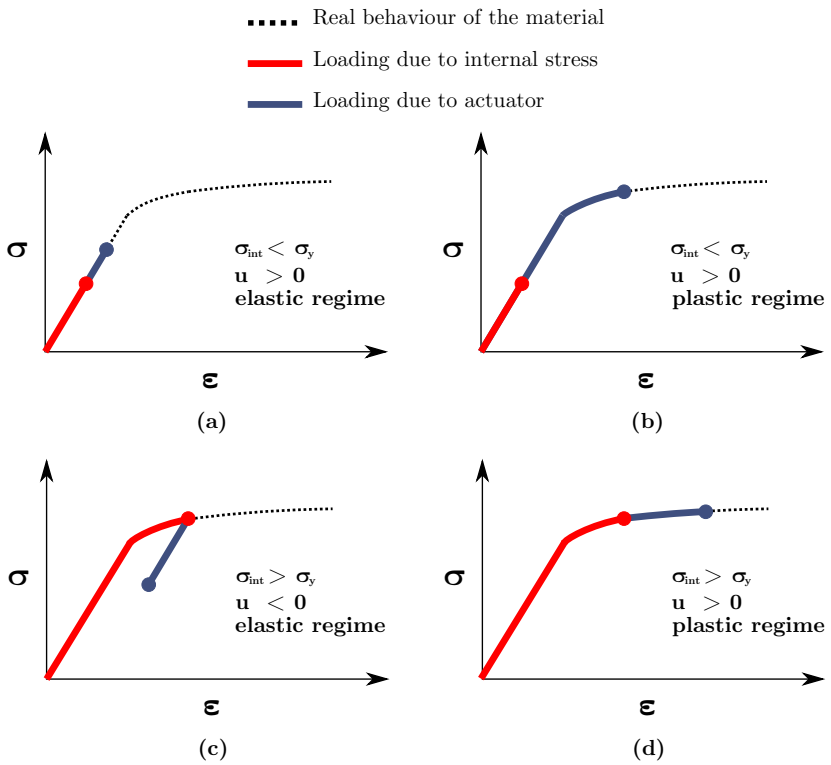

Figure 8.3: *Different situations that can arise when releasing structures of a material deposited with tensile internal stresses. σ_{int} is the tensile internal stress, σ_y is the yield strength and u is the displacement measurement.*

is measured, that is, if the specimen beam pulls on the actuator beam (Fig. 8.3c). Negative displacement never occurred with the design of generation 3 and 4 set of masks for all the AlSi films tested. It means that in all cases, the deformation contribution coming from the actuator is positive and is added to the mismatch strain of the specimen material (Fig. 8.3a, b and d).

The concept of internal stress actuated micro-tensile stages is thus not suitable for extracting the elastic behaviour in this particular case. However, the plastic regime is well captured from 0.4% of deformation until

specimen failure. The error bars in Fig. 8.2 are derived from the error made on the measurement of the displacement u (accuracy = 50 nm). It must be noted that the Young's modulus (E) and the mismatch strain (ε_a^{mis}) of the actuator material as well as the initial cross-sections of the actuator (S_{a0}) and of the specimen beams (S_0) are considered to be constant over the entire set of structures. These parameters affect only the stress determination and any error would translate the stress-strain curve vertically. Similarly, the mismatch strain of the specimen material (ε^{mis}) is considered to be constant over the measured structures. An error on that parameter would translate the stress-strain curve horizontally. The constant values taken for the above parameters is justified by the fact that all structures are located on an area of a few square millimetres. Variations in the properties or geometry of the films over such a small area are not expected. The different values of the constant parameters used for the three studied AlSi films are shown in Table 8.1[1].

Due to the discrete nature of the technique, the complete behaviour of the film is not known but the number of points is sufficient to allow proper fitting. A Voce law (see Eq. 8.1) is shown to fit very well with the data in Fig. 8.2. It must be noted that with the present technique, the 25 points of Fig. 8.2 are extracted from 25 different tensile test structures. The stress-strain curve can thus be viewed as a mean stress-strain curve giving a statistically representative behaviour of the film material. From that curve, the engineering yield strength corresponding to 0.2% of plastic deformation is found to be around 140 MPa which corresponds approximately to the first data point. The strain hardening capacity is analysed further and together with the 415 nm-thick film (see Fig. 8.5). The maximum strain observed (4.7%) is a good approximation of the fracture strain. However, imperfections in the specimen beams can affect the maximum strain as fracture occurred earlier (at smaller strain) for longer specimens beams. There is indeed an increasing probability of having larger imperfections for longer specimens. Hutchinson and Neale [69] have shown that plastic localisation is triggered earlier in the

[1]The mismatch strain of the AlSi was not measured in the case of the 415 nm-thick film and was chosen so that the "elastic" points fit in the slope of the Young's modulus measured by nanoindentation.

Film thickness	205 nm±5	415 nm±5	1080 nm±5
Set of structures	"T10-6"	"T10-6"	"T10-2"
ε^{mis} extracted from free cantilever beams [-]	$3.2\ 10^{-3} \pm 1\ 10^{-4}$	$1\ 10^{-3} \pm 1\ 10^{-4}$	$0.8\ 10^{-3} \pm 1\ 10^{-4}$
ε_a^{mis} extracted from auto-actuated micromachines [-]	$3.0\ 10^{-3} \pm 1\ 10^{-4}$	$3.0\ 10^{-3} \pm 1\ 10^{-4}$	$3.0\ 10^{-3} \pm 1\ 10^{-4}$
E considered (extracted from nanoindentation of a 300 nm-thick Si_3N_4 film [7]) [GPa]	240	240	240
Biaxial internal stress (Stoney) [MPa]	$\simeq 270$	$\simeq 210$	$\simeq 200$

Table 8.1: *Parameters used for extraction of the stress-strain curves of the three AlSi film thicknesses with results given in Fig. 8.2, Fig. 8.4 and Fig. 8.6. The internal stress in the AlSi film is added at the end of the table but is not used to determine the stress-strain curve.*

presence of imperfections. The influence of imperfections on the ductility is not studied for AlSi films but is analysed later for the case of pure Al films in Section 9.3.

$$\sigma = \sigma_0 - (\sigma_0 - \sigma_s)\exp(k\varepsilon) \tag{8.1}$$

where σ_s is the saturation stress, σ_0 is the true stress at the onset of plastic deformation, k is a constant and σ and ε are the true stress and true strain in the specimen, respectively.

The stress-strain curve of the 415 nm-thick AlSi film is given in Fig. 8.4 and comes from a "T10-6" set of structures. The internal biaxial stress measured on a blanket wafer was a approximately ∼200 MPa. The yield strength can be determined as some points of the stress-strain curve lie in the elastic regime. This means that the stress consecutive to deposition was not high enough to cause permanent deformation in the film and the situation is similar to the one depicted in Fig. 8.3a and b. The yield strength corresponding to the loss of linearity of the stress-strain curve (σ_0) is determined to be around 195 MPa whereas the engineering yield strength is around 220 MPa. The higher yield strength observed in the thicker film is unexpected as it is opposite to what is reported in the literature. It will be discussed later.

For both the 205 nm-thick and the 415 nm-thick films, the stress increases significantly before fracture indicating a high strain hardening capacity. The strain hardening capacity evolution is shown for both films in Fig. 8.5. Two characteristic strain hardening parameters are defined:

- the hardening rate $\Theta = d\sigma/d\varepsilon_p$
- the incremental strain hardening exponent $n_{incr} = d\ln\sigma/d\ln\varepsilon_p$.

In the definition of both parameters, ε_p is the plastic strain.

In Fig. 8.5a, Θ is plotted as a function of $\sigma - \sigma_y$ where σ_y is the engineering yield strength. Θ exhibits an initial value one order of magnitude

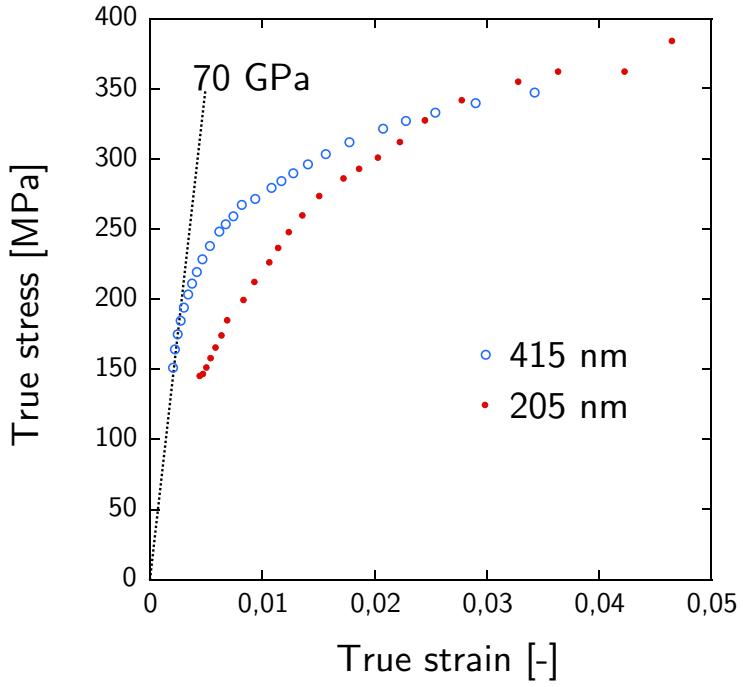

Figure 8.4: *True stress-true strain curve obtained from a "T10-6" set of structures of a* 415 nm*-thick AlSi film and compared with the curve from the* 205 nm*-thick film.*

higher than what is usually reported for polycrystals [79]. The maximum expected hardening rate is indeed about $E/50$ for a polycrystal with micron-sized grains which would be around 1.4 GPa in the case of AlSi. Similarly to the results on evaporated Pd films [70] [15], this high initial value indicates that regions of the film still behave elastically while other regions deform plastically giving rise to a large elastoplastic transition. This long elastoplastic transition has been analysed for instance by Verdier et al. [68].

Fig. 8.5b shows the variation of n_{incr} for both films. n_{incr} first reaches a maximum ($\simeq 0.5$) then decreases as plastic deformation proceeds in the case of the 205 nm-thick film. For the 415 nm-thick film, n_{incr} stays between 0.1 and 0.15. The value reached by this parameter for both films are much larger than what is currently reported for nanocrystalline materials. The initial high strain hardening is the result of the strong initial kinematic hardening contribution.

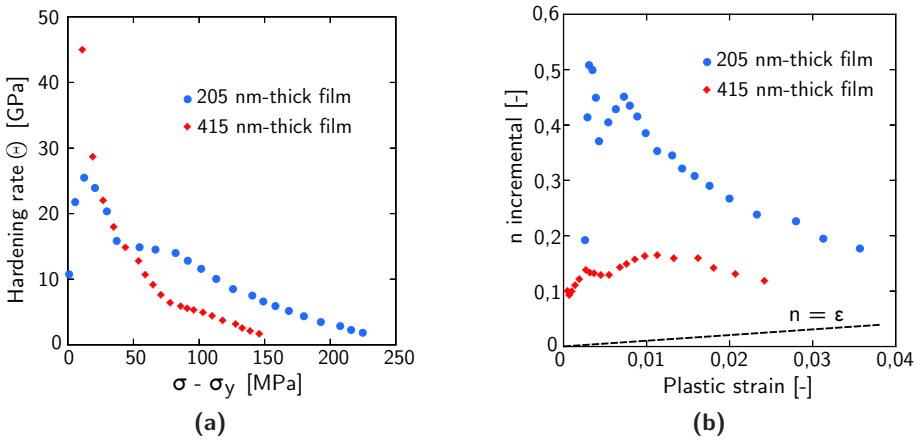

Figure 8.5: *Variation of (a) the hardening rate Θ as a function of $\sigma - \sigma_y$ and (b) the incremental strain hardening exponent n_{incr} as a function of the plastic strain for the* 205 nm*-thick and the* 415 nm*-thick AlSi films.*

The dotted line in Fig. 8.5b shows the Considère criterion which predicts that necking initiates when the plastic strain is equal to n_{incr}. Obviously,

the criterion is not reached and fracture occurs earlier. This can be explained by the presence of imperfections in the specimen beams. From that point of view, a ductility size effect cannot be analysed for the two considered films. Indeed, the high imperfection density in the 400 nm-thick film (see Fig. 8.1a) suggests that the ductility of this film could have been larger with a reduced concentration of imperfections. These imperfections were inherent to the non-standard processing conditions of the 400 nm-thick film. A proper comparison with the 205 nm-thick film should be performed on another batch involving similar process conditions. This has not been done as the focus was put on another phenomenon affecting AlSi films and described in Section 8.3.

The stress-strain curve from the 1080 nm-thick AlSi film is given in Fig. 8.6 and comes from a "T10-2" set of structures. This set is the only one for which a displacement could be measured. The actuator layer involved in this process was indeed too thin to induce enough displacement. The error on stress and strain is thus larger than for other stress-strain curves and fracture could not be attained within this set. Moreover, the particular morphology of the deposit and the difficult etching procedure (large thickness to be etched) suggest that this batch was probably a "one shot result" and could not be exactly reproduced. However, the stress-strain curve is shown in Fig. 8.6 to show the ability of the technique to extract the elastic properties of a thin film material when its internal stress is far below its yield strength. The yield strength of the 1080 nm-thick film is indeed quite high ($\sim$450 MPa) and again higher than thinner films. But, as this value is far larger than the internal stress measured by the wafer curvature method (202 MPa), a lot of structures lie in the elastic part of the curve. The slope of this elastic part is similar to the Young's modulus extracted by nanoindentation.

The increased yield strength of the 1080 nm-thick AlSi film with respect to the 205 nm-thick AlSi film is apparently contradictory to the Nix-Freund model [96] which predicts a $1/h$ dependence of the thickness strengthening (h being the thickness of the film). However, the thickness is not the only parameter influencing the yield strength and the full microstructure should be taken into account. TEM observations have thus been made on the two films to determine the grain size and

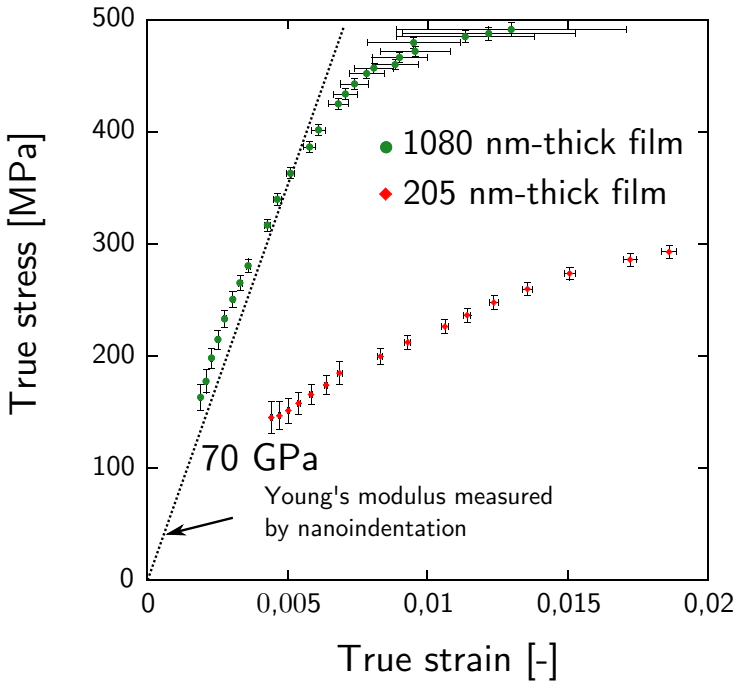

Figure 8.6: *True stress-true strain curve obtained from a "T10-2" set of structures of a* $1080\,\mathrm{nm}$*-thick AlSi film. The mismatch of the specimen material* (ε^{mis}) *is measured on cantilever beams and is equal to* $0.8\ 10^{-3}$.

morphology[2]. Fig. 8.7a shows a TEM top view from a 205 nm-thick AlSi structure extracted with the post-mortem technique described in Section 7.2.1. The grain size is approximately equal to 200 nm, with only one grain over the thickness. Surprisingly, the TEM pictures did not reveal any Si precipitate in the Al matrix. The solubility of Si in Al is indeed very low at room temperature and the phase diagram illustrated in Fig. 5.7 of Section 5.4 claims for a two-phases alloy in the case of AlSi(1%). A possible explanation could be that the deposition of the Al alloy did not occur under equilibrium conditions. The Al would then be supersaturated in Si. A more probable explanation would be that the silicon gathers in nanoclusters in the volume of the grains or at grains boundaries. These clusters could only be observed by performing high resolution (HR) TEM pictures or by observing dislocations pinned by these clusters. The 1080 nm-thick AlSi film being too thick to be transparent to electrons, a cross-sectional FIB thin foil was prepared for TEM investigation. Fig. 8.7b is a TEM picture from the thin foil which reveals a columnar structure with a lateral grain size of 200 nm. The grain sizes of the two films are thus similar and only the thickness, and thus the grain aspect ratio, differs from one film to the other.

In an attempt to understand the size-scale plasticity in geometrically confined systems such as thin films, Espinosa et al. [34] [31] provided a possible explanation for the particular behaviour observed in AlSi. They indeed conducted 3D Discrete Dislocation Dynamics (DDD) simulations. They assume that for the grain size considered (200 nm) plasticity occurs by dislocation motion and that the dislocation sources are located at the grain boundaries. The grain boundaries are considered as impenetrable to dislocations whereas the top and bottom faces are considered as free surfaces (freestanding film). The simulations reveal that once activated, the dislocation sources propagate in their slip plane and are either absorbed by free surfaces or stored at grain boundaries. For a fixed grain size (200 nm) and four different thicknesses (200 nm, 400 nm, 600 nm and 1000 nm), the DDD simulations were able to capture an increased strain

[2]Unfortunately, no grain size analysis was performed on the 415 nm-thick film. The further size effect analysis is thus performed based on the TEM observations from the 205 nm-thick and 1080 nm-thick AlSi films.

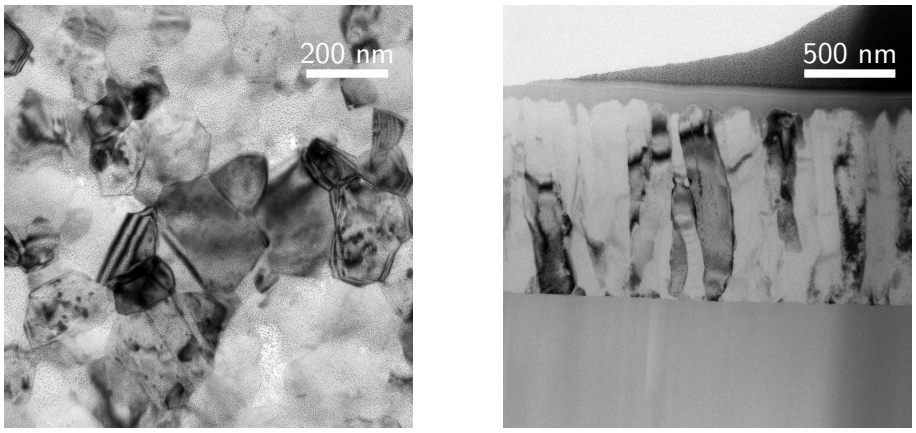

Figure 8.7: *TEM pictures extracted from AlSi films (a) Top view from a* 205 nm*-thick AlSi structure and (b) Cross-section view from* 1080 nm*-thick AlSi film. In the two cases the grain size is around* 200 nm *with one grain over the thickness (columnar structure).*

hardening and yield stress when decreasing the thickness. Espinosa et al. [34] provide two reasons in order to explain this size effect:

- The 200 nm-thick film possesses less grain boundary area and hence a lower probability of dislocation nucleation at a given stress than the thicker films.
- For smaller thicknesses there is a higher probability for the dislocations to encounter free surfaces and be partially adsorbed by them, which results in a smaller available free path and consequently in a smaller potentiality for the dislocations to generate plastic strain by sweeping area inside the crystal.

However, the aspect ratio of the grains can alter the second effect. Indeed, for the thickest films (highest aspect ratio), there is a higher probability for dislocations to intersect with one another and, therefore, form junctions and networks. This event produces an increase of the internal

stress (back stress) during the deformation process and, hence, an obstacle to further dislocation nucleation. As a consequence, thicker films with high aspect ratio can experience a slight increase of the flow stress. This model does not necessarily fully applies to the case of the AlSi film analysed here. Indeed, it is not sure whether the grain boundaries are completely impenetrable to dislocations. In addition, the hypothesis of free surfaces might be discredited by the presence the native oxide layer on the Al alloy. The aspect ratio size effect is probably not sufficient to explain the increased yield stress in the 1080 nm-thick AlSi film compared to the thinner ones. Nevertheless, it emphasises the need of TEM to correlate the mechanical behaviour to the microstructure.

8.3 Strain rate sensitivity

In Section 8.2, all the stress-strain curves are extracted by measuring the equilibrium position defined in Fig. 4.4 of Section 4.2. This equilibrium position is reached almost instantaneously after the release of the structures but the measurement is performed after the rinsing and drying step which last for about one hour. If the tested material experiences a time dependent response, the equilibrium position will evolve with time giving access to the rate sensitivity exponent and the activation volume of the tested material. This section aims thus at explaining the procedure to extract these parameters and analyses the data on the 205 nm-thick film[3].

8.3.1 State of the art

The enhanced strain rate sensitivity of nano-grained metallic materials with respect to coarse-grained metals has been repetitively reported in the recent literature [30] [114] [132]. The mechanisms responsible for this strain rate sensitivity involve thermally assisted dislocation nucleation and glide mechanisms, diffusion creep, grain boundary migration

[3]This section derives mainly from a paper which is going to be published in Review of Scientific Instruments [18].

and grain growth. These thermally activated mechanisms lead to stress relaxation and creep, negatively impacting the reliability of devices and coatings made with these materials when subjected to internal stresses or to constant external forces. Furthermore, an enhanced strain rate sensitivity has a marked positive impact on ductility, e.g. Neale and Hutchinson in [69], which is a key property in many applications such as in flexible electronics, and in forming of coated sheets. High throughput reliable testing procedures for measuring the rate dependent deformation on nanoscale samples are thus heavily needed. The existing methods are reviewed in this section.

Two parameters are generally used to describe the time dependent permanent deformation response effect of materials: an empirical rate sensitivity exponent (m) and the activation volume (V_{act}). The rate sensitivity exponent is defined as:

$$m = \frac{\partial \ln \sigma}{\partial \ln \dot{\varepsilon}_p} \tag{8.2}$$

where σ is the stress in the material and $\dot{\varepsilon}_p$ is the applied plastic strain rate.

The activation volume is defined as:

$$V_{act} = M k_B T \frac{\partial \ln \dot{\varepsilon}_p}{\partial \sigma} \tag{8.3}$$

where σ is the stress in the material, $\dot{\varepsilon}_p$ is the plastic strain rate, T is the temperature, k_B is the Botzmann constant and M is the Taylor factor which connects the macroscopic tensile stress to the microscopic resolved shear stress. V_{act} is usually given in units of b^3, b being the length of the Burgers vector of the material. This definition of an activation volume is based on an assumed Arrhénius law for thermally activated mechanisms controlled by the local shear stress. The value of M is known to be 3 in FCC metals with randomly oriented large grains where plasticity is controlled by dislocation glide. In thin film testing, grains are small, and thin films are usually textured and the mechanisms involved are probably not limited to dislocation glide. A value of $\sqrt{3}$ for M is

generally reported in the literature [131] [132]. Now, if the deformation mechanism is controlled by something else than dislocation (e.g. diffusion) the value of M is different. As the controlling mechanism cannot be guessed a priori, activation volume will be normalised by the Taylor factor in the following.

Extraction of these two parameters in thin films requires performing tests at different strain rates. There are three main categories of methods.

- The first category involves strain rate jump experiments. In these experiments, the specimen is deformed under constant strain rate $\dot{\varepsilon}_1$ up to a stress $\sigma_1(\dot{\varepsilon}_1)$. The strain rate is then increased very rapidly to a value $\dot{\varepsilon}_2$ associated to a stress $\sigma_2(\dot{\varepsilon}_2)$. The jump in the strain rate is performed fast enough so that the microstructure before and after the jump remains the same. A variant of the strain rate jump test simply consists in performing tensile or compressive tests at different rates.
- The second category involves stress relaxation tests where a fixed displacement (or strain) is imposed to a specimen while the load evolution is recorded as a function of time.
- The third category corresponds to creep tests, where a fixed load is imposed to the specimen while the displacement is recorded as a function of time.

In the two last categories, the microstructure evolves during the test which must be taken into account when analysing the data. Any combination of these elementary testing methods can be used.

Whatever the selected test method, the transfer of the classical macroscopic techniques to small scale samples leads to instrumentation difficulties due to the small force and displacement values that have to be measured or controlled accurately while ensuring that the electronics remains stable over long period of time. Thermal drift effects are often a key issue. Extracting values of the rate sensitivity involves taking derivatives of strain rate versus stress which puts a burden on the level

of accuracy that must be attained. Other difficulties involve the manipulation of the very small samples, the alignment of the specimens, the measurement of the dimensions of the specimens and the production of minimum geometrical imperfection.

Strain rate jumps tests, under uniaxial tension, have been reported on thin foils of nanocrystalline (nc) Ni [131] and nc Cu [13]. Usually, several strain rate jumps are performed on the same specimen as the flow stress depends on the initial strain at which the test is performed. Different values for m and V_{act} can thus arise for different initial strains indicating a change of the relaxation mechanism and/or of the energy barrier on the level of permanent deformation. Due to the difficulty to perform fast strain rate jumps especially in nanosystems, the rate sensitivity exponent is often calculated by comparing yield strength measurements from tensile tests performed at different strain rates e.g. for nc Ni [19] and for nc Cu [90]. The values are estimated at the same level of plastic deformation. Emery et al. [30] performed tensile tests on Au films as thin as 200 nm-thick. The strain rate sensitivity parameter was extracted based on yield strength versus strain rates from tests performed on several samples. Gianola et al. [48] describe strain rate jump tests performed on Al 200 nm-thick films showing large strain rate sensitivity. An advanced experimental setup developed by Jonnalagadda et al. [74] enables tensile testing of thin films spanning a broad area of strain rates down to 10^{-6} s^{-1}.

Nanoindentation has also been used to determine the rate dependent behaviour of thin metallic films. The complexity in the analysis does not come from the setup but from the complex stress state. The strain field around the tip of the indenter is far more complex than the uniform field in a tensile test. Lucas and Oliver [91] have proposed a technique allowing constant strain rate testing during depth sensing indentation. Schwaiger et al. [114] used this technique to indent nc Ni foils while the strain rate sensitivity exponent was extracted by computational modelling. Constant load nanoindentation can also be used [89] [131]. Now, as already stated in Section 2.1.1, the maximum indentation depth has to be limited to a small fraction of the thickness of the specimen in order to avoid substrate effects. This fraction varies from 20% to less than 1%

depending on the stiffness mismatch between specimen and substrate. Extraction of time dependent response of films thinner than typically 200-300 nm requires special development and other loading configurations should be preferred due to the ease of results interpretation.

In all the aforementioned techniques, the strain rate typically varies between 10^{-6} and 10^{3} s^{-1}. Slower strain rate testing is not performed as it would require monopolizing a test equipment for a long time while ensuring a stable measurement especially regarding thermal and electronic drift.

8.3.2 Data reduction scheme

The concept of internal stress-driven on-chip test structures provides a new tool to perform stress relaxation experiments. For a particular test structure, once a stable position is reached in the force-displacement diagram, stress relaxation can take place through thermally activated deformation mechanisms which depend on the material, microstructure, state of the surface, thickness and temperature. During relaxation, the stress in the specimen beam will decrease while the strain will increase following the force–displacement relationship imposed by the actuator "spring" as shown in Fig. 8.8. By monitoring the evolution of the displacement with time, it is possible to characterise the relaxation behaviour of the material and to extract the rate sensitivity exponent and activation volume. The test conditions correspond to a creep test performed on a material attached to a spring.

The procedure is the following. The displacement of each tensile stage is recorded as a function of time. Time t_0 in Fig. 8.8 corresponds to the time just after release when the stable position of the structures is reached. No imaging and thus no measurement can be made at time t_0. The post release steps, involving the rinsing, supercritical drying and transfer to SEM take about one hour. Hence, no data is available for the relaxation occurring in the specimens during the first hour of the loading. The first measurement is performed at time t_1. The n next measurements provide a discrete variation of the displacement with time $u(t_i)$. The small number of measurements (e.g. 11 measurements in the

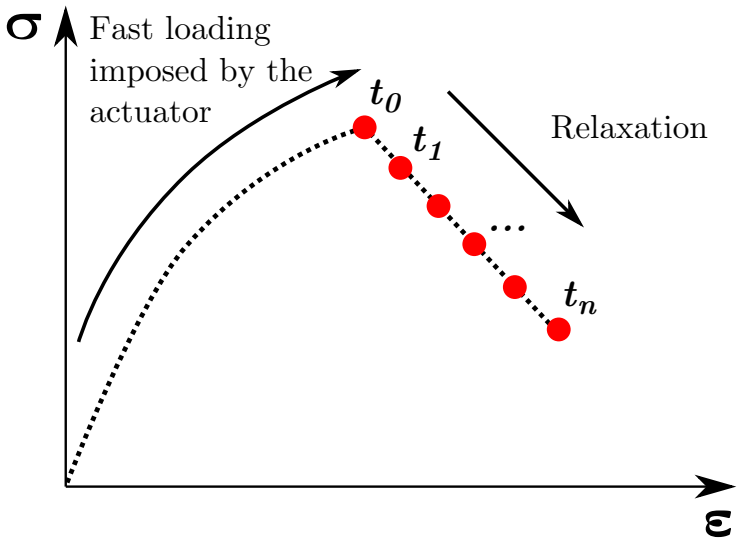

Figure 8.8: *Evolution of stress and strain in a relaxation test performed with a particular micromachine.*

case analysed in Section 8.3.3) is due to the limited resolution of the displacement measurement. Indeed, the displacement variation cannot be smaller than a few tens of nanometres in order to be captured (see Section 6.2). The determination of the rate sensitivity exponent and activation volume requires the derivation of strain versus time. In order to avoid a large error on the strain rate, a fitting of the displacement versus time raw data is performed (Fig. 8.9a) using cubic splines. It provides a continuous relation $u(t)$ between time and displacement. Then, using Eq. 4.6 and Eq. 4.7 the plastic strain (Fig. 8.9b) and stress (Fig. 8.9c) are computed as a function of time. The plastic strain is calculated as $\varepsilon - E\varepsilon_{elastic}$ where $\varepsilon_{elastic} = \sigma/E$, E being the Young's modulus of the test material extracted by nanoindentation. The numerical derivation of the plastic strain gives access to the variation of the strain rate with time (Fig. 8.9d). Finally, the stress can be related to the strain rate for each tensile stage at any time, providing the strain rate sensitivity exponent and activation volume using Eq. 8.2 and Eq. 8.3, respectively (Fig. 8.9e). This procedure is summarised in Fig. 8.9.

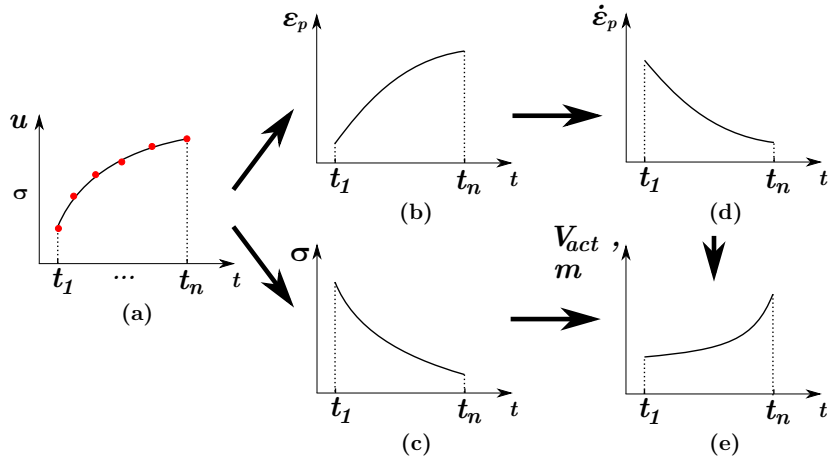

Figure 8.9: *Methodology for the extraction of the strain rate sensitivity parameters from a specific test structure.*

8.3.3 Results and discussion

The methodology described in Section 8.3.2 is applied to the 205 nm-thick AlSi film and the relaxation is shown in the stress-strain curve of Fig. 8.10. A "T10-6 2000" set of structures is considered. After etching of the sacrificial layer, rinsing and critical point drying, the patterned sample is transferred in the SEM chamber for displacement measurements. The 23 first tensile test structures in the set are deformed while the 7 last are broken. As a test structure "24" from the 1500 µm-long set and a "25" from the 1000 µm-long set are found to sustain a higher deformation, a first displacement measurement is performed for these two additional structures. Further displacement measurements are then performed on the 25 unbroken structures with increasing time interval. No additional structure failed during the relaxation time. Because the AlSi films experienced unexpectedly fast relaxation, the sample is kept in the SEM chamber between displacement measurements. Eleven measurements were performed between $t = 1$ h and $t = 14$ h, $t = 0$ s being the time corresponding to the release.

The fitting procedure of the time versus displacement relation is illus-

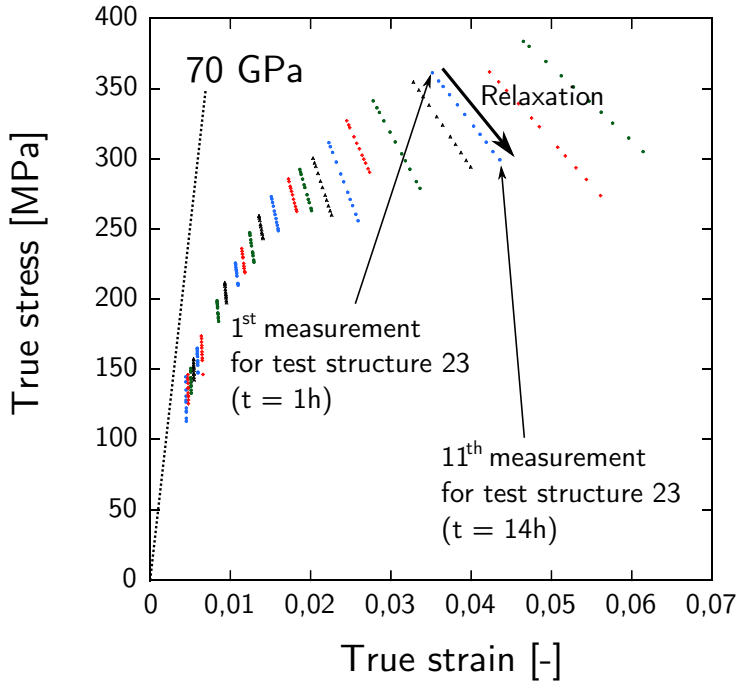

Figure 8.10: *True stress-true strain curve obtained from a "T10-6" set of structures of a* 205 nm*-thick AlSi film.*

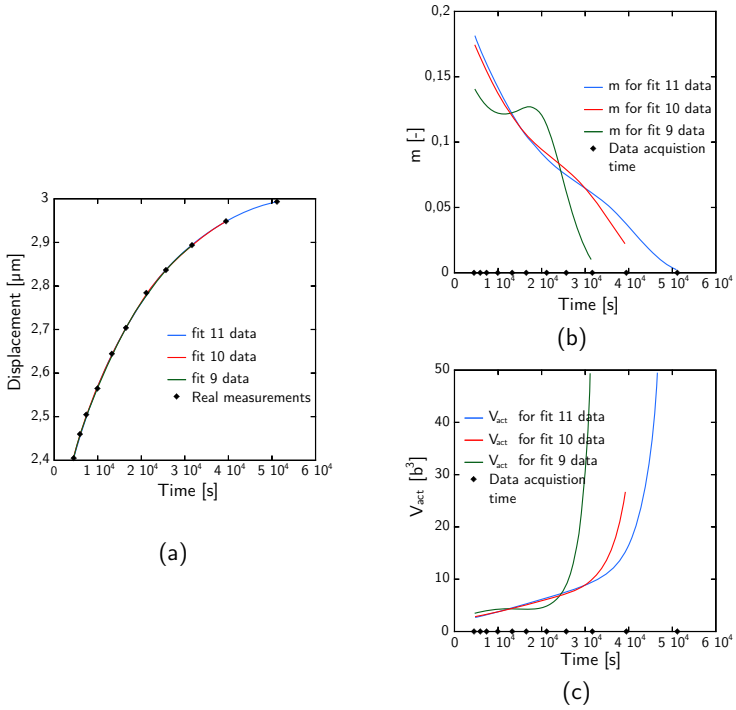

Figure 8.11: *Extraction of strain rate sensitivity parameters for the specific case of the "22 test structure": (a) fitting displacement versus time (b) variation of the rate sensitivity exponent as a function of time (c) variation of the activation volume as a a function of time.*

trated for a particular test structure in Fig. 8.11a. The resulting rate sensitivity exponent and activation volume are computed and plotted as a function of time for this particular test structure in Fig. 8.11b and Fig. 8.11c, respectively. Activation volumes are presented in units of b^3, b being the length of the Burgers vector (0.286 nm for Al).

Fig. 8.11 also illustrates the influence of the fit on the determination of m and V_{act}. In Fig. 8.11a, the fit is performed by considering the 9, 10 and 11 first measurements respectively. If the three different fits seem to match the measured data, the further derivations needed to extract m and V_{act} have a large influence on the final shape of the evolution of the rate sensitivity exponent (Fig. 8.11b) and the activation volume

(Fig. 8.11c) at long times. As a consequence, care should be taken when interpreting the data especially concerning the last measured data points and the real acquired data points (black diamonds in Fig. 8.11, Fig. 8.12 and Fig. 8.13) should always appear on the graph showing the evolution of the strain rate sensitivity parameters (m and V_{act}) with time, strain or stress. It must be noted that the high number of structures within one set should enable to discard the odd evolution of these parameters.

For the less deformed specimens (less than $\simeq 0.6\%$ initial plastic strain), m and V_{act} are not calculated due to the poor fit coming from the too small variation of the displacements between two times of data acquisition. The evolution of the rate sensitivity exponent and activation volume are shown in Fig. 8.12 and Fig. 8.13 for 4 specific test structures involving 0.6%, 0.9%, 1.6% and 3.1% plastic strain at $t = 1$h. The test structures have been selected to cover the whole initial plastic strain range from 0.6% to 3.1%. In the insert of Fig. 8.12 and Fig. 8.13 the data are presented for the whole time range measured. These two inserts illustrate the odd evolution of the strain rate sensitivity parameters with dramatic changes of slope for long times. As this is an artefact coming from the fitting procedure, the data in Fig. 8.12 and Fig. 8.13 have been limited to $t = 3\ 10^4$ s which corresponds approximately to the time of the ninth measurement.

The rate sensitivity exponent for a single test structure starts from an initial value around 0.15 and then decreases by a factor 2 to 4 as relaxation proceeds. Although this rate sensitivity is quite large compared to bulk large grain Al ($m \simeq 0.01$), the values lie in the same range as measured by Gianola et al. [49] on pure Al film with similar thickness. They had values obtained by strain rate jump experiments ranging 0.036 to 0.14. The initial deformation applied to the specimen seems to play a role on strain rate sensitivity with higher m extracted for the more deformed specimens.

In the following, the analysis is performed on the evolution of the activation volume in order to determine the mechanisms responsible for stress relaxation. It must be recalled that the activation volumes extracted in this work are normalised by the Taylor factor M. The real values of the activation volumes should be higher by a factor $\sqrt{3}$ to 3 [28]. Moreover,

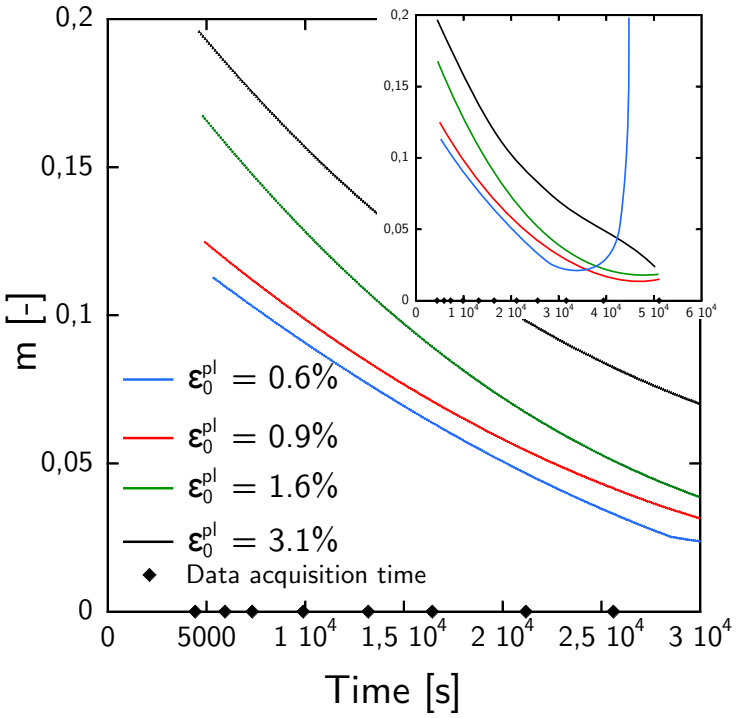

Figure 8.12: *Graph showing the evolution of the rate sensitivity exponent m as a function of time for 4 different test structures.* ε_{pl}^{0} *is the plastic strain in the beginning of the relaxation experiment.*

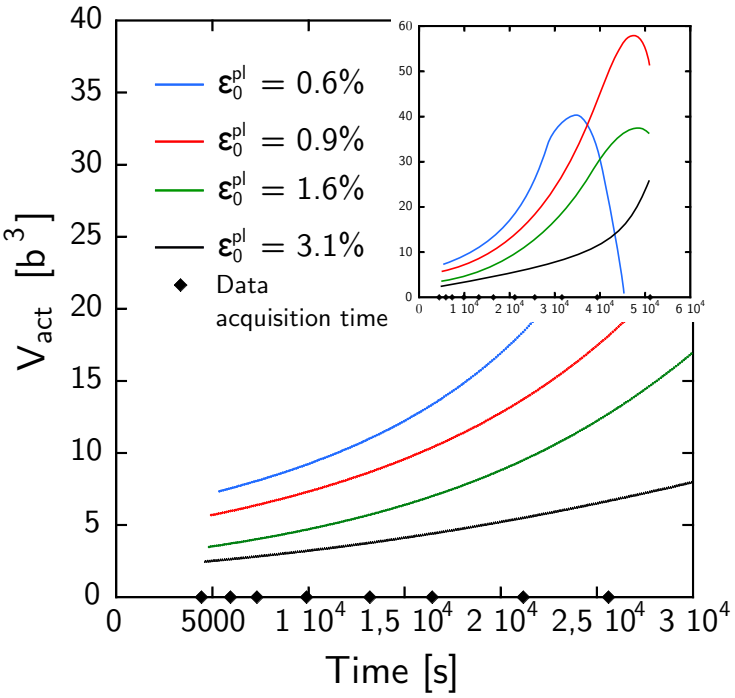

Figure 8.13: *Graph showing the evolution of the activation volume V_{act} as a function of time for 4 different test structures. ε_{pl}^0 is the plastic strain in the beginning of the relaxation experiment.*

the method proposed here is neither a pure relaxation test nor a pure creep test as both the stress and the strain vary during the test. Hence, the activation volume is characterised under evolving conditions, with possible microstructure changes such as a change of dislocation density, grain growth, etc.

Looking at Fig. 8.13, the initial activation volume does indeed depend on the level of predeformation, and on the relaxation time. The initial activation volume goes from $8b^3$ for small pre-deformation to $2b^3$ for the largest initial pre-deformation. These values are not small enough to reveal a diffusion mechanism. The evolution of activation volume with the pre-deformation is in agreement with the Cottrell-Stokes law[4] [8] [9]. This suggests that the activation volume is controlled by the interdislocation distance. From that perspective, a different initial dislocation density from one AlSi structure to another can explain the variation in the initial activation volume. The further evolution of the activation volume with time can still be assessed with dislocation-type mechanisms. Two events happen simultaneously as relaxation proceeds. First, dislocations nucleate from the grain boundaries. Due to the small grain size, the time necessary for a dislocation to spread the whole grain is expected to become smaller than the time necessary to nucleate the dislocation. Second, dislocations can be absorbed by grain boundaries or by free surfaces. Consequently, the number of dislocations within one grain will decrease as well as the interdistance between dislocation. This can explain the increase of the activation volume as relaxation proceeds. Although the measured activation volume give an idea of the thermally activated mechanism responsible for relaxation phenomena, the real mechanisms can only be confirmed by TEM observations. This has not been performed in the frame of this thesis. The only TEM observations made on the 205 nm-thick AlSi film were performed several weeks after the acquired relaxation data and revealed very few dislocations within the grains. Although, a low density of dislocations after large relaxation

[4] As explained in [28], the Cottrell-Stokes law tells that for tensile or compressive stress experiments $\partial\sigma/\partial \ln \dot{\varepsilon} \propto \sigma$. This law is usually followed in metals with grain size larger 1 µm. In the case of plasticity by dislocation-based mechanisms, it tells that the activation volume is proportional to the distance between forest dislocations (dislocations pinning points) which is inversely proportional to the flow stress.

is consistent with the proposed mechanisms, further TEM observations should be performed just after release of the test structures. An analysis of the evolution of the dislocation density with time could help to corroborate the proposed mechanisms.

A priori, the overall trends observed for the 205 nm-thick AlSi could be extended for higher relaxation times by performing additional displacement measurements on the test specimens. This would increase the accuracy on the fit of the displacement versus time relationship and would give access to more reliable data. Unfortunately, the sample was taken out of the SEM chamber after the last data acquisition (14 hours after release). This has led to a change at the surface of the sample due presumably to the change of the native oxide growth. As a consequence further displacement measurements did not match the first 11 data points in the sense that the displacement variation was no more monotonic. No fitting procedure could thus be performed.

The intrinsic limitations of the technique to extract the strain rate sensitivity parameters are the following. As no displacement measurement is possible prior to the drying of the structures, the behaviour of the material between the release of structures and the first SEM image, taking place about one hour later is not captured. This could be an issue for adapting the technique to testing of low melting temperature pure metals or thin film polymers. High rate relaxation phenomena cannot be captured and other techniques should be preferred for strain rate higher than typically 10^{-6} s^{-1}. Moreover, the SEM measurements do not allow continuous monitoring of all the test structures. This is not a major issue as long as enough data points are acquired and that the time of the measurements is precisely recorded. Again, following a very fast relaxation would require a completely different monitoring of the displacement evolution, for instance through instrumented capacitive measurements, but this would very much complicate the fabrication process.

Another limitation comes from the unknown initial strain rate applied during the first loading step. When a test structure is released, the specimen beam is subjected to a force equal to the internal stress in the actuator material times the cross-sectional area of the actuator beam. The strain rate at that time depends on the time required by the struc-

ture to reach an equilibrium point. This strain rate is probably quite high and could influence the behaviour of very strain sensitive materials. Now, the first measurement after relaxation is performed at a time when the rate dependency during the transient corresponding to the first loading is probably not playing a role anymore. The use of a tapered actuator beam could be a way to control the rate of loading if the etch rate is known.

The main advantage of the use of self actuated micro-tensile stage to perform relaxation experiments lies in that all test structures (i.e. specimens and actuators) are built on-chip. No external device, such as nanoindenter or tensometer testing platform, is thus needed. Monopolization of equipment for long period of time can be cumbersome if experiments must be conducted for days and months considering that only one specimen can be tested at a time. Strain rate lower than 10^{-6} s^{-1} can thus be investigated which has not yet been reported in the literature for thin freestanding film specimens. The high number of testing structures provides statistically representative results probing the effect of the initial deformed microstructure on the time dependent response of the specimen material.

Chapter 9

Testing of pure aluminium thin films

9.1 Materials and experimental procedures

All Al films discussed in this chapter were deposited by electron beam evaporation. The reactor used for evaporation is similar to the one depicted in Fig. 5.5 in Section 5.4. The Al target is made of 99.999% pure Al pellets. The chamber pressure prior to deposition is equal to 7.10^{-7} mbar which is the lowest pressure that the vacuum system can reach. Twelve substrates can be deposited at the same time. The substrates are not heated but a small rise of the temperature is expected at the substrate level as the electron bombardment at the source level heat up the Al atoms. The temperature is not measured but should not be higher than 100 °C in the case of Al deposition. The deposition rate is fixed to 0.3 $Å s^{-1}$. The only parameter varying from one deposition to another is the duration of the deposition process which allows monitoring the thickness of the film.

For each process involving pure Al test structures, one blanket wafer is added at the metallisation step. After Al deposition, this blanket wafer is used for internal stress measurement by wafer curvature (see Section 6.5). The processed wafers are patterned using positive litho-

graphy (Fig. 5.4) and plasma etching as already stated in Section 5.4. Films tested with test structures had a thickness ranging from 100 nm to 500 nm

9.2 Stress relaxation

The internal stress in all Al deposits was found to be zero within the limits of accuracy of the Stoney measurement method. This was indicated by the absence of wafer curvature change on the blanket wafer. It was confirmed on the released rotating sensors from the patterned wafers as no deflection occurred. Concerning the analysis of the micromachines and as already stated in the introduction of part III, no consistent stress-strain curve could be extracted from micromachines on pure Al films. No matter the thickness of the film, unexpected fast relaxation occurred in all specimens. For all structures, the displacement measurement (u) was very close to the displacement that would have occurred if the actuator was free to contract (u_{free}). The situation is depicted in the force-displacement diagram of Fig. 9.1.

The equilibrium position defined in Section 4.2 is not known and a relaxation analysis between this equilibrium point and the first measured point, like in Section 8.3, cannot be performed. The difference lies in the fact that no further relaxation was observed up to that first measurement even several days after release. It means that all the relaxation process occurs in less than an hour after actuation no matter the initial stress in the specimen beam. It is not known whether this fast relaxation occurs only in freestanding pure Al films as the zero internal stress measured on the blanket wafer (not freestanding) could also be a consequence of the fast relaxation. The fast relaxation is certainly linked to the purity of the Al as only small amount of impurities have already proven to considerably lower the steady-state creep rate of Al [71].

To confirm that relaxation phenomena are indeed occurring in Al at a faster rate than in AlSi, creep measurements were performed by nanoindentation on the the two film materials. The pure Al film was 500 nm-

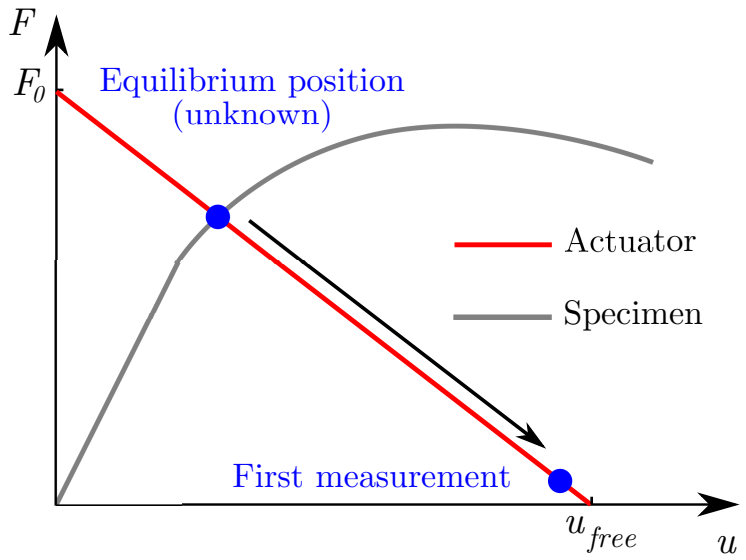

Figure 9.1: *Force-displacement diagram in the case of pure Al testing. The equilibrium position reached just after release is not known. The first measurement which can be performed is near the fully relaxed position ($u = u_{free}$, $F = 0$).*

thick whereas the AlSi film was 205 nm-thick[1]. Each test is performed as follows:

- The tip is brought into contact with the film thickness and the load is increased at constant load rate (0.01 mN/s) from 0 to the maximum load F_{max}.
- The load is maintained to its maximum value for a constant time t and the displacement is recorded.
- The load is decreased at constant load rate (0.01 mN/s) from the maximum load to 0.

[1]It would be preferable to compare films with the same thickness but these experiments were performed on available samples and aimed only are capturing the kinetic difference between the relaxation process of the two materials.

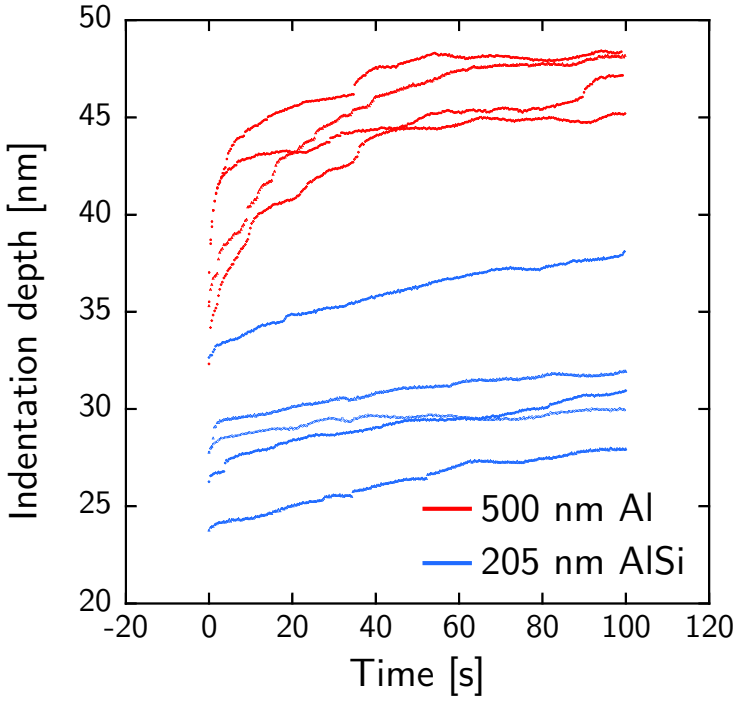

Figure 9.2: *Evolution of the indentation depth as a function of time for an applied force of* 0.06 mN *for a* 500 nm*-thick pure Al film and a* 205 nm*-thick AlSi film.*

The different values for the maximum load are equal to 0.02 mN, 0.03 mN, 0.06 mN and 0.1 mN. The highest load corresponds to indentation depth in the range of 60 nm and 30 nm for Al and AlSi, respectively. This is around 10% of the indentation depth which should not be affected by the presence of the substrate in this case of a soft material on a hard substrate. Each indentation is performed 6 times. Differences in the measured displacement for indentations performed with the same parameters can arise due to the roughness of the film. However, as we are interested in the kinetic of relaxation phenomena, only the constant load part of the test is considered. Indentions data with too large thermal drift are discarded.

Fig. 9.2 compares the unloading part of the test for the two films with

the following parameters: $F_{max} = 0.06\,\mathrm{mN}$ and $t = 100\,\mathrm{s}$. The force was observed to decrease slightly as the displacement increases during the relaxation experiment. This is due to the indentation method but as a first approximation, the force level can be considered to be constant. The fact that the displacement evolves with time for a constant force for both materials reveals a creep/relaxation behaviour. Similar experiments on fused silica do not show any time dependent response. Moreover, the increase in displacement is clearly larger in the case of pure Al indicating that the relaxation is faster when Al is not alloyed.

The fast relaxation processes occurring in pure Al films makes the concept of internal stress actuated micro-tensile stages not suitable for extraction of the static hardening properties.

9.3 Ductility of Al thin films

9.3.1 Imperfection-sensitive ductility of Al thin films[2]

Besides the fast relaxation, the large ductility observed for the pure Al specimens sometimes larger than 30% associated to a large scatter was quite a surprise, pushing for an in-depth analysis. Ductility is the capacity for a material to deform without cracking [24]. Two main mechanisms limit the ductility of metals:

- The first is the occurrence of plastic localisation by geometric necking or material instability. The strain corresponding to the onset of plastic localisation is denoted as ε_u throughout this text. Note that ε_u depends on the loading conditions (e.g. uniaxial tension, biaxial tension, shear, etc.) and is thus not an intrinsic material property.
- The second mechanism is the accumulation of damage by nucleation, growth and coalescence of microvoids or microcracks. The strain corresponding to the complete failure of a material element

[2]This section is mainly derived from the paper Coulombier et al., Scr. Mater. 2010, 62, 742 [16].

is noted ε_f and, as for ε_u, it is not an intrinsic material property, but depends on the loading conditions.

In the following, the term "ductility" is defined as the strain corresponding to the onset of necking, which is often smaller than the true fracture strain.

Ductility in thin metallic films is known to be weaker than in the bulk counterpart and even in the case of Al, the ductility hardly reaches a few percent [60] [36]. In thin films, the small grain size and the dominant presence of the surfaces are expected to play a major role. Indeed, some or even most of the dislocations can escape from the film (depending on the morphology and number of grains over the thickness, and on the presence of a possible surface oxide layer), thus limiting the strain-hardening capacity. Furthermore, it is important to remember that imperfections significantly affect the ductility of plastically deforming solids [69] and that the magnitude of typical imperfections can be expected to be larger in thin films compared to macroscopic samples. However, large ductility has been encountered in thin metallic films like Al when it was associated to grain growth mechanisms [48] (see Section 3.2).

In this section, the pure Al micromachines are analysed in terms of their resistance to plastic localisation. The study focusses on two films thicknesses: 200 nm and 375 nm. The analysis focusses primarily on the observed wide scatter in the ductility, which is dependent on the specimen size and thickness, a topic which has not received any attention in the literature to date.

First, it is important to recall that the dimensions (lengths and widths) of specimens are varied all over the wafer (See Section 4.4.6). Within one set of structures (same width ratio between specimen and actuator beam), the overall length of the two-beams structure is kept constant while the lengths of the two beams are varied to generate different states of stress. Some sets of structures have exactly the same geometric dimensions except from the overall length[3], providing equally deformed

[3]This is true for generation 3 and 4 set of masks from which all the data of this section are extracted.

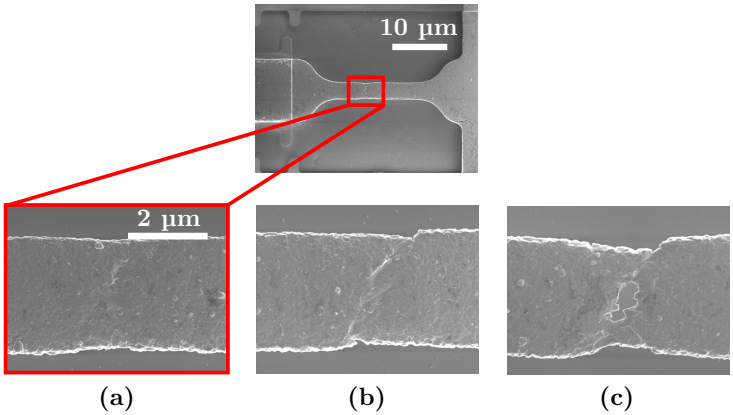

Figure 9.3: *Plastic localisation evolution observed in consecutive specimens with different strains involving (a) diffuse necking, (b) localised shear band process and (c) damage up to final failure.*

structures but with varying length. The resulting high number of testing structures allows to analyse the impact of the geometrical dimensions on the ductility of the tested material.

For the two considered thicknesses, plastic localisation is observed in specimens deformed to sufficiently large strains. When plastic localisation sets in, the extra overall displacement required to reach failure is small. Hence, due to the discrete nature of the test technique, specimens most often either fail or deform uniformly. Nevertheless, specimens with necking can sometimes be observed, such as in Fig. 9.3 for 200 nm-thick, 4 µm-wide Al specimens. Fig. 9.3a shows a diffuse necking process over a length scaling with the specimen width. At larger strains, a more localised necking mechanism develops that resembles a shear band oriented at about 55° from the main loading direction (see Fig. 9.3b and c). Finally, Fig. 9.3c shows that damage develops within the shear band, leading to final fracture.

A qualitative observation of the test structures shows that the ductility is subjected to wide variations. For instance, in a series of specimens, one failed specimen followed by one non-failed specimen is sometimes observed, even though the latter involves a larger strain. Furthermore,

a series of shorter test structures systematically show larger ductility compared to longer test structures. In order to rationalise these observations, Fig. 9.4 gathers the strain experienced by each tensile stage as a function of the specimen surface area for thicknesses equal to (a) 200 nm and (b) 375 nm, respectively. The failed specimens are indicated with open symbols. In order to provide an accurate estimate of the strain that was applied to the failed specimens, it was assumed that the applied stress is equal to the stress experienced by the first non-failed specimen located in the same set of structures. The displacement of the failed specimen as if no fracture had occurred is then obtained using Eq. 4.7 which was derived in Section 4.2 and which links the measured displacement to the stress experienced by the specimen beam. In some structures, fracture occurs at the overlap between the actuator and the specimen due to the local stress concentration and not in the gauge section of the dogbone specimen. Those samples are discarded. Finally, for some specimens, fracture is not caused by the deformation imposed by the actuator but is due to processing problems, such as a defect in the photoresist or dust particle on the wafer. In such instances, the failed samples are also not taken into account.

In order to analyse more quantitatively the effect of the specimen size on the ductility, the data of Fig. 9.4 are converted in the form of a probability graph, as shown in Fig. 9.5a. Because the technique involves a wide range of sample sizes and imposed strains, the data are grouped in different intervals of surface area and strain. For each interval, the probability of failure is calculated as the number of failed samples divided by the total number of samples within the same interval.

Fig. 9.5b and Fig. 9.5c show a statistical behaviour similar to the one observed for brittle materials, usually rationalised using Weibull-type analysis [85]. A maximum strain value is observed beyond which fracture occurs for all specimens. The maximum values are about 0.08 and 0.27 for the smallest specimens, made of 200 nm and 375 nm thick films, respectively.

The distribution of ductility shown in Fig. 9.5 can be analysed by considering the effect of the presence of imperfections within the specimens. Imperfections are inherent to the fabrication process as a result of local

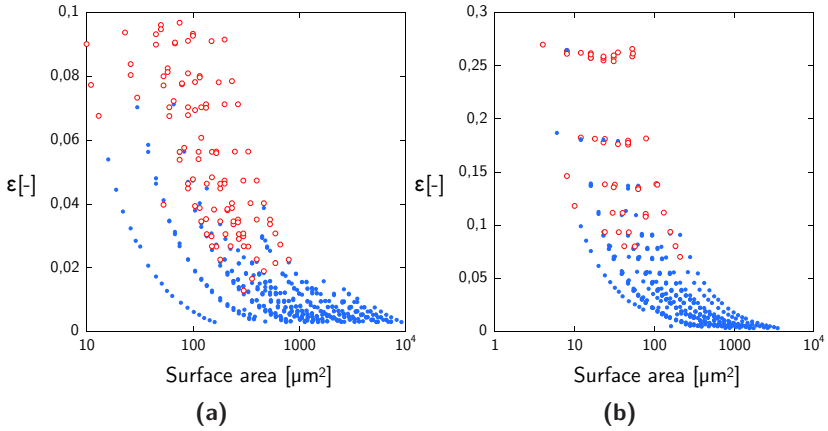

Figure 9.4: *Strain as a function of the specimen surface area for (a)* 200 nm*-thick and (b)* 375 nm*-thick Al specimens. Open symbols indicate failed specimens, filled symbols indicate non-failed specimens.*

thickness reduction due to the natural roughness, heterogeneities in the etching process or grain boundary grooving, or local width reduction due to the definition of the photoresist or material imperfection (e.g. a cluster of grains with weak orientations; see [44]). There is an increasing probability of producing larger imperfections when the surface area increases, as well as when the thickness decreases. The effect of imperfection on necking has been addressed by Hutchinson and Neale [69], who demonstrated that plastic localisation is triggered earlier in the presence of imperfections. Recent computational studies based on strain gradient plasticity theory have addressed the same issue, showing that strain gradient effects can delay the necking process in micron-sized samples [95].

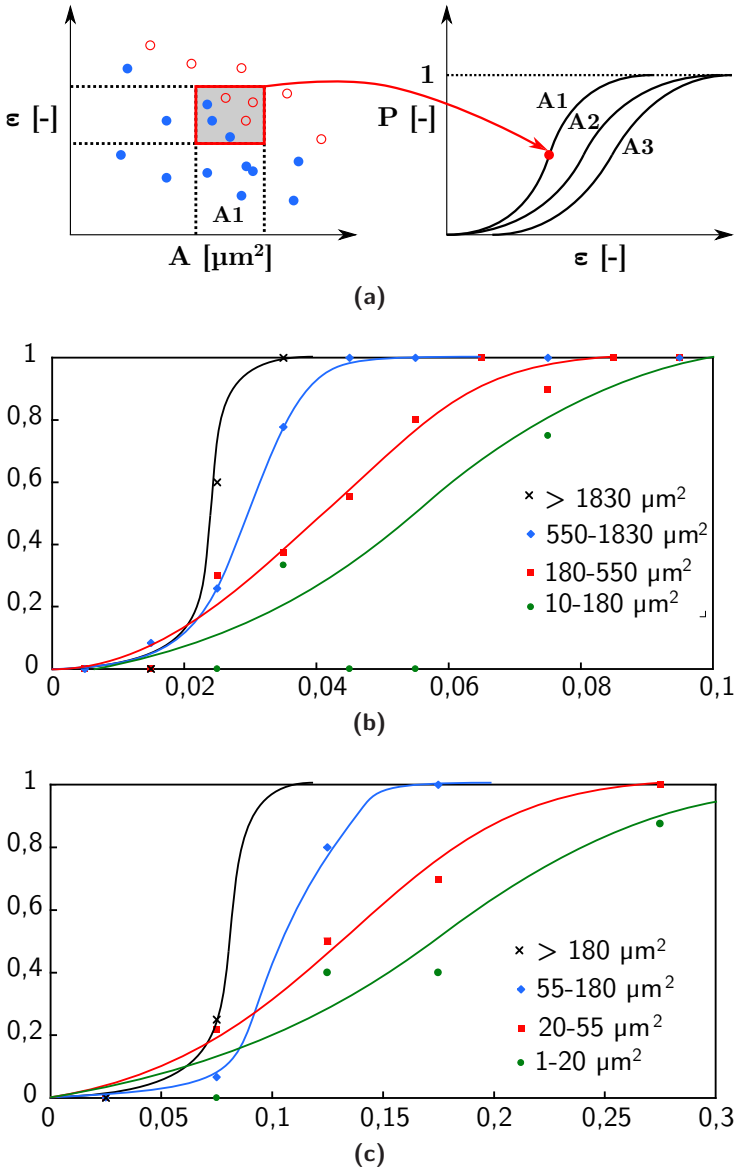

Figure 9.5: *(a) Methodology for converting a "strain–surface" plot into a "probability of failure" graph; (b) probability of failure for the* 200 nm*-thick and (c) for the* 375 nm*-thick Al film. Lines are plotted as a guide for the eye.*

9.3.2 Modelling size effects in thin film[4]

The presence of imperfections is not the only cause of the size effect on the ductility of Al thin films. The high density of interfaces and the large surface-to-volume ratio which are inherent to thin films are known to affect strength and ductility. In thin films, interfaces consist in grain boundaries, interfaces between film and substrate and possible oxide layer at the surface. They all act as barriers to dislocation motion and multiple mechanisms between dislocations and interfaces can arise: blocking, annihilation, emission, reflection, transmission. The density of dislocations barriers is thus related to both grain size and sample thickness. A simple model based on empirical data was proposed by Venkatraman and Bravman [129] to account for the influence of these two parameters on the strength of AlCu(0.5%) films. This model was already given in Section 3.2.

Description of the model

As other parameters than grain size and sample thickness can have a first-order impact on ductility and strength, a finite-element model has been developed relying on a finite-strain implementation of the strain gradient plasticity theory developed by Fleck and Hutchinson [40] for the behaviour of the grain interior. Cohesive zones are used to represent the interface layers, together with evolving higher-order boundary conditions at the frontier with the grain interior (Fig. 9.6). The interface layers are extremely thin, of the order of a few atomic spacings, depending on the type of interface considered (grain boundary, interface with an oxide layer, interphase) with a structure, and thus a response, different from that of the grain interior. The interface layers are considered to be initially impenetrable to dislocations. This is enforced by constraining the plastic strain rate at the interfaces between the grain

[4]This section is mainly derived from the work of Charles Brugger who has spent two years in UCL as a post doc, collaborating with me, to develop the modelling aspects aiming at understanding the size effects in thin films. The main results of his work were published in the following paper: Brugger et al., Acta Mater 2010, 58, 4940 [10].

interior and the layer ($\dot{\varepsilon}_p = 0$). When applying the load, the grain interior starts deforming plastically while the interface layers remain elastic. The strength of the near-interface regions increases rapidly due to the large local plastic strain gradients resulting from the higher-order boundary conditions, generating also large back-stress levels within the grain interior. When the stress on an interface reaches a critical value, the different mechanisms of transmission, nucleation and/or sinking of dislocations start being activated. This is empirically modelled by relaxing the constraint on both sides of the interface layer, and letting the plastic flow develop within it. The back-stress then also partially relaxes. From that point on, the confinement is not explicitly enforced through the higher-order effect, and the plastic flow is only controlled by the classical behaviour of the interface layer represented by a simple linear hardening law. The slope of the classical hardening law of the interface layer phenomenologically represents the resistance to dislocation motion imposed by the mechanisms occurring inside the interface layer and the evolving structure of the interface.

The thin films are modelled using plane-strain conditions. A ribbon of 20 rectangular grains is simulated. Necking is simulated by adding an imperfection η in the central grain making boundary conditions no longer periodic. The imperfection consists of a smaller initial flow stress equal to $(1-\eta)\sigma_0$, where σ_0 is the initial flow stress of the other grains. The inputs of the model are the following:

- the Young's modulus E and Poisson ratio ν for the bulk material elastic behaviour;
- a Voce law [79] characterised by σ_0, Θ_0 and β_0 for the plastic behaviour;
- the internal length l_* of the strain gradient plasticity model;
- the interface relaxation stress σ_{IRS} and effective hardening h_I for the behaviour of the the interface layer;
- n for the number of constrained surfaces which is 0 (freestanding film), 1 or 2.

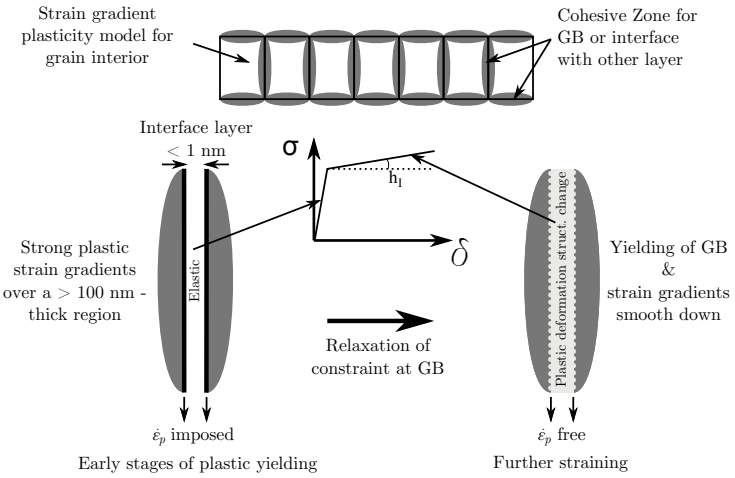

Figure 9.6: *Schematic description of the 2-D plane-strain model for the polycrystalline thin film based on a strain gradient plasticity description of the grain interior and cohesive zone representation of the interface layers (grain boundaries and interfaces with other layers) involving, on both sides, evolving higher-order boundary conditions.*

For all the different simulations performed, the parameters describing the grain interior are kept constant: $E/\sigma_0 = 1167$, $\nu = 0.3$, $\Theta_0/\sigma_0 = 9$, $\beta_0 = 13.5$. These parameters are taken from [117] and are representative of pure Al. The other parameters are varied around a master case to see their influence on the ductility and strength of thin Al films. The master case corresponds to $h/l_* = 1$, $d/l_* = h/l_*$, $\eta = 1\%$ and no constrained surfaces ($n = 0$). In the master case, interfaces are considered to be impenetrable (σ_{IRS}/σ_0 set to a very high value).

Effect of the thickness

Fig. 9.7a presents the influence of the normalised thickness h/l_* on the normalised engineering stress–strain curves for homogeneous or polycrystalline freestanding thin films with no constrained surface. The thickness can have two opposite effects on the ductility depending on the presence or not of grain boundaries. In homogeneous films, the thinner the film, the larger the magnitude of the plastic strain gradients, hence the ductility. Plastic strain gradients tend to stabilise plastic localisation by providing additional strengthening to the region where necking initiates. This effect has been discussed by Niordson and Tvergaard [95].

In polycrystalline films, the ductility decreases with decreasing thickness. This drop in ductility associated with the size-induced strengthening has already been reported experimentally in Al [56] as well as in other materials [36] [120]. This decrease in the ductility is captured by the model, though there is no dramatic drop. Now, allowing for grain boundary relaxation through decreasing the associated stress σ_{IRS} leads to a more significant loss of ductility, as shown in Fig. 9.7b, where the uniform strain of freestanding polycrystalline thin films is plotted as a function of the inverse of the normalised thickness l_*/h for $\sigma_{IRS}/\sigma_0 = \infty$ or 4. The relaxation of the higher-order boundary conditions has thus an impact on the loss of ductility for very thin films.

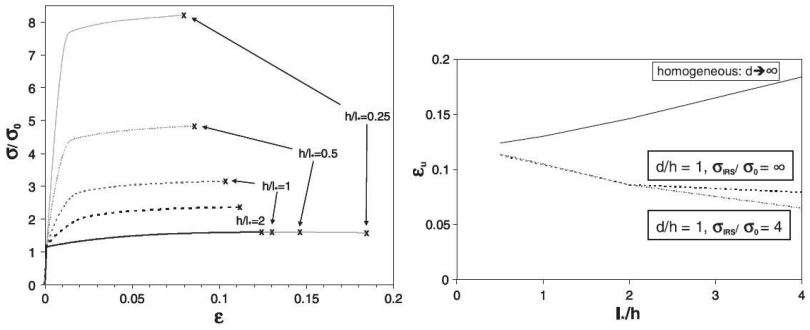

Figure 9.7: *Effect of the normalised thickness h/l_* on (a) the normalised engineering stress–strain curve and (b) on the uniform elongation for homogeneous (continuous lines) or polycrystalline (dotted lines) freestanding films with or without grain boundary relaxation.*

Effect of imperfections

Imperfections can also alter significantly the ductility [69], at least in the case of bulk materials. However, the imperfection sensitivity is not expected to be as large in thin films materials due to strain gradient effects. Fig. 9.8 presents the variation of the normalised uniform elongation $\varepsilon_u/\varepsilon_u^{\eta\to 0}$ as a function of the imperfection η, allowing or not for grain boundary relaxation, i.e. $\sigma_{IRS}/\sigma_0 = \infty$ or 4. Very limited imperfection sensitivity is predicted without grain boundary relaxation: a 10% imperfection leads to less than 20% loss of ductility. With relaxation of the grain boundary confinement, a much larger decrease by 50% of the ductility is predicted by the model. The loss of ductility depends thus heavily on the grain boundary relaxation σ_{IRS}/σ_0. A limited value for σ_{IRS} should be used in the model as imperfections were shown to have a large impact on the ductility observed for the two pure Al films thicknesses of Section 9.3. Thin films are indeed more prone to imperfections than their bulk counterpart because of the roughness, grain boundary grooving or the columnar grain structure.

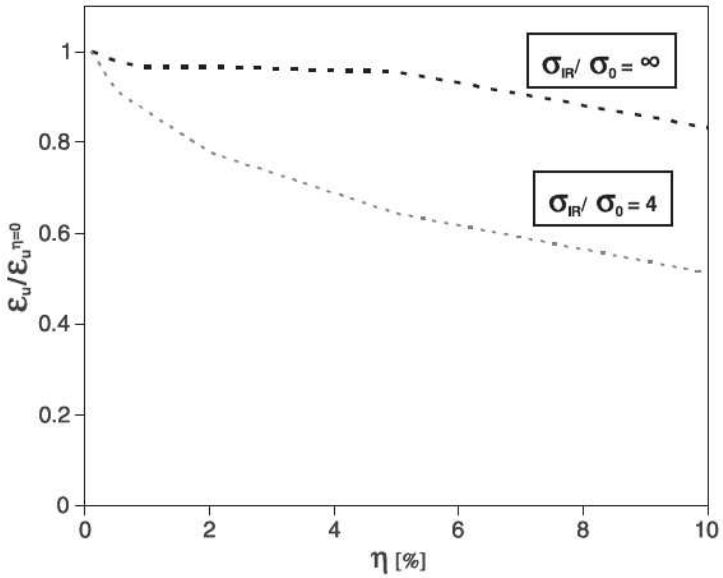

Figure 9.8: *Variation of the normalised uniform elongation as a function of the imperfection size for polycrystalline freestanding films with or without grain boundary relaxation.*

Effect of the grain size distribution

In all the aforementioned simulations, the film is modelled as a ribbon of 20 grains with identical grain size d. The influence of the grain size distribution is performed by considering 10 different normal grain size distributions with a mean value of $d = l_*$ and a standard deviation $\Delta d = 0.2 l_*$. Fig. 9.9 compares the normalised engineering stress-strain curves for these 10 cases to the master case involving a single grain size and no imperfection ($\eta = 0$). The master case gives an upper bound on the strength and on the ductility. Accounting for a grain size distribution induces a slight decrease in the strength and a noticeable loss of ductility. The smallest stress was observed for the distribution involving the largest grain: the uniform strain and corresponding stress are about 60% and 10% lower than the master case, respectively. The largest grain has a major impact on the behaviour. It sets the maximum level of strengthening as the yield stress is known to be smaller for larger grains. A large grain acts thus as an imperfection which affects the ductility. However, the 2-D ribbon model artificially amplifies grain distribution effects, as the imperfection is affecting the entire width, which is not the case in the reality of the Al film tested in this work. Even though the 2-D model exaggerates this effect, it reveals the importance of the grain size distribution in the range of sizes ($d < 1\,\mu$m) where the strength is significantly affected by small changes in the dimensions of the microstructure. The grain size distribution is thus a primary source of imperfections controlling the resistance to necking.

Modelling versus experiments on pure Al

The link between the model used by Brugger and the results of Section 9.3.1 on the ductility of pure Al can only be qualitative. Indeed, the significant creep contribution indicates a large rate sensitivity which is not taken into account in the model. However, the parameters considered in the previous section certainly play a role on the ductility of Al. Strain gradients effects have been shown to stabilise the necking process which is confirmed by the observation of pure Al deformed specimens Fig. 9.3 in which diffuse necking is observed. The loss of ductility with

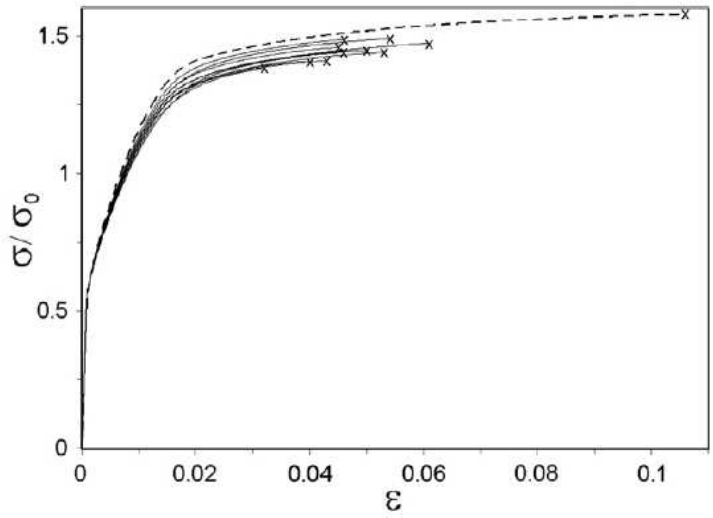

Figure 9.9: *Effect of 10 different grain size distributions (continuous lines) on the normalised engineering stress–strain curve compared to the master case with single grain size (dashed line).*

larger imperfections predicted by the model is also in agreement with the results on the two pure Al films tested in Section 9.3.1. In addition to these two contributions, the rate sensitivity is probably the main reason explaining the high ductility of pure Al films. The strain rate sensitivity is indeed known to very much increase the resistance to necking [69]. Generally, the ductility of thin film materials hardly reaches a few percents. In the case of pure Al films and in the absence of imperfections (small specimen), ductility as high as 30% was detected. This underlines the need to take rate sensitivity effects into account in the model to capture such high strain before necking.

9.4 Fracture of Al thin films[5]

In Section 9.3, the ductility of Al thin films was analysed in terms of their resistance to plastic localisation. In this section the focus is put on the second mechanism limiting the ductility of metals: damage and fracture mechanisms. For this purpose, the notched specimen geometry described in Section 7.1 is considered. These specimens are better suited than uniaxial tension specimens to characterise fracture by allowing a stable deformation process without the occurrence of necking. Fig. 9.10 show micrographs of 210 nm-thick Al notched specimens corresponding to different amounts of deformation. Cracking is found to initiate at the notch root (Fig. 9.10a) and then propagates by coalescence of voids (Fig. 9.10b and Fig. 9.10c). The void spacing seems to scale with the grain size. Fig. 9.10d shows a TEM micrograph of a void present in the necking region of one of the highly deformed uniaxial specimen. The TEM sample was obtained after FIB cutting and micromanipulation. The void is located at a grain boundary in agreement with observations made by Kumar et al. [81] on electrodeposited nanocrystalline Ni showing void nucleation at triple junctions. Fracture of Al films seems thus to be intergranular rather than intragranular and from Fig. 9.10 looks similar to what is observed on macroscopic samples.

As notched specimens involve non-homogeneous deformation, numerical analysis is needed to extract quantitative information about the stress and strain field in the specimen. For that purpose, 3-D finite element (FE) simulations have been performed using the general purpose FE software Abaqus, within a finite strain set-up [3]. Highly refined meshes were used in the near notch tip region. The constitutive model is the J2 flow theory and the hardening law corresponds to a 250 nm-thick Al film as measured in [37]. This hardening law was extracted from a set of micromachines before realising the fast stress relaxation phenomena occurring in pure Al films (Section 9.2). Moreover, the classical plasticity

[5]This section is derived from the analysis of notched specimens. The FE simulations were performed by Thomas Gets during his master thesis which I partly co-supervised (academic year 2006-2007) and the results have been discussed in [3], [17] and [101].

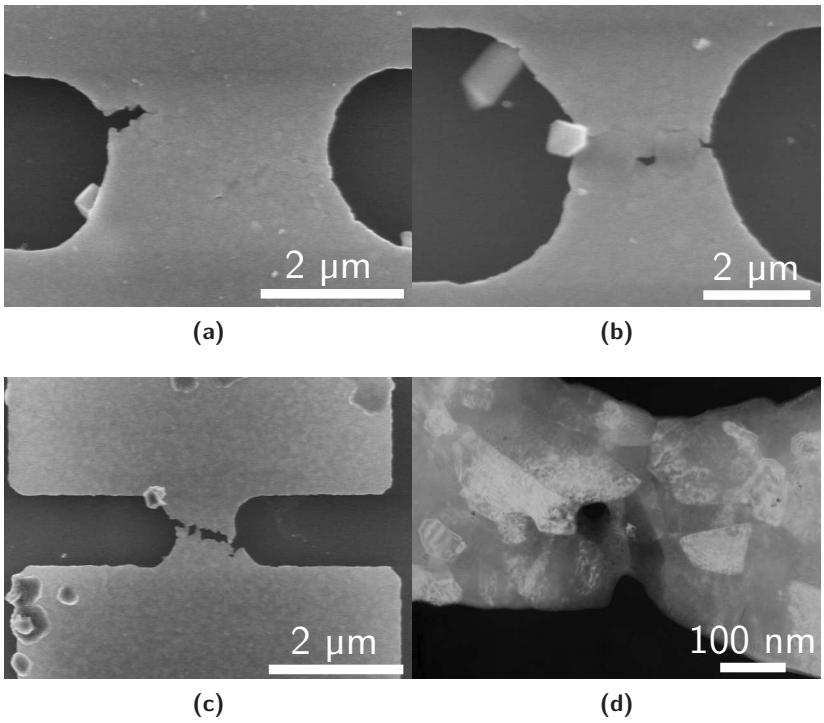

Figure 9.10: *Damage by void growth and coalescence in* 210 nm*-thick Al films; (a) to (c) micrographs of three notched specimens deformed up to different levels of deformation; (d) TEM micrograph showing a cavity growing along a grain boundary in a necking zone of a tensile test specimen.*

theory used here does not take into account any strain gradient effect or viscoplastic behaviour. As a consequence, the analysis performed with the FE element simulations do not correspond to the real behaviour of pure Al. Though, the procedure is qualitatively correct and the outputs from the simulations should be considered as qualitative data.

The results of the simulations were compared to the experimental results by matching the experimental and predicted notch opening as shown in Fig. 9.11. The fracture strain ε_f is defined as the equivalent plastic strain at the onset of cracking near the notch root. This comparison was performed for different geometries of the notched specimens. The fracture strain of the different geometries is reported as a function of the ratio L/R in Fig. 9.12, L and R being the length of the ligament and the radius of curvature of the notch, respectively. The fracture strain as well as the scatter on the fracture strain increase with increasing L/R ratio. No dependence of the fracture strain on the film thickness is observed (though the number of data is too small relative to the scatter to ascertain definitive conclusions). The increase of ε_f with decreasing R probably originates from a grain size effect. As voids nucleate at grain boundaries perpendicular to the main loading direction [81], when decreasing the notch radius, the probability of finding a well oriented grain boundary in the large strain zone near the notch root decreases, leading to larger ε_f, but also larger scattering.

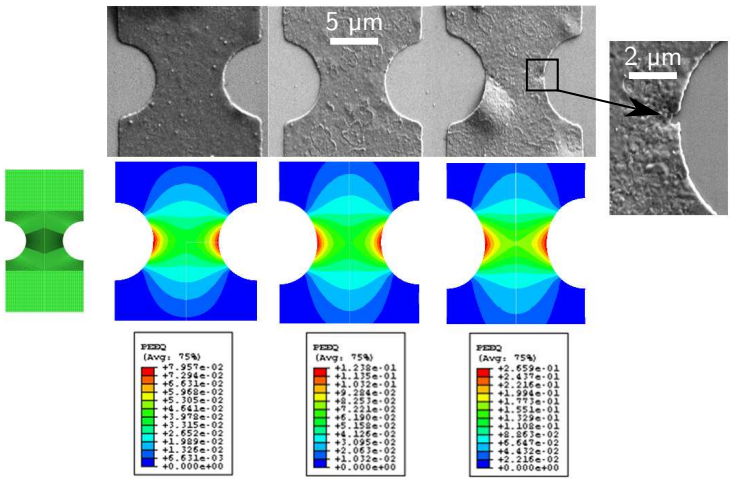

Figure 9.11: *Comparison between micrographs and FE predictions of deformed notched specimens, the third one corresponding to cracking initiation.*

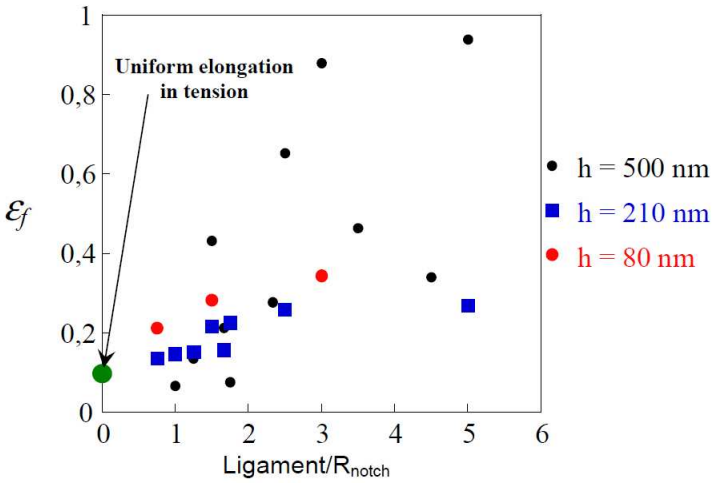

Figure 9.12: *Variation of the fracture strain of Al notched samples of 3 different thicknesses as a function of the ratio of the length of the ligament (L) divided by the radius of the notch R.*

Chapter 10

Conclusion and perspectives

In this thesis, a novel experimental method has been proposed to extract the mechanical properties of thin film materials. It is an on-chip technique which relies, as an actuation mean, on the internal stress generated during deposition. Apart from the particular actuation principle, an original feature lies in the high number of test structures generated at the same time instead of relying on a complex multipurpose testing stage.

The mechanics ruling a single test structure as well as the design requirements needed to produce valid measurements were described in Chapter 4.

All the aspects of the fabrication process were detailed in Chapter 5. The properties that each layer should meet were described and a solution was proposed for the specific testing of Al and AlSi films.

Then, Chapter 6 described the different structures (rotating sensors, single material auto-actuated test structures) and techniques (wafer curvature, ellipsometry, nanoindentation) needed to extract the parameters needed in the data reduction scheme following the idea of creating a versatile on-chip mechanical testing laboratory.

Chapter 7 pushed forward the potential of the technique by proposing different geometries (notched specimens) as well as the adaptation of the

fabrication process to enable TEM observation of the deformed structures.

In Chapter 8, the new concept was used to extract the stress-strain curves of AlSi(1%) sputtered films. This study proved the ability of the technique to extract the mechanical properties of ductile materials. In addition, the relaxation behaviour was measured and analysed for strain rate smaller than 10^{-6} s^{-1}. A methodology was proposed for the extraction of the strain rate sensitivity parameters of the tested material.

The study of the evaporated pure Al films was discussed in Chapter 9. The novel tool showed its limitations as the too fast relaxation mechanisms in pure Al did not allow to extract any stress-strain response. Nevertheless, the ductility was analysed for these pure Al films and was found to be strongly dependent on the presence of imperfections. Besides the imperfection sensitivity, values of the necking strain as high as 30% were measured where usual thin film materials hardly reach a few percents. A finite-element model relying on a finite-strain implementation of the Fleck–Hutchinson strain gradient plasticity theory captured the trends observed on the ductility of pure Al films. Although the model did not take into account any viscoplastic effect, the high ductility was in agreement with the fast relaxation of the pure Al films. Finally, a qualitative analysis of notched specimens revealed that the fracture of pure Al occurred by void growth and coalescence similarly to what is usually observed on macroscopic samples.

Application of the on-chip technique to the study of Al and AlSi films has shown its limitations essentially through two aspects. The first one is that the data acquisition is not performed in situ during tensile testing. Indeed, just after actuation by etching of the sacrificial layer, the samples have to be rinsed and dried and the measurement are performed in a SEM, test structure after test structure. As a consequence, in the case of a time dependent response, the early behaviour of the material cannot be captured. The other limiting factor is the fact that the strain rate applied to the test structures is not controlled. Moreover, as the structures are released at the same time, the strain rate is different for each structure. This is a problem for very strain rate sensitive materials as their stress-strain behaviour depends on the applied strain rate. From

that point of view the two materials tested in this thesis are certainly not the best materials suitable for mechanical testing by the on-chip technique. However, they allowed to identify these weak points and further developments of the technique should aim at enabling direct measurement of the displacement. For instance, controlling the rate of loading during the release is not too difficult if use is made of tapered actuator beams.

Despite these limitations, the lab on-chip technique presents many advantages with respect to already existing techniques. The fabrication process is very simple and involves techniques which are standard in facilities dedicated to microfabrication. The fact that both specimens and actuators are created during the fabrication process avoids the handling issues which occur in the case of loading by an external device. High throughput statistical data can be generated and different loading conditions can be envisaged. The technique is not limited to the testing of Al films as the standard fabrication process already proved to be suitable for mechanical testing of other thin film materials such as monocrystalline silicon, polysilicon and palladium. Moreover, the addition of one step in the fabrication process (back etching of the substrate) is sufficient to allow TEM investigation of the deformed specimens. It must be reminded that the lab on-chip concept is not just limited to the testing of materials deposited in UCL. Indeed, the technology has already been transferred to industrial deposits by sending pre-patterned wafers. The user then performs the film deposition from which the mechanical properties must be extracted. The wafers are then brought back to UCL for lift-off (patterning of the specimen material), etching of the sacrificial layer and measurements.

Concerning the perspectives of the present work, two aspects must be considered: the evolution of the lab-on chip concept and the understanding of the behaviour of the investigated film materials. The further developments of the concept should focus on the following guidelines:

- Find the best couple sacrificial layer/etchant so as to dispose of a generic process which gives a maximum etching selectivity for any kind of tested material.

- Modify the design of the actuators so as to control the strain rate applied to the specimens, see above.
- Measure the displacement imposed to the specimens by means of an electrical measurement.
- Define the best design requirements to extract valid measurements for other testing configuration.

In terms of material properties and investigation of deformation and failure properties, specifically for the important class of Al-based films, several questions remain also open:

- The origin of the increasing yield strength with increasing thickness on the AlSi films (inverse size effect) is not clearly identified.
- The physical mechanisms governing the relaxation in AlSi have to be confirmed by observing the evolution of the microstructure as relaxation proceeds.
- The silicon content in the AlSi films could not be located. A more in-depth TEM analysis is required to locate the Si and identify the origin of the very different time dependent response of pure and alloyed Al.
- The origin of the particularly high ductility in pure Al is not understood and TEM investigation coupled to external loading should aim at determining whether grain growth mechanisms are involved.

All these open questions necessitate the use of TEM for observation of the microstructure of the film material. The back etching technique detailed in Chapter 7 provides thus the adequate tool for that purpose. This demonstrates that in addition to providing mechanical data of a film material, the lab on-chip concept can be coupled to TEM to have more insights in the deformation and fracture properties.

Appendix A

Design procedure based on an imposed relative error

The present design procedure consists in determining the range of acceptable dimensions for the actuators and test specimens, such as to respect a constant relative error $x\,|_{\varepsilon}$ on the strain and on the stress $x\,|_{\sigma}$ for given value of Δu, $\Delta\varepsilon_a^{mis}$ and $\Delta\varepsilon^{mis}$. Based on Eq. 4.10, the first condition (on the strain) for a valid design writes (using a small strain assumption)

$$x\,|_{\varepsilon}\,\varepsilon^{mech} > \frac{u}{L_0} - \varepsilon^{mis}. \tag{A.1}$$

Introducing the expression of the strain in the specimen Eq. 4.8 in Eq. A.1 gives the following condition

$$u > \frac{\Delta u}{x\,|_{\varepsilon}} + L_0\left(\frac{\Delta\varepsilon^{mis}}{x\,|_{\varepsilon}} + \varepsilon^{mis}\right). \tag{A.2}$$

Neglecting the presence of the mismatch strain into the test specimen, this equation means that the tolerated error on the displacement $x\,|_{\varepsilon}\,u$ must, at least, be larger than Δu which is tied to the measurement method for u.

Based on Eq. 4.11, the second condition for a valid design writes

$$x\mid_{\sigma}\sigma > E_a R\left(\frac{-u}{L_{a0}} - \varepsilon_a^{mis}\right). \tag{A.3}$$

Introducing the expression of the stress in the specimen Eq. 4.9 in Eq. A.3 gives the following condition

$$u < L_{a0}\left(-\varepsilon_a^{mis} - \frac{\Delta\varepsilon_a^{mis}}{x\mid_{\sigma}}\right) - \frac{\Delta u}{x\mid_{\sigma}}. \tag{A.4}$$

This condition implies that $|\varepsilon_a^{mis}| > \Delta\varepsilon_a^{mis}/x\mid_{\sigma}$ in order to have a solution, u being defined as a positive quantity. Combining Eq. A.2 and Eq. A.4 shows that, there is a minimum value of β

$$\beta > \frac{\frac{1}{x|_{\varepsilon}} + \frac{1}{x|_{\sigma}} + \alpha\left(\frac{\Delta\varepsilon_a^{mis}}{x|_{\varepsilon}} + \varepsilon^{mis}\right)}{\varepsilon_a^{mis} + \frac{\Delta\varepsilon_a^{mis}}{x|_{\sigma}}}. \tag{A.5}$$

A.1 Design for small strain elastic behaviour

Let us assume that the test material has a Young's modulus E, and that strain measurements must be made in the range $[\varepsilon_{min}, \varepsilon_{max}]$. Introducing in the expression of stress (Eq. 4.9) and strain (Eq. 4.8) (small displacement) in Hooke's law (Eq. 4.12) leads to an expression for the displacement u

$$u = \frac{\varepsilon^{mis} - \chi\varepsilon_a^{mis}}{\frac{1}{L_0} + \frac{\chi}{L_{a0}}}. \tag{A.6}$$

This equation is similar to Eq. 4.13 except that the nondimensional stiffness ratio $\chi = R/E^* = S_a E_a/SE$ has been defined. Introducing Eq. A.6 into the first design condition (Eq. A.2) leads to

$$\chi > \beta\frac{\frac{1}{\alpha} + \Delta\varepsilon^{mis}}{-\varepsilon_a^{mis} x\mid_{\varepsilon}\beta + 1 + \alpha\Delta\varepsilon^{mis} + \alpha\varepsilon^{mis} x\mid_{\varepsilon}}, \tag{A.7}$$

while the second condition (Eq. A.4) becomes

$$\chi < -\frac{\beta\left(\varepsilon_a^{mis} x\mid_\sigma + \Delta\varepsilon_a^{mis}\right) + 1 + \alpha\varepsilon^{mis} x\mid_\sigma}{\frac{\alpha}{\beta} + \alpha\Delta\varepsilon_a^{mis}}. \tag{A.8}$$

The design requirements are thus these two conditions on the stiffness ratio together with the constraint of being able to generate mechanical strains in the range $[\varepsilon_{min}, \varepsilon_{max}]$ which remains identical to Eq. 4.15.

A.2 Design for plastic behaviour

The developments for the moderate to large strain plastic behaviour closely follow the procedure described just above, except that the stress σ is now equal to σ_0. The change of cross section S is neglected. By using the same conventions as for the first design procedure, the constraints write

$$\chi > -\beta\frac{\sigma_0}{E_a}\frac{x\mid_\varepsilon}{x\mid_\varepsilon \varepsilon_a^{mis}\beta + \beta + \alpha\left(x\mid_\varepsilon \varepsilon^{mis} - \Delta\varepsilon^{mis}\right)} \tag{A.9}$$

$$\chi \leq \beta\frac{\sigma_0}{E_a}\frac{x\mid_\sigma}{\Delta\varepsilon_a^{mis}\beta + 1} \tag{A.10}$$

while Eq. 4.16 does not change.

Appendix B

List of references

Publications in international journals

1. **M. Coulombier**, G. Guisbiers, M.-S. Colla, J.-P. Raskin, T. Pardoen, *On-chip stress relaxation method for freestanding thin film materials*, Review of Scientific Instruments, to be submitted

2. **M. Coulombier**, A. Boé, C. Brugger, J.-P. Raskin, T. Pardoen, *Imperfection-sensitive ductility of aluminium thin films*, Scripta Materialia, Vol. 62, 10, p. 742-745 (2010)

3. T. Pardoen, **M. Coulombier**, A. Boé, A. Safi, C. Brugger, S. Ryelandt, P. Carbonnelle, S. Gravier, J.-P. Raskin, *Ductility of thin metallic films*, Materials Science Forum, Vol. 633-634, p. 615-635 (2010)

4. C. Brugger, **M. Coulombier**, T. J. Massart, J.-P. Raskin, T. Pardoen, *Strain gradient plasticity analysis of the strength and ductility of thin metallic films using an enriched interface model*, Acta Materialia, Vol. 58, 15, p. 4940-4949 (2010)

5. S. Gravier, **M. Coulombier**, A. Safi, N. André, A. Boé, J.-P. Raskin, T. Pardoen, *New on-chip nanomechanical testing laboratory -*

applications to aluminum and polysilicon thin films, IEEE Journal of Microelectromechanical Systems, Vol. 18, 3, p. 555-569 (2009)

6. A. Boé, A. Safi, **M. Coulombier**, D. Fabrègue, T. Pardoen, J.-P. Raskin, *MEMS-based microstructures for nanomechanical characterization of thin films*, Smart Materials and Structures, Vol. 18, 11 (2009)

7. A. Boé, A. Safi, **M. Coulombier**, T. Pardoen, J.-P. Raskin, *Internal stress relaxation based method for elastic stiffness characterization of very thin films*, Thin Solid Films, Vol. 518, 1, p. 260-264 (2009)

8. D. Fabrègue, N. André, **M. Coulombier**, J.-P. Raskin, T. Pardoen, *Multipurpose nanomechanical testing machines revealing the size-dependent strength and high ductility of pure aluminium submicron films*, Micro & Nano Letters, Vol. 2, 1, p. 13-16 (2007)

9. J.-P. Raskin, F. Iker, N. André, D. Fabrègue, **M. Coulombier**, T. Pardoen, *From nanoelectronics towards nanoelectromechanical Systems*, Revue E Tijdschrift, Vol. 1, p. 26-33 (2007)

10. N. André, **M. Coulombier**, V. De Longueville, D. Fabrègue, T. Gets, T. Pardoen, J.-P. Raskin, *Microfabrication-based nanomechanical laboratory for testing the ductility of submicron aluminium films*, Microelectronic Engineering, Vol. 84, 11, p. 2714-2718 (2007)

International conference contributions

1. **M. Coulombier**, G. Guisbiers, M.-S. Colla, J.-P. Raskin, T. Pardoen, *Experimental evidences of competing stress relaxation mechanisms in thin Al/Si and Pd films tested on chip*, 2011 Materials Research Society Fall Meeting, Boston (2011)

2. T. Pardoen, **M. Coulombier**, M.-S. Colla, H. Idrissi, B. Wang, A. Boé, D. Schrijvers, J.-P. Raskin, *Imperfection, rate and size dependent plastic localization in thin nanocrystalline metallic films*,

20th Technical meeting: mechanical behaviour of nanomaterials, metallic glasses and architecturally designed materials, Paris (2011)

3. **M. Coulombier**, L. Ryelandt, H. Idrissi, B. Wang, A. Boé, D. Schrijvers, J.-P. Raskin, T. Pardoen, *Deformation mechanisms in aluminium and aluminium-silicon freestanding thin films uncovered through on-chip testing*, Euromat2011, Montpellier (2011)

4. S. Ryelandt, P. Carbonnelle, **M. Coulombier**, M.-S. Colla, S. Houri, G. Zeb, A. Zulfiqar, U. Bhaskar, J-P. Raskin, T. Pardoen, *High throughput lab-on-chip for testing the mechanical properties of thin films*, Euromat2011, Montpellier (2011)

5. T. Pardoen, **M. Coulombier**, H. Idrissi, B. Wang, C. Brugger, A. Enmili, *Ultra large local ductility in thin freestanding Al films*, 2010 Materials Research Society Fall Meeting, Boston (2010)

6. T. Pardoen, **M. Coulombier**, A. Boé, C. Brugger, M.-S. Colla, L. Delannay, S. Dancette, J.-P. Raskin, *Imperfection and size dependent fracture of thin metallic films*, 5th International Conference on Multiscale Materials Modeling, Freiburg (2010)

7. B. Wang, H. Idrissi, M.-S. Colla, **M. Coulombier**, J.-P. Raskin, T. Pardoen, D. Schrijvers, *TEM characterization of freestanding metallic thin films deformed by controlled on chip internal stress*, 17th International Microscopy Congress, Rio de Janeiro (2010)

8. C. Brugger, **M. Coulombier**, A. Boé, M.-S. Colla, J.-P. Raskin, T. Pardoen, *Size dependent ductility and fracture behaviour of thin freestanding metallic films*, 18th European Conference on Fracture, Dresden (2010)

9. D. Schrijvers, H. Idrissi, B. Wang, M.-S. Colla, **M. Coulombier**, A. Boé, J. Proost, J.-P. Raskin, T. Pardoen, *TEM characterization of freestanding Pd and Al films for lab-on-chip nanomechanical tensile testing*, Microscience 2010, London (2010)

10. P. Carbonnelle, S. Ryelandt, A. Boé, **M. Coulombier**, A. Zulfiqar, U.K. Bhaskar, J.-P. Raskin, T. Pardoen, *Lab-on-chips based testing methods to investigate the mechanical behaviour of thin*

films, 2nd International Conference on Functional Nanocoatings, Dresden (2010)

11. P. Carbonnelle, S. Ryelandt, A. Boé, **M. Coulombier**, A. Zulfiqar, U.K. Bhaskar, J.-P. Raskin, T. Pardoen, *Lab-on-chips based testing methods to investigate the mechanical behavior of nanofilms*, European Conference on Nano Film, Liège (2010)

12. S. Ryelandt, P. Carbonnelle, A. Boé, **M. Coulombier**, U.K. Bhaskar, A. Zulfiqar, M.-S. Colla, J. Proost, S. Godet, J.-P. Raskin, T. Pardoen, *Nanomechanical testing of thin metallic films application to aluminium, palladium and chromium films*, European Conference on Nano Film, Liège (2010)

13. M.-S. Colla, **M. Coulombier**, A. Boé, H. Idrissi, B. Wang, J. Proost, J.-P. Raskin, T. Pardoen, *Characterization of the mechanical properties of freestanding palladium films by on chip internal stress controlled nanomechanical tensile testing*, Nanobrucken nanomechanical testing workshop, Saarbrucken (2010)

14. T. Pardoen, C. Brugger, **M. Coulombier**, A. Boé, J.-P. Raskin, T.J. Massart, *Strain hardening in fine grained metallic alloys : from bulk to thin film systems*, The International Symposium on Plasticity 2010, St Kitts (2010)

15. T. Pardoen, C. Brugger, **M. Coulombier**, A. Boé, M.-S. Colla, J. Proost, J.-P. Raskin, *Imperfection and size dependent ductility of thin freestanding metallic films*, 2009 Materials Research Society Fall Meeting, Boston (2009)

16. **M. Coulombier**, A. Boé, S. Ryelandt, C. Brugger, B. Wang, H. Idrissi, D. Schrijvers, J.-P. Raskin, T. Pardoen, *Size dependent ductility of thin metallic films using internal stress driven nanotesting structures*, Innovations in Thin Film Processing and Characterization, Nancy (2009)

17. M.-S. Colla, R. Delmelle, A. Boé, **M. Coulombier**, J.-P. Raskin, J. Proost, T. Pardoen, *Impact of hydriding cycles on mechanical*

properties of palladium thin film, Innovations in Thin Film Processing and Characterization, Nancy (2009)

18. A. Boé, **M. Coulombier**, M.-S. Colla, U.K. Bhaskar, A. Zulfiqar, J.-P. Raskin, T. Pardoen, *Internal stress relaxation based method to extract the Young's modulus of brittle and ductile thin layers*, Innovations in Thin Film Processing and Characterization, Nancy (2009)

19. C. Brugger, **M. Coulombier**, A. Boé, J.-P. Raskin, T.J. Massart, T. Pardoen, *Strain gradient plasticity based modeling of the necking in thin metallic films: influence of grain size and imperfections*, Materials Science & Technology Conference & Exhibition 2009, Pittsburgh (2009)

20. **M. Coulombier**, A. Boé, U.K. Bhaskar, S. Ryelandt, C. Brugger, J.-P. Raskin, T. Pardoen, *New testing method for ductility of thin Al films*, ECI 2009 Nanomechanical Testing in Materials Research and Development, Barga (2009)

21. A. Boé, **M. Coulombier**, M.-S. Colla, C. Brugger, J. Dille, J. Proost, T. Pardoen, J.-P. Raskin, *Lab-on-chip tensile stages for nanomechanical testing and TEM analysis*, 35th International Conference on Micro & Nano Engineering, Ghent (2009)

22. C. Brugger, **M. Coulombier**, A. Boé, J.-P. Raskin, T.J. Massart, T. Pardoen, *Strain gradient plasticity based modeling of the ductility of thin freestanding metallic films*, 15th International Conference on the Strength of Materials, Dresden (2009)

23. **M. Coulombier**, A. Boé, A. Safi, S. Gravier, J.-P. Raskin, T. Pardoen, *Fracture of thin freestanding ductile metallic films characterized using a nanomechanical lab-on-chip technique*, 12th International Congress on Fracture, Ottawa (2009)

24. A. Boé, **M. Coulombier**, A. Safi, J.-P. Raskin, T. Pardoen, *On-chip testing laboratory for nanomechanical characterization of thin films*, 2009 SEM Annual Conference and Exposition on Experimental and Applied Mechanics, Albuquerque (2009)

25. **M. Coulombier**, A. Boé, S. Ryelandt, J.-P. Raskin, T. Pardoen, *TEM observation of damage in aluminium thin films using on-chip nanomechanical testing laboratory*, GDR Mecano - 2ème atelier général Ecole des Mines de Paris, Paris (2009)

26. A. Boé, **M. Coulombier**, S. Ryelandt, J.-P. Raskin, T. Pardoen, *MEMS based microstructures for nanomechanical characterization of thin films*, GDR Mecano - 2ème atelier général Ecole des Mines de Paris, Paris (2009)

27. **M. Coulombier**, A. Safi, A. Boé, P. Carbonnelle, J.-P. Raskin, T. Pardoen, *A new on chip micro and nanolaboratory measuring the mechanical properties of ductile and brittle thin film materials*, 9th Symposium on Nano-mechanical Testing - Nanomech, Hückelhoven (2008)

28. A. Boé, A. Safi, **M. Coulombier**, T. Pardoen, J.-P. Raskin, *MEMS microstructures for the nanomechanical characterization of thin films*, International Conference on Multifunctional Materials and Structures, Hong-Kong (2008)

29. T. Pardoen, **M. Coulombier**, A. Safi, A. Boé, J.-P. Raskin, *A new nanomechanical testing concept for thin films*, Gordon Conference on thin films, Colby College, Maine (2008)

30. A. Safi, S. Houri, **M. Coulombier**, S. Gravier, N. André, T. Pardoen, J.-P. Raskin, *A new on chip nanomechanical testing concept applied to ductile and brittle thin film materials*, Surface Modification of Materials Scientific Research Community of the F.W.O. - Mechanical Behavior of Materials in Small Volumes, Heverlee (2008)

31. T. Pardoen, A. Safi, S. Houri, **M. Coulombier**, S. Gravier, N. André, P. Carbonnelle, J.-P. Raskin, *A new on chip nanomechanical testing method*, Observatory for Micro & NanoTechnologies - Nanomechanics for NEMS: scientific and technological issues, Grenoble (2008)

32. T. Pardoen, A. Safi, **M. Coulombier**, S. Gravier, P. Carbonnelle, J.-P. Raskin, *A new on chip nanomechanical testing concept applied to ductile and brittle thin film materials*, 2nd Integration & Commercialization of Micro & Nanosystems - International Conference &andan Exhibition, Clear Water Bay, Kowloon (2008)

33. A. Safi, S. Houri, **M. Coulombier**, S. Gravier, N. André, T. Pardoen, J.-P. Raskin, *A new on chip nanomechanical testing concept applied to ductile and brittle thin film materials*, EuroSimE 2008 International Conference on Thermal, Mechanical and Multi-Physics; Simulation and Experiments in Microelectronics and Micro-Systems, Freiburg im Breisgau (2008)

34. T. Pardoen, J.-P. Raskin, **M. Coulombier**, S. Gravier, N. André, A. Safi, V. De Longueville, S. Sobieski, S. Houri, *Multipurpose on-chip nanomechanical laboratory for testing thin films*, 2007 Materials Research Society Fall Meeting, Boston (2007)

35. N. André, **M. Coulombier**, V. De Longueville, D. Fabrègue, T. Gets, S. Gravier, S. Houri, A. Safi, J.-P. Raskin, T. Pardoen, *Multipurpose on-chip nanomechanical laboratory for testing the size-dependent strength and ductility of submicron metallic films*, International Union of Theoretical and Applied Mechanics Symposium on Multi-Scale Plasticity of Crystalline Materials Organization, Eindhoven (2007)

36. **M. Coulombier**, S. Gravier, T. Pardoen, D. Fabrègue, N. André, S. Houri, J.-P. Raskin, *Multipurpose on-chip nanomechanical laboratory revealing the size-dependent strenght and high ductility of pure aluminium submicron films*, European Congress and Exhibition on Advanced Materials and Processes, Nuremberg (2007)

37. **M. Coulombier**, S. Gravier, T. Pardoen, D. Fabrègue, N. André, S. Houri, J.-P. Raskin, *New concept of multipurpose on-chip nanomechanical laboratory*, 1st International Congress and Exhibition on Microreliability and Nanoreliability in Key Technology Applications, Berlin (2007)

38. **M. Coulombier**, N. André, S. Sobieski, S. Houri, S. Gravier, P. Carbonnelle, J.-P. Raskin, T. Pardoen, *Microlaboratoire "on chip" pour la mesure des propriétés mécaniques de films minces*, Pôle de compétitivité MECATECH - Journée de Rencontre Entreprises-Laboratoires, Louvain-la-Neuve (2007)

39. J.-P. Raskin, D. Fabrègue, N. André, **M. Coulombier**, T. Pardoen, *Low complexity testing micromachines revealing size-dependent mechanical properties of thin Al films*, 14th International Conference on Solid-State Sensors, Actuators and Microsystems, Lyon (2007)

40. T. Pardoen, D. Fabrègue, N. André, **M. Coulombier**, J.-P. Raskin, *Nanomechanical testing machines revealing size-dependent mechanical properties of thin metallic films*, Materials and Structures for Advanced Micro and Nano-electronics, Bruges (2007)

41. **M. Coulombier**, N. André, V. De Longueville, D. Fabrègue, T. Gets, S. Gravier, S. Houri, J.-P. Raskin, T. Pardoen, *New multipurpose nanomechanical laboratory based on MEMS Technology*, Workshop on "Nanomaterials : microstructural and mechanical characterisations, simulations", Poitiers (2006)

42. T. Pardoen, D. Fabrègue, **M. Coulombier**, N. André, J.-P. Raskin, *Micromechanical testing lab-on-chip for nano-sized materials*, 2006 Materials Research Society Fall Meeting, Boston (2006)

43. D. Fabrègue, N. André, T. Pardoen, J.-P. Raskin, **M. Coulombier**, *New internal stress driven micromachines for measuring the mechanical properties of thin films*, International Symposium on Design, Test, Integration and Packaging of MEMS/MOEMS, Stresa (2006)

Patent

T. Pardoen, D. Fabrègue, J.-P. Raskin, N. André, **M. Coulombier**, *Internal stress actuated micro- and nanomachines for testing physical*

properties of micro- and nano-sized material samples, Publication number: EP19873366 (A2)

Bibliography

[1] Agilent Technologies. *Agilent Continuous Stiffness Measurement (CSM) Option*, 2011.

[2] André, N. *CMOS co-integrated in-plane and out-of-plane MEMS sensors*. PhD thesis, UCL, 2011.

[3] André, N., Coulombier, M., De Longueville, V., Fabrègue, D., Gets, T., Gravier, S., Pardoen, T., and Raskin, J.-P. Microfabrication-based nanomechanical laboratory for testing the ductility of submicron aluminium films. *Microelectronic Engineering 84*, 11 (Nov. 2007), 2714–2718.

[4] Bader, S., Kalaugher, E. M., and Arzt, E. Comparison of mechanical properties and microstructure of al(1 wt.%si) and al(1 wt.%si, 0.5 wt.%cu) thin films. *Thin Solid Films 263*, 2 (July 1995), 175–184.

[5] Beams, J. *Structure and Properties of Thin Films*. John Wiley and Sons, 1959, ch. Mechanical properties of thin films of gold and silver, p. 183.

[6] Bei, H., Shim, S., George, E., Miller, M., Herbert, E., and Pharr, G. Compressive strengths of molybdenum alloy micro-pillars prepared using a new technique. *Scripta Materialia 57*, 5 (2007), 397 – 400.

[7] Boé, A., Safi, A., Coulombier, M., Pardoen, T., and Raskin, J.-P. Internal stress relaxation based method for elastic

stiffness characterization of very thin films. *Thin Solid Films 518*, 1 (Nov. 2009), 260–264.

[8] Bochniak, W. The cottrell-stokes law for f.c.c. single crystals. *Acta Metallurgica et Materialia 41*, 11 (1993), 3133 – 3140.

[9] Bochniak, W. Mode of deformation and the cottrell-strokes law in f.c.c. single crystals. *Acta Metallurgica et Materialia 43*, 1 (1995), 225 – 233.

[10] Brugger, C., Coulombier, M., Massart, T., Raskin, J.-P., and Pardoen, T. Strain gradient plasticity analysis of the strength and ductility of thin metallic films using an enriched interface model. *Acta Materialia 58*, 15 (Sept. 2010), 4940–4949.

[11] Chasiotis, I., and Knauss, W. A new microtensile tester for the study of mems materials with the aid of atomic force microscopy. *Experimental Mechanics 42* (2002), 51–57.

[12] Chen, X., and Vlassak, J. J. Numerical study on the measurement of thin film mechanical properties by means of nanoindentation. *Journal of Materials Research 16*, 10 (2001), 2974–2982.

[13] Cheng, S., Ma, E., Wang, Y., Kecskes, L., Youssef, K., Koch, C., Trociewitz, U., and Han, K. Tensile properties of in situ consolidated nanocrystalline cu. *Acta Materialia 53*, 5 (Mar. 2005), 1521–1533.

[14] Cheng, Y.-W., Read, D. T., McColskey, J. D., and Wright, J. E. A tensile-testing technique for micrometer-sized free-standing thin films. *Thin Solid Films 484*, 1-2 (July 2005), 426–432.

[15] Colla, M.-S., Wang, B., Idrissi, H., Schryvers, D., Raskin, J.-P., and Pardoen, T. High strength-ductility of thin nanocrystalline palladium films with nanoscale twins: On-chip testing and grain aggregate model. *Acta Materialia 60*, 4 (2012), 1795 – 1806.

[16] Coulombier, M., Boé, A., Brugger, C., Raskin, J., and Pardoen, T. Imperfection-sensitive ductility of aluminium thin films. *Scripta Materialia 62*, 10 (May 2010), 742–745.

[17] Coulombier, M., Boé, A., Safi, A., Gravier, S., Pardoen, T., and Raskin, J.-P. Fracture of thin freestanding ductile metallic films characterized using a nanomechanical lab-on-chip technique.

[18] Coulombier, M., Guisbiers, G., Colla, M.-S., Raskin, J.-P., and Pardoen, T. On-chip stress relaxation method for freestanding thin film materials. *Review of Scientific Instruments* (to be submitted).

[19] Dalla Torre, F., Van Swygenhoven, H., and Victoria, M. Nanocrystalline electrodeposited ni: microstructure and tensile properties. *Acta Materialia 50*, 15 (Sept. 2002), 3957–3970.

[20] de Boer, M. P., Corwin, A. D., Kotula, P. G., Baker, M. S., Michael, J. R., Subhash, G., and Shaw, M. J. On-chip laboratory suite for testing of free-standing metal film mechanical properties, part ii - experiments. *Acta Materialia 56*, 14 (Aug. 2008), 3313–3326.

[21] de Boer, M. P., DelRio, F. W., and Baker, M. S. On-chip test structure suite for free-standing metal film mechanical property testing, part i - analysis. *Acta Materialia 56*, 14 (Aug. 2008), 3344–3352.

[22] Dehm, G. Miniaturized single-crystalline fcc metals deformed in tension: New insights in size-dependent plasticity. *Progress in Materials Science 54*, 6 (Aug. 2009), 664–688.

[23] Dehm, G., Balk, T. J., Edongué, H., and Arzt, E. Small-scale plasticity in thin cu and al films. *Microelectronic Engineering 70*, 2-4 (Nov. 2003), 412–424.

[24] Delannay, F., and Pardoen, T. *Introduction to the deformation and fracture of matherials*. Université catholique de Louvain, 2004.

[25] Doerner, M., and Nix, W. A method for interpreting the data from depth-sensing indentation instruments. *Journal of Materials Research 1*, 04 (1986), 601–609.

[26] Doerner, M. F., and Nix, W. D. Stresses and deformation processes in thin films on substrates. *Critical Reviews in Solid State and Materials Sciences 14*, 3 (1988), 225–268.

[27] dos Santos, J. M. M., Wang K., Horsfall, A., Prata Pina, J., Wright, N., O'Neill, A., Soare, S., Bull, S., Terry, J., Walton, A., Gundlach, A., and J.T.M., S. Calibration of mems-based test structures for predicting thermomechanical stress in integrated circuit interconnect structures. *IEEE Transactions on device and materials reliability 5*, 4 (Dec. 2005), 713–719.

[28] Duhamel, C., Brechet, Y., and Champion, Y. Activation volume and deviation from cottrellstokes law at small grain size. *International Journal of Plasticity 26*, 5 (2010), 747 – 757.

[29] Eiper, E., Keckes, J., Martinschitz, K., Zizak, I., Cabié, M., and Dehm, G. Size-independent stresses in al thin films thermally strained down to -100 °c. *Acta Materialia 55*, 6 (Apr. 2007), 1941–1946.

[30] Emery, R. D., and Povirk, G. L. Tensile behavior of free-standing gold films. part ii. fine-grained films. *Acta Materialia 51*, 7 (Apr. 2003), 2079–2087.

[31] Espinosa, H., Panico, M., Berbenni, S., and Schwarz, K. Discrete dislocation dynamics simulations to interpret plasticity size and surface effects in freestanding fcc thin films. *International Journal of Plasticity 22*, 11 (Nov. 2006), 2091–2117.

[32] Espinosa, H., Prorok, B., Peng, B., Kim, K., Moldovan, N., Auciello, O., Carlisle, J., Gruen, D., and Mancini, D. Mechanical properties of ultrananocrystalline diamond thin films relevant to mems/nems devices. *Experimental Mechanics 43* (2003), 256–268.

[33] Espinosa, H., Zhu, Y., and Moldovan, N. Design and operation of a mems-based material testing system for nanomechanical characterization. *Journal of Microelectromechanical Systems 16*, 5 (Oct. 2007), 1219 –1231.

[34] Espinosa, H. D., Berbenni, S., Panico, M., and Schwarz, K. W. An interpretation of size-scale plasticity in geometrically confined systems. *Proceedings of the National Academy of Sciences of the United States of America 102*, 47 (2005), 16933–16938.

[35] Espinosa, H. D., Prorok, B. C., and Fischer, M. A methodology for determining mechanical properties of freestanding thin films and mems materials. *Journal of the Mechanics and Physics of Solids 51*, 1 (Jan. 2003), 47–67.

[36] Espinosa, H. D., Prorok, B. C., and Peng, B. Plasticity size effects in free-standing submicron polycrystalline fcc films subjected to pure tension. *Journal of the Mechanics and Physics of Solids 52*, 3 (Mar. 2004), 667–689.

[37] Fabregue, D., Andre, N., Coulombier, M., Raskin, J., and Pardoen, T. Multipurpose nanomechanical testing machines revealing the size-dependent strength and high ductility of pure aluminium submicron films. *Micro Nano Letters, IET 2*, 1 (Mar. 2007), 13 –16.

[38] Farkas, D., Frøseth, A., and Swygenhoven, H. V. Grain boundary migration during room temperature deformation of nanocrystalline ni. *Scripta Materialia 55*, 8 (2006), 695 – 698.

[39] Finot, M., and Suresh, S. Small and large deformation of thick and thin-film multi-layers: Effects of layer geometry, plasticity and compositional gradients. *Journal of the Mechanics and Physics of Solids 44*, 5 (1996), 683 – 721. Mechanics and Physics of Layered and Graded Materials.

[40] Fleck, N. A., and Hutchinson, J. W. A reformulation of strain gradient plasticity. *Journal of the Mechanics and Physics of Solids 49*, 10 (Oct. 2001), 2245–2271.

[41] Flinn, P., Gardner, D., and Nix, W. Measurement and interpretation of stress in aluminum-based metallization as a function of thermal history. *Electron Devices, IEEE Transactions on 34*, 3 (Mar. 1987), 689 – 699.

[42] Florando, J., and Nix, W. A microbeam bending method for studying stress-strain relations for metal thin films on silicon substrates. *Journal of the Mechanics and Physics of Solids 53*, 3 (Mar. 2005), 619–638.

[43] Freund, L., and Suresh, S. *Thin Film Materials*. 2003.

[44] Geers, M., Brekelmans, W., and Janssen, P. Size effects in miniaturized polycrystalline fcc samples: Strengthening versus weakening. *International Journal of Solids and Structures 43*, 24 (Nov. 2006), 7304–7321.

[45] Gennissen, P., and French, P. Sacrificial oxide etching compatible with aluminum metallization. In *Solid State Sensors and Actuators, 1997. TRANSDUCERS '97 Chicago* (1997), vol. 1, pp. 225 –228.

[46] Gets, T. Dimensionnement de micro et nanomachines « on chip » et étude des propriétés de plasticité, d'endommagement et de rupture de films et poutres sub-microniques. Master's thesis, UCL, 2007.

[47] Gianola, D., Mendis, B., Cheng, X., and Hemker, K. Grain-size stabilization by impurities and effect on stress-coupled grain growth in nanocrystalline al thin films. *Materials Science and Engineering: A 483-484* (June 2008), 637–640.

[48] Gianola, D., Van Petegem, S., Legros, M., Brandstetter, S., Van Swygenhoven, H., and Hemker, K. Stress-assisted discontinuous grain growth and its effect on the deformation behavior of nanocrystalline aluminum thin films. *Acta Materialia 54*, 8 (May 2006), 2253–2263.

[49] Gianola, D., Warner, D., Molinari, J., and Hemker, K. Increased strain rate sensitivity due to stress-coupled grain growth in nanocrystalline al. *Scripta Materialia 55*, 7 (Oct. 2006), 649–652.

[50] Gravier, S., Coulombier, M., Safi, A., Andre, N., Boe, A., Raskin, J.-P., and Pardoen, T. New on-chip nanomechanical testing laboratory - applications to aluminum and polysilicon thin films. *Journal of Microelectromechanical Systems 18*, 3 (June 2009), 555 –569.

[51] Greer, J. R., and Hosson, J. T. D. Plasticity in small-sized metallic systems: Intrinsic versus extrinsic size effect. *Progress in Materials Science 56*, 6 (2011), 654 – 724.

[52] Gruber, P. A., Böhm, J., Onuseit, F., Wanner, A., Spolenak, R., and Arzt, E. Size effects on yield strength and strain hardening for ultra-thin cu films with and without passivation: A study by synchrotron and bulge test techniques. *Acta Materialia 56*, 10 (June 2008), 2318–2335.

[53] Guckel, H., Burns, D., Rutigliano, C., Lovell, E., and Choi, B. Diagnostic microstructures for the measurement of intrinsic strain in thin films. *Journal of Micromechanics and Microengineering 2*, 2 (1992), 86.

[54] Guckel, H., Randazzo, T., and Burns, D. W. A simple technique for the determination of mechanical strain in thin films with applications to polysilicon. *Journal of Applied Physics 57*, 5 (Mar. 1985), 1671 –1675.

[55] Haque, M., and Saif, M. Microscale materials testing using mems actuators. *Journal of Microelectromechanical Systems 10*, 1 (Mar. 2001), 146 –152.

[56] Haque, M., and Saif, M. A review of mems-based microscale and nanoscale tensile and bending testing. *Experimental Mechanics 43*, 3 (Sept. 2003), 248 –255.

[57] Haque, M., and Saif, M. Thermo-mechanical properties of nano-scale freestanding aluminum films. *Thin Solid Films 484*, 1-2 (July 2005), 364–368.

[58] Haque, M. A., and A Saif, M. T. Mechanical behavior of 30-50 nm thick aluminum films under uniaxial tension. *Scripta Materialia 47*, 12 (Dec. 2002), 863–867.

[59] Haque, M. A., and Saif, M. T. A. Application of mems force sensors for in situ mechanical characterization of nano-scale thin films in sem and tem. *Sensors and Actuators A: Physical 97-98* (Apr. 2002), 239–245.

[60] Haque, M. A., and Saif, M. T. A. Strain gradient effect in nanoscale thin films. *Acta Materialia 51*, 11 (June 2003), 3053–3061.

[61] Hay, J., and Crawford, B. Measuring substrate-independent modulus of thin films. *Journal of Materials Research 26*, 06 (2011), 727–738.

[62] He, J., Luo, J., Le, H., and Moore, D. Mechanical characterization of biocompatible thin film materials by scanning along micro-machined cantilevers for micro-/nano-system. *Materials Science and Engineering: A 423*, 1-2 (May 2006), 134–142.

[63] He, Q., Luo, Z., and Chen, X. Comparison of residual stress measurement in thin films using surface micromachining method. *Thin Solid Films 516*, 16 (June 2008), 5318–5323.

[64] Hommel, M., and Kraft, O. Deformation behavior of thin copper films on deformable substrates. *Acta Materialia 49*, 19 (Nov. 2001), 3935–3947.

[65] Hopcroft, M., Nix, W., and Kenny, T. What is the young's modulus of silicon? *Journal of Microelectromechanical Systems 19*, 2 (Apr. 2010), 229 –238.

[66] Horsfall, A., Wang, K., dos Santos, J., Soare, S., Bull, S., Wright, N., O'Neill, A., Terry, J., Walton, A., Gundlach, A., and Stevenson, J. Dependence of process parameters on stress generation in aluminum thin films. *Device and Materials Reliability, 4*, 3 (Sept. 2004), 482 – 487.

[67] Huang, C., Lou, W., Tsai, C., Wu, T.-C., and Lin, H.-Y. Mechanical properties of polymer thin film measured by the bulge test. *Thin Solid Films 515*, 18 (2007), 7222 – 7226.

[68] Huang, H., Yu, D. Y., Verdier, M., and Spaepen, F. Flow and fracture of free-standing ag and cu thin films and ag/cu multilayers. *International Journal of Fracture 119* (2003), 359–364.

[69] Hutchinson, J., and Neale, K. Influence of strain-rate sensitivity on necking under uniaxial tension. *Acta Metallurgica 25*, 8 (1977), 839 – 846.

[70] Idrissi, H., Wang, B., Colla, M. S., Raskin, J. P., Schryvers, D., and Pardoen, T. Ultrahigh strain hardening in thin palladium films with nanoscale twins. *Advanced Materials 23*, 18 (2011), 2119–2122.

[71] Ishikawa, K., Okuda, H., and Kobayashi, Y. Creep of pure aluminium materials at a low temperature. *Journal of Materials Science Letters 17*, 5 (Mar. 1998), 423–424.

[72] Jin, M., Minor, A., and Jr., J. M. Strain-induced coarsening in nano-grained films. *Thin Solid Films 515*, 6 (2007), 3202 – 3207.

[73] Jin, M., Minor, A., Stach, E., Morris, J., and Jr. Direct observation of deformation-induced grain growth during the nanoindentation of ultrafine-grained al at room temperature. *Acta Materialia 52*, 18 (2004), 5381 – 5387.

[74] Jonnalagadda, K., Karanjgaokar, N., Chasiotis, I., Chee, J., and Peroulis, D. Strain rate sensitivity of nanocrystalline au films at room temperature. *Acta Materialia 58*, 14 (Aug. 2010), 4674–4684.

[75] Kang, Y., and Ho, P. Thickness dependent mechanical behavior of submicron aluminum films. *Journal of Electronic Materials 26*, 7 (July 1997), 805–813.

[76] Kaouache, B., Gergaud, P., Thomas, O., Bostrom, O., and Legros, M. Impact of thermal cycling on the evolution of grain, precipitate and dislocation structure in al, 0.5 *Microelectronic Engineering 70*, 2-4 (Nov. 2003), 447–454.

[77] Kiener, D., Grosinger, W., Dehm, G., and Pippan, R. A further step towards an understanding of size-dependent crystal plasticity: In situ tension experiments of miniaturized single-crystal copper samples. *Acta Materialia 56*, 3 (Feb. 2008), 580–592.

[78] Kiener, D., Motz, C., Rester, M., Jenko, M., and Dehm, G. Fib damage of cu and possible consequences for miniaturized mechanical tests. *Materials Science and Engineering: A 459*, 1-2 (June 2007), 262–272.

[79] Kocks, U., and Mecking, H. Physics and phenomenology of strain hardening: the fcc case. *Progress in Materials Science 48* (2003), 171–273.

[80] Kraft, O., Hommel, M., and Arzt, E. X-ray diffraction as a tool to study the mechanical behaviour of thin films. *Materials Science and Engineering A 288*, 2 (Sept. 2000), 209–216.

[81] Kumar, K., Suresh, S., Chisholm, M., Horton, J., and Wang, P. Deformation of electrodeposited nanocrystalline nickel. *Acta Materialia 51*, 2 (2003), 387 – 405.

[82] Kumar, K. S., Swygenhoven, H. V., and Suresh, S. Mechanical behavior of nanocrystalline metals and alloys. *Acta Materialia 51*, 19 (2003), 5743 – 5774.

[83] Laconte, J., Iker, F., Jorez, S., André, N., Proost, J., Pardoen, T., Flandre, D., and Raskin, J.-P. Thin films

stress extraction using micromachined structures and wafer curvature measurements. *Microelectronic Engineering 76*, 1-4 (Oct. 2004), 219–226.

[84] LaVan, D., and Sharpe, W. Tensile testing of microsamples. *Experimental Mechanics 39* (1999), 210–216.

[85] Lawn, B., and Wilshaw, T. *Fracture of Brittle Solids*. 1993.

[86] Legros, M., Dehm, G., Keller-Flaig, R. M., Arzt, E., Hemker, K. J., and Suresh, S. Dynamic observation of al thin films plastically strained in a tem. *Materials Science and Engineering A 309-310* (July 2001), 463–467.

[87] Legros, M., Gianola, D. S., and Hemker, K. J. In situ tem observations of fast grain-boundary motion in stressed nanocrystalline aluminum films. *Acta Materialia 56*, 14 (Aug. 2008), 3380–3393.

[88] Legros, M., Hemker, K. J., Gouldstone, A., Suresh, S., Keller-Flaig, R. M., and Arzt, E. Microstructural evolution in passivated al films on si substrates during thermal cycling. *Acta Materialia 50*, 13 (Aug. 2002), 3435–3452.

[89] Li, N. Size effects of nanoindentation creep. *Journal of Material Research 19*, 2 (Feb. 2004), 513–522.

[90] Lu, L., Li, S. X., and Lu, K. An abnormal strain rate effect on tensile behavior in nanocrystalline copper. *Scripta Materialia 45*, 10 (Nov. 2001), 1163–1169.

[91] Lucas, B., and Oliver, W. Indentation power-law creep of high-purity indium. *Metallurgical and Materials Transactions A 30* (1999), 601–610.

[92] Modlinski, R., Witvrouw, A., Ratchev, P., Puers, R., Toonder, J. d., and Wolf, I. D. Creep characterization of al alloy thin films for use in mems applications. *Microelectronic Engineering 76*, 1-4 (Oct. 2004), 272–278.

[93] Morris, J., Jr., Jin, M., and Minor, A. In situ studies of the transmission of strain across grain boundaries. *Materials Science and Engineering: A 462*, 1-2 (2007), 412 – 417.

[94] Nicola, L., Xiang, Y., Vlassak, J., Van der Giessen, E., and Needleman, A. Plastic deformation of freestanding thin films: Experiments and modeling. *Journal of the Mechanics and Physics of Solids 54*, 10 (Oct. 2006), 2089–2110.

[95] Niordson, C. F., and Tvergaard, V. Instabilities in power law gradient hardening materials. *International Journal of Solids and Structures 42*, 9-10 (2005), 2559 – 2573.

[96] Nix, W. Mechanical properties of thin films. *Metallurgical and Materials Transactions A 20* (1989), 2217–2245.

[97] Oh, S., Legros, M., Kiener, D., Gruber, P., and Dehm, G. In situ tem straining of single crystal au films on polyimide: Change of deformation mechanisms at the nanoscale. *Acta Materialia 55*, 16 (Sept. 2007), 5558–5571.

[98] Ohring, M. *Materials science of thin films: deposition and structure*. 2002.

[99] Oliver, W., and Pharr, G. An improved technique for determining hardness and elastic modulus using load and displacement sensing indentation experiments. *Journal of Materials Research 7*, 06 (1992), 1564–1583.

[100] Oliver, W., and Pharr, G. Measurement of hardness and elastic modulus by instrumented indentation: Advances in understanding and refinements to methodology. *Journal of Materials Research 19* (2004), 3–20.

[101] Pardoen, T., Coulombier, M., Boé, A., Safi, A., Brugger, C., Ryelandt, Carbonnelle, P., Gravier, S., and Raskin, J. Ductility of thin metallic films. *Materials Science Forum 633-634* (2010), 615–635.

[102] Peng, B., Pugno, N., and Espinosa, H. An analysis of the membrane deflection experiment used in the investigation of mechanical properties of freestanding submicron thin films. *International Journal of Solids and Structures 43*, 11-12 (June 2006), 3292–3305.

[103] Pineau, A., and Pardoen, T. Failure of metals. In *Comprehensive Structural Integrity*, I. Milne, R. O. Ritchie, and B. Karihaloo, Eds. Pergamon, Oxford, 2007, pp. 684–797.

[104] Proost, J., Witvrouw, A., Cosemans, P., Roussel, P., and Maex, K. Stress relaxation in al(cu) thin films. *Microelectronic Engineering 33* (Sept. 1997), 137–147.

[105] Prorok, B., Zhu, Y., Espinosa, H., Guo, Z., Bazant, Z., Zhao, Y., and Yakobson, B. Micro- and nanomechanics. *Encyclopedia of Nanoscience and Nanotechnology 5* (2004), 555–600.

[106] Read, D. T., Cheng, Y.-W., Keller, R. R., and McColskey, J. D. Tensile properties of free-standing aluminum thin films. *Scripta Materialia 45*, 5 (Sept. 2001), 583–589.

[107] Reddy, A., Kahn, H., and Heuer, A. A mems-based evaluation of the mechanical properties of metallic thin films. *Journal of Microelectromechanical Systems 16*, 3 (June 2007), 650 –658.

[108] Renault, P. O., Villain, P., Coupeau, C., Goudeau, P., and Badawi, K. F. Damage mode tensile testing of thin gold films on polyimide substrates by x-ray diffraction and atomic force microscopy. *Thin Solid Films 424*, 2 (Jan. 2003), 267–273.

[109] Rupert, T. J., Gianola, D. S., Gan, Y., and Hemker, K. J. Experimental observations of stress-driven grain boundary migration. *Science 326*, 5960 (2009), 1686–1690.

[110] Safi, A. Conception, fabrication et application d'un microlaboratoire on chip: Etude des proprietes mecaniques de films minces de titane. Master's thesis, UCL, 2007.

[111] Saif, M. T. A., Zhang, S., Haque, A., and Hsia, K. J. Effect of native al2o3 on the elastic response of nanoscale al films. *Acta Materialia 50*, 11 (June 2002), 2779–2786.

[112] Sanders, P., Eastman, J., and Weertman, J. Elastic and tensile behavior of nanocrystalline copper and palladium. *Acta Materialia 45*, 10 (Oct. 1997), 4019–4025.

[113] Schadler, L. S., and Noyan, I. C. Experimental determination of the strain transfer across a flexible intermediate layer in thin-film structures. *Journal of Materials Science Letters 11* (1992), 1067–1069.

[114] Schwaiger, R., Moser, B., Dao, M., Chollacoop, N., and Suresh, S. Some critical experiments on the strain-rate sensitivity of nanocrystalline nickel. *Acta Materialia 51*, 17 (Oct. 2003), 5159–5172.

[115] Sharpe, W.N., J., Yuan, B., and Edwards, R. A new technique for measuring the mechanical properties of thin films. *Journal of Microelectromechanical Systems 6*, 3 (Sept. 1997), 193 –199.

[116] Shen, Y.-L., and Suresh, S. Thermal cycling and stress relaxation response of si-al and si-al-sio2 layered thin films. *Acta Metallurgica et Materialia 43*, 11 (Nov. 1995), 3915–3926.

[117] Simar, A., Bréchet, Y., de Meester, B., Denquin, A., and Pardoen, T. Sequential modeling of local precipitation, strength and strain hardening in friction stir welds of an aluminum alloy 6005a-t6. *Acta Materialia 55*, 18 (2007), 6133 – 6143.

[118] Stoney, G. G. The tension of metallic films deposited by electrolysis. *Proceedings of the Royal Society of London. Series A, Containing Papers of a Mathematical and Physical Character 82*, 553 (1909), 172–175.

[119] Taylor, J. R. *An introduction to error analysis : the study of uncertainties in physical measurements*. 1997.

[120] Tsuchiya, T., Hirata, M., Chiba, N., Udo, R., Yoshitomi, Y., Ando, T., Sato, K., Takashima, K., Higo, Y., Saotome, Y., Ogawa, H., and Ozaki, K. Cross comparison of thin-film tensile-testing methods examined using single-crystal silicon, polysilicon, nickel, and titanium films. *Journal of Microelectromechanical Systems 14*, 5 (Oct. 2005), 1178 – 1186.

[121] Tsuchiya, T., Shikida, M., and Sato, K. Tensile testing system for sub-micrometer thick films. *Sensors and Actuators A: Physical 97-98* (Apr. 2002), 492–496.

[122] Tsuchiya, T., Tabata, O., Sakata, J., and Taga, Y. Specimen size effect on tensile strength of surface-micromachined polycrystalline silicon thin films. *Journal of Microelectromechanical Systems 7*, 1 (Mar. 1998), 106 –113.

[123] Uchic, M. D., Shade, P. A., and Dimiduk, D. M. Plasticity of micrometer-scale single crystals in compression. *Annual Review of Materials Research 39* (2009), 361–386.

[124] Van Barel, G. *In-situ characterization of mechanical properties of MEMS structural layers using different test approaches, with application to thick poly-SiGe.* PhD thesis, Universiteit Hasselt, May 2011.

[125] Van Swygenhoven, H., Derlet, P. M., and Hasnaoui, A. Atomic mechanism for dislocation emission from nanosized grain boundaries. *Phys. Rev. B 66*, 2 (June 2002), 024101.

[126] Vayrette, R., Rivero, C., Gros, B., Blayac, S., and Inal, K. Residual stress estimation in damascene copper interconnects using embedded sensors. *Microelectronic Engineering 87*, 3 (Mar. 2010), 412–415.

[127] Velez Callejas, G. Fabrication et caracterisation d'une micromachine. Tech. rep., 2011.

[128] Venkatraman, R., and Bravman, J. Mechanical properties and microstructural characterization of al-cu(0.5) thin films. *Journal of electronic materials 19*, 11 (Aug. 1990), 1231–1237.

[129] Venkatraman, R., and Bravman, J. Separation of film thickness and grain boundary strenghtening effects in al thin films on si. *Journal of material research 7*, 8 (Aug. 1992), 2040–2048.

[130] Venstra, W., van der Velden, M., Spronck, J., van Eijk, J., and Sarro, P. Versatile wire configuration for independent actuation of bending and torsion displacements of microcantilevers. In *Sensors, 2005 IEEE* (Nov. 2005), pp. 584–587.

[131] Wang, Y., Hamza, A., and Ma, E. Temperature-dependent strain rate sensitivity and activation volume of nanocrystalline ni. *Acta Materialia 54*, 10 (June 2006), 2715–2726.

[132] Wei, Q. Strain rate effects in the ultrafine grain and nanocrystalline regimes influence on some constitutive responses. *Journal of Materials Science 42* (2007), 1709–1727.

[133] Wei, X., Lee, D., Shim, S., Chen, X., and Kysar, J. W. Plane-strain bulge test for nanocrystalline copper thin films. *Scripta Materialia 57*, 6 (Sept. 2007), 541–544.

[134] Weihs, T., Hong, S., Bravman, J., and Nix, W. Mechanical deflection of cantilever microbeams: A new technique for testing the mechanical properties of thin films. *Journal of material research 3*, 5 (Oct. 1988), 931–942.

[135] Xiang, Y., Chen, X., and Vlassak, J. Plane-strain bulge test for thin films. *Journal of material research 20*, 9 (Apr. 2005), 2360 – 2370.

[136] Xiang, Y., and Vlassak, J. Bauschinger and size effects in thin-film plasticity. *Acta Materialia 54*, 20 (Dec. 2006), 5449–5460.

[137] Youngdahl, C. J., Sanders, P. G., Eastman, J. A., and Weertman, J. R. Compressive yield strengths of nanocrystalline cu and pd. *Scripta Materialia 37*, 6 (Sept. 1997), 809–813.

[138] Zulfiqar, A. Study of stress in pecvd si3n4 and its application in lab-on-chip concept. Tech. rep., 2009.